



The  
University  
Of  
Sheffield.

DISSERTATION SUBMITTED FOR THE DEGREE OF  
DOCTOR OF PHILOSOPHY  
DEPARTMENT OF PHYSICS AND ASTRONOMY

---

Improving the efficiency of  
quantum light sources based on  
solid-state emitters

---

Andrea Barbiero

March 2021



# Declaration of authorship

I hereby declare that except where specific reference is made to the work of others, the contents of this dissertation are original and have not been submitted in whole or in part for consideration for any other degree or qualification in this, or any other university. This dissertation is my own work and contains nothing which is the outcome of work done in collaboration with others, except as specified in the text and Acknowledgements.

Andrea Barbiero



# Acknowledgements

The work presented in this thesis would not have been possible without the help of many people I had the privilege to meet during this exciting journey. First of all, I owe a huge debt of gratitude to Jan Huwer and Mark Stevenson for sharing their broad expertise and genuine passion for scientific research and for providing support and guidance whenever needed. I would also like to thank Andrew Shields for giving me the chance to join his research group at Toshiba and Aleksander Tartakovskii for the academic supervision. I'm deeply thankful to Dave Ellis and Joanna Skiba-Szymanska for teaching me the fundamentals of semiconductor processing and making my work in the cleanroom a lot easier. Moreover, I thank Tina Müller for many interesting exchanges of ideas.

I gratefully acknowledge the 4-Photon ITN for the financial support and the opportunity to meet fellow early-stage researchers around Europe. It has been an honor to be a member of this amazing organization. A very heartfelt thank you also goes to all my fellow PhD students at Toshiba who have made this period of my life so enjoyable, with a special mention to Enzo, Jonathan, Mariella and Mirko.

Naturally, those few years would have been a lot more difficult without the encouragement coming from my family and friends back in Italy. I am particularly grateful to my parents Mauro and Roberta for supporting my previous studies and my decisions and to my brother Davide, to whom I wish a bright future and career. Finally, I would like to thank Chrissy for accepting to dance with me three years ago and for the happiness she brought in my life ever since.



# Abstract

This dissertation presents the design, development and characterization of various platforms for efficient generation of quantum light. Most of the devices investigated are based on InAs quantum dots, which are considered mature candidates for many applications in the field of quantum information because of their compatibility with conventional semiconductor opto-electronics.

The first set of experiments concerns the incorporation of highly symmetric InAs Droplet Epitaxy QDs emitting in the telecom O-band within an optical microcavity, focusing on improving the extraction efficiency whilst keeping a low fine-structure splitting for entanglement-based experiments. Since the signal intensities achieved with this approach would be sufficient only for proof-of-principle experiments, the second main avenue of work involves hybrid circular Bragg gratings (CBGs) which have recently emerged as a promising solution for broadband optical enhancement of the radiation emitted by quantum dots. In particular, we combine the broadband properties of hybrid CBGs operating in the telecom O-band with a membrane-transfer process that can be performed on wafer scale. Furthermore, we characterize the performances of multiple devices to address the question of reproducibility. We also present a design optimization of CBGs operating in the telecom C-band, which is crucial for quantum network applications, and propose a modified structure directly compatible with electric field control. Finally, we examine a different class of quantum emitters which appear in atomically thin layers of WSe<sub>2</sub> and investigate GaP nano-antennas as an optical device to enhance their light output.



# Publications

Parts of this dissertation have appeared in the following publications and conference contributions.

## Articles

- **A. Barbiero**, A. Tuktamyshev, G. Pirard, J. Huwer, T. Müller, R. M. Stevenson, S. Bietti, S. Vichi, A. Fedorov, G. Bester, S. Sanguinetti and A. J. Shields, *Exciton fine structure in InAs quantum dots with cavity-enhanced emission at telecommunication wavelength and grown on a GaAs(111)A vicinal substrate*. Physical Review Applied, 18(3), 034081 (2022).
- **A. Barbiero**, J. Huwer, J. Skiba-Szymanska, D. Ellis, R. M. Stevenson, T. Müller, G. Shooter, L. Goff, D. A. Ritchie and A. J. Shields, *High performance single-photon sources at telecom wavelength based on broadband hybrid circular Bragg gratings*. ACS Photonics 9(9), 3060-3066 (2022).
- **A. Barbiero**, J. Huwer, J. Skiba-Szymanska, T. Müller, R. M. Stevenson and A. J. Shields, *Design study for an efficient semiconductor quantum light source operating in the telecom C-band based on an electrically-driven circular Bragg grating*. Optics Express 30(7), 10919-10928 (2022).

## Conference contributions

- ‘Single-photon sources based on semiconductor quantum dots’ (poster), **School on Introduction to Quantum Information**, Basel, Switzerland (Jan 2018).

- ‘Hybrid circular Bragg gratings for efficient photon extraction’ (talk), **3<sup>rd</sup> 4-Photon Workshop** (moved online), Milan, Italy (Jan 2020).
- ‘Efficient quantum light sources at telecom wavelength for long-distance secure communication’ (talk), **Quantum Matter**, Barcelona, Spain (Jun 2022).
- ‘Efficient quantum light sources at telecom wavelength based on hybrid circular Bragg gratings’ (talk), **SPIE Optics+Photonics**, San Diego, USA (Aug 2022).

# Contents

<b>Declaration of authorship</b>	<b>iii</b>
<b>Acknowledgements</b>	<b>v</b>
<b>Abstract</b>	<b>vii</b>
<b>Publications</b>	<b>ix</b>
<b>1 Introduction and motivation</b>	<b>1</b>
<b>2 Theoretical background</b>	<b>3</b>
2.1 Classical cryptography . . . . .	3
2.2 Quantum cryptography . . . . .	4
2.2.1 Quantum key distribution (QKD) . . . . .	4
2.2.2 Quantum light sources for QKD . . . . .	6
2.3 Semiconductor quantum dots . . . . .	9
2.3.1 Electronic structure of InAs quantum dots . . . . .	10
2.3.2 Optical properties of InAs quantum dots . . . . .	11
2.4 Optical microcavities . . . . .	13
2.4.1 Working principles of optical microcavities . . . . .	13
2.4.2 Quantum dot-cavity coupling and Purcell effect . . . . .	15
2.4.3 Photon collection efficiency and directivity . . . . .	18
<b>3 Experimental methods</b>	<b>21</b>
3.1 QDs growth with Molecular Beam Epitaxy . . . . .	21

3.1.1	Stranski-Krastanov QDs . . . . .	22
3.1.2	Droplet Epitaxy QDs . . . . .	24
3.2	Numerical FEM simulations . . . . .	26
3.3	Device fabrication . . . . .	27
3.3.1	Flip-chip process: wafer bonding and substrate removal . . . . .	29
3.3.2	Electron beam lithography . . . . .	31
3.3.3	Dry etching and resist stripping . . . . .	33
3.3.4	Quality control . . . . .	34
3.4	Optical characterization . . . . .	35
3.4.1	Micro-PL spectroscopy . . . . .	35
3.4.2	Time-resolved spectroscopy . . . . .	38
3.4.3	Hanbury Brown and Twiss interferometry . . . . .	39
<b>4</b>	<b>Cavity-enhanced InAs QDs emitting at telecom wavelength grown on GaAs(111)A</b>	<b>43</b>
4.1	Introduction . . . . .	43
4.2	Sample growth . . . . .	45
4.3	Experimental results . . . . .	46
4.3.1	Reflectivity measurements . . . . .	46
4.3.2	Micro-PL measurements . . . . .	47
4.4	Numerical simulations . . . . .	51
4.4.1	Numerical model . . . . .	51
4.4.2	Influence of the miscut on the optical properties of the QDs . . . . .	52
4.5	Conclusions . . . . .	55
<b>5</b>	<b>Bright Purcell-enhanced single-photon sources in the telecom O-band</b>	<b>57</b>
5.1	Introduction . . . . .	57
5.2	Device design . . . . .	59
5.2.1	Numerical simulations . . . . .	59
5.2.2	Final mask . . . . .	62

---

5.3	Experimental results . . . . .	63
5.3.1	Reflectivity measurements . . . . .	63
5.3.2	Micro-PL measurements . . . . .	66
5.3.3	Emission dynamics . . . . .	69
5.3.4	Photon statistics . . . . .	71
5.3.5	Reproducibility . . . . .	74
5.4	Conclusions . . . . .	78
<b>6</b>	<b>Design of high-performance single-photon sources in the telecom</b>	
	<b>C-band</b>	<b>81</b>
6.1	Introduction . . . . .	81
6.2	Device modeling . . . . .	83
6.3	Numerical simulations . . . . .	84
6.3.1	Optimization of Purcell factor and collection efficiency . . . . .	84
6.3.2	Direct coupling into SM fibre . . . . .	91
6.3.3	Proposal for an electrically driven circular Bragg grating . . . . .	96
6.4	Conclusions . . . . .	99
<b>7</b>	<b>Summary and future work</b>	<b>101</b>
<b>A</b>	<b>Single photon emitters in WSe<sub>2</sub> coupled to GaP nano-antennas</b>	<b>105</b>
A.1	Introduction . . . . .	105
A.2	Methods . . . . .	107
A.2.1	Device design . . . . .	107
A.2.2	Exfoliation and transfer of WSe <sub>2</sub> monolayers . . . . .	109
A.2.3	PL measurements . . . . .	111
A.2.4	First order correlation function measurements . . . . .	111
A.3	Experimental results . . . . .	112
A.3.1	Micro-PL measurements . . . . .	112
A.3.2	Polarization-resolved spectroscopy . . . . .	116
A.3.3	Emission dynamics . . . . .	117

A.3.4	Coherence of a strain-induced single-photon emitter . . . . .	119
A.4	Conclusions . . . . .	121
<b>Bibliography</b>		<b>123</b>

# 1 | Introduction and motivation

The generation and control of light have become increasingly important in many aspects of our life. Nowadays, optical fiber networks allow us to transmit data all over the world, while LED bulbs are the most efficient way to illuminate our homes and the laser technology market keeps expanding with applications in telecommunications, medical treatments and material processing. All those examples involve classical light sources, emitting radiation that can be modeled as an electromagnetic wave with intensity proportional to the amplitude.

On the other hand, quantum light sources cannot be described using classical electromagnetism. Instead, they generate a stream of single photons which can be exploited in experiments involving interesting concepts such as entanglement and quantum teleportation. Some of those effects are on the verge of becoming much more than a scientific curiosity, with applications in quantum computing and quantum cryptography. In fact, keeping sensitive information safe and secure is one of the main challenges created by the rapid progress that the field of information technology has seen over the last decade. Every day an unprecedented amount of personal data is being harvested and stored on remote computer servers and the raising concerns about cybercrime and data breaches make the need for secure transmission of sensitive information more significant than ever.

The work described in this dissertation concerns the development of novel quantum light sources based on solid-state emitters, with the aim of improving their efficiency compared to devices described in previous reports. In fact, an increased light output is fundamental to make single photon sources useful not only for proof-of-principle experiments, but also for future practical applications in the field of quantum communication and computing.

The outline of the thesis is the following: in Chapter 2 we provide a brief introduction to quantum cryptography and discuss the relevant concepts regarding semiconductor quantum dots and optical microcavities. Chapter 3 describes the tools used for numerical simulations, the processing techniques for the fabrication of devices and the experimental methods employed during their optical characterization. In Chapter 4 we present the development of InAs/InAlAs droplet epitaxy quantum dots emitting in the telecom O-band within a DBR microcavity grown on a vicinal GaAs(111)A substrate. We also investigate the influence of the miscut on the natural  $C_{3v}$  symmetry of the surface and on the properties of the emitted light. In Chapter 5 we discuss the integration of InAs/GaAs quantum dots into hybrid circular Bragg gratings operating in the telecom O-band, which are a promising route to provide broadband enhancement of the emitted radiation. In Chapter 6 we extend that approach to InAs/InP QDs emitting in the telecom C-band, presenting a design study for circular Bragg gratings fabricated on InP slabs and proposing an alternative device design compatible with electric field control.

Finally, Chapter 7 presents a summary of the results and outlines possible future improvements while Appendix A summarizes the additional work carried out during my visit to Prof. Alexander Tartakovskii's group at the University of Sheffield. Those last experiments focused on the investigation of a different class of quantum emitters, which appear at cryogenic temperatures in atomically thin layers of WSe<sub>2</sub>.

# 2 | Theoretical background

This chapter provides a basic introduction to the use of single photons for secure communication protocols and summarizes the relevant concepts regarding the use of quantum dots and optical microcavities for the efficient generation of quantum light.

## 2.1 Classical cryptography

Cryptography is a practice that allow only the sender and intended recipient of a message to read its content. In fact, data exchanged between two parties, Alice and Bob, across a public communication channel can be easily intercepted by an eavesdropper Eve. As a result, Alice and Bob usually employ a series of techniques to keep their communication secure: Alice could use an algorithm (cipher) to scramble her message and combine it with some additional piece of information (key). This operation is commonly known as encryption. When Bob receives the encrypted message, he can retrieve and read the original text by applying the inverse operation (decryption).

The different encryption protocols that Alice and Bob may choose to implement can be placed in two main classes: asymmetric (public-key) schemes and symmetric (private-key) schemes [1]. In asymmetric schemes, Bob must first compute both a public and a private key. Then he shares the public key with Alice, who will use it to encrypt her message. Finally, when Bob receives the encrypted message he can securely retrieve the original text using the private key, which he is the only one to know. Public-key schemes are very popular and their security is based on computational complexity, i.e. the difficulty for an eavesdropper to infer the private key even after intercepting the public key.

On the other hand, symmetric schemes exploit a single private key for both the encryption and decryption operations. Although perfectly secure in principle, these schemes require Alice and Bob to possess a randomly generated common secret key, which must be at least as long as the message itself and used only for the encryption and decryption of a single message (one-time pad). Since the secure distribution of long keys is difficult, this solution is currently used only for the most critical applications.

## 2.2 Quantum cryptography

In the last few years the field of quantum computing has shown remarkable advances, posing a threat to the security of traditional public-key protocols. Nevertheless, research in quantum cryptography has demonstrated that quantum mechanical properties can be also exploited to develop novel communications techniques capable of resisting such attacks [2].

Between the different solutions proposed, one of the most efficient consists of distributing a secret quantum key between two parties, which can then use classical encryption protocols to share a message securely. As a result, quantum key distribution (QKD) is one of the fastest growing areas in quantum information science. In fact, novel theoretical protocols are designed on a regular basis and proof-of-principle demonstrations are gradually turning into field-trial experiments and commercial prototypes [3].

### 2.2.1 Quantum key distribution (QKD)

The intuition behind QKD is that, if the key distribution is conducted using quantum systems, any attack performed by an eavesdropper will perturb the quantum state prepared by the legitimate users [4]. Therefore, if Eve performs a measurement on the system in the attempt to steal information, Alice and Bob will be able to detect her presence from the increased noise in the communication channel. Moreover, such a noise can be exploited to quantify the amount of information Eve has access to: if

it overcomes a certain limit, Alice and Bob will know that the attacker has gained enough information to compromise the security of the key.

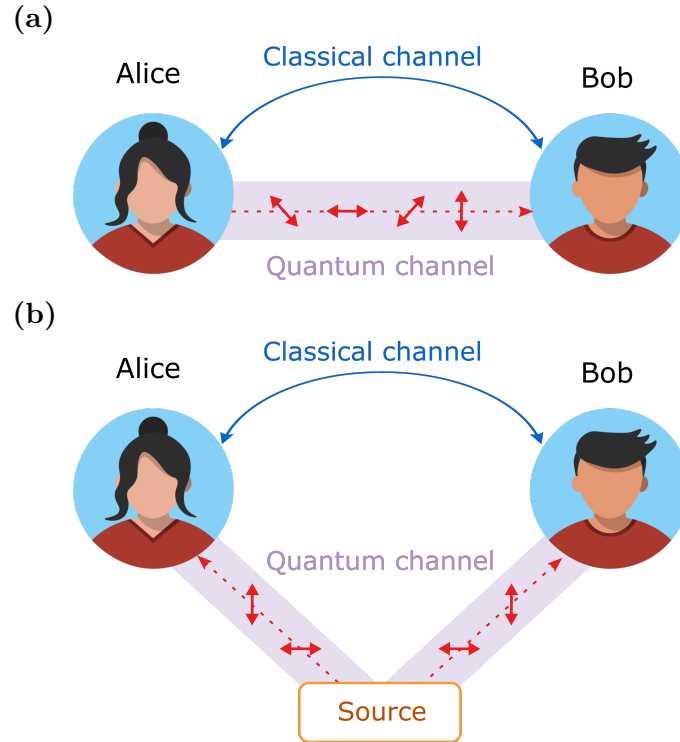


Figure 2.1: Schematic representation of (a) prepare-and-measure QKD and (b) entanglement-based QKD. In both cases the key distribution happens over a quantum channels, while the message is shared securely over a classical channel.

The first QKD protocol, commonly known as BB84, was proposed in 1984 by Charles Bennett and Gilles Brassard and it is based on encoding information into single photons. In fact, photons constitute a convenient communication medium since they can be transmitted over long distances using optical fibres and their phase and polarization can be easily controlled. In order to implement the BB84 protocol, Alice and Bob have agreed to share single photons in one of two complementary bases, such as the linear ( $|H\rangle=0, |V\rangle=1$ ) and the diagonal ( $|D\rangle=0, |A\rangle=1$ ) polarisation bases. The exchange of information happens in two distinct phases [5]: during the first phase, Alice prepares a random sequence of bits  $r_i$  and a second sequence  $b_i^A$ , where the  $i$ -th element of  $b_i^A$  reveals the basis used by Alice to encode the  $i$ -th element of  $r_i$ . After encoding the sequence  $r_i$  in the polarisation of single photons,

she sends it to Bob over a quantum channel. On the receiver side, Bob measures each incoming photon in a random basis, represented by the sequence  $b_i^B$ . In the second phase, which happens over an authenticated classical channel, Bob transmits the sequence  $b_i^B$  and Alice communicates which of his measurement were made using the correct basis. It important to underline that this step does not reveal anything about the content of  $r_i$ . Alice and Bob can now delete from  $r_i$  all the bits measured using incompatible bases to produce their resulting raw key  $r_i'$ . Finally, Alice and Bob compare a subset of their raw keys and, if the error rate does not overcome a certain threshold, they use the remaining secret bits as a final secret key. On the other hand, if the error rate is higher than the threshold, they realize that Eve may have hacked the quantum channel.

The BB84 scheme is an example of prepare-and-measure QKD setting (Figure 2.1a), since Alice prepares the photon states and sends them to Bob who will perform the measurements. The BB84 protocol and its variations are still widely used in experimental implementations of QKD. It is worth mentioning that there exist a second main category of QKD protocols, commonly known as entanglement-based (Figure 2.1b): in these schemes, a source of entangle photon pairs placed in a central node distributes polarization entangled photon pairs to Alice and Bob, who can detect the presence of an eavesdropper by taking advantage of Bell's theorem. The first entanglement-based QKD protocol was proposed in 1991 by Artur Ekert [6] and is therefore identified as E91.

### 2.2.2 Quantum light sources for QKD

As explained in the previous section, photons are an ideal information carrier for QKD protocols, which means that both prepare-and-measure and entanglement-based schemes require efficient sources of pure and indistinguishable single photons or entangled photon pairs. Since those sources are not readily available, typical implementations of QKD usually exploit an approximation of single photon states which is given by heavily attenuated laser pulses containing less than one photon per pulse [7, 8], also known as weak coherent pulses (WCP).

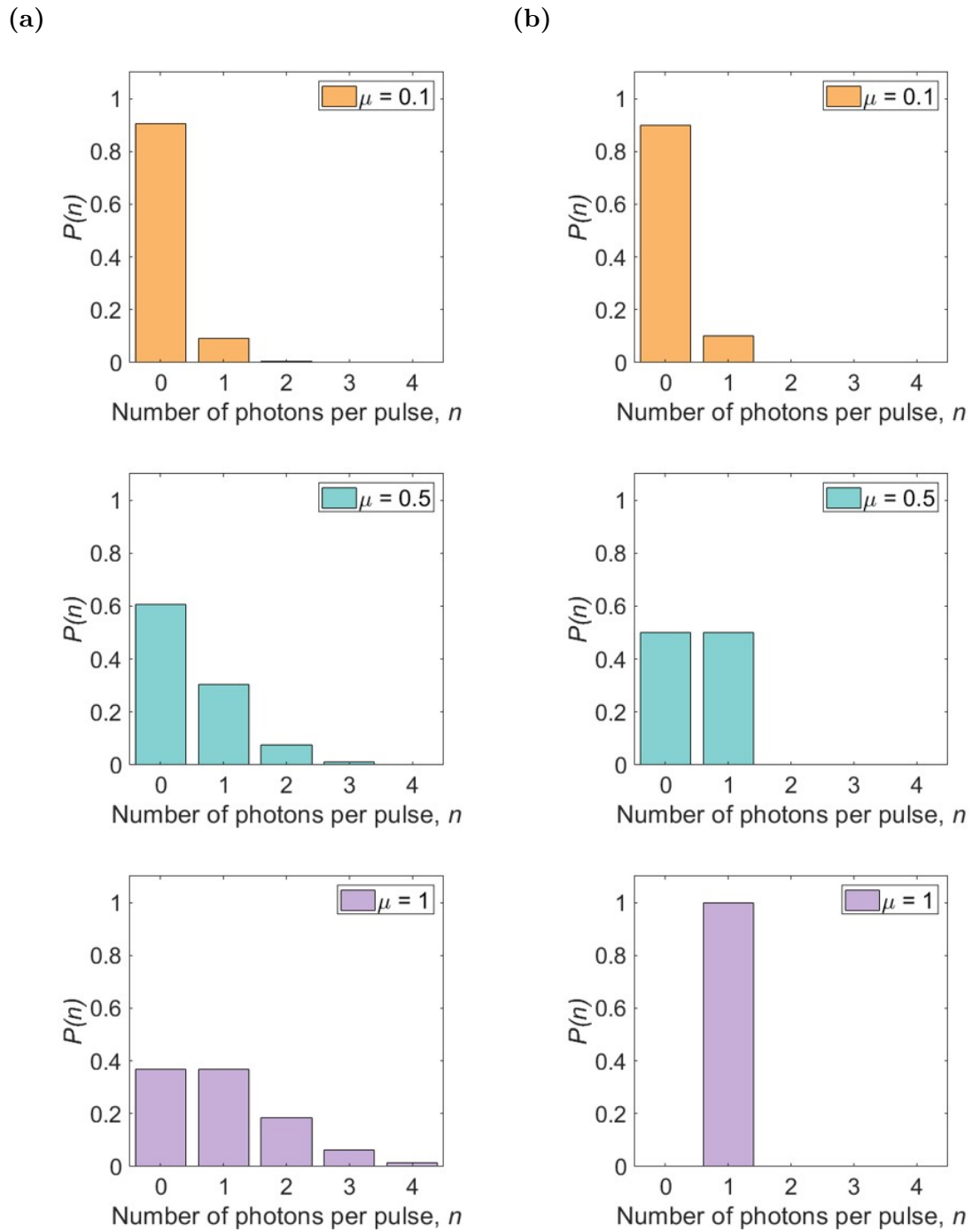


Figure 2.2: (a) Photon statistics of a Poissonian WCP source for three different values of the average photon number  $\mu$ . (b) Corresponding photon statistics of an ideal single photon source with the same average photon number  $\mu$ .

The number of photons in each of those pulses is described by the Poissonian statistics, meaning that the probability  $P(n)$  of having  $n$  photons in a pulse with an average photon number  $\mu$  is given by:

$$P(n) = \frac{\mu^n}{n!} e^{-\mu} \quad (2.1)$$

From Equation 2.1, it can be demonstrated that the conditional probability to find more than one photon in a non-empty pulse is  $\approx \mu/2$  [9]. Therefore, WCPs require a low photon number  $\mu$  in order to minimize the probability of multi-photon events which could potentially impact the security of the protocol. A typical value used in QKD experiments with WCP is  $\mu = 0.1$ . However, such a small value of  $\mu$  has a negative impact on the secret key rate because it reduces the number of photons transmitted through the quantum channel.

Even if this issue can be mitigated by employing the so-called decoy states [10], the Poisson statistics predicts that the probability to find only one photon in WCPs with  $\mu=1$  does not exceed 37%. As a result, a single photon source with an average photon number above that value outperforms any WCP source when driven at the same rate (Figure 2.2) [9]. Moreover, optimal single photon sources could enable novel schemes with the ability to increase the transmission range, such as quantum relays [11] and quantum repeaters [12].

In recent years, several solutions for the development of pure single photon sources such as atoms [13], molecules [14] and nitrogen vacancy centres in diamond [15] have been examined. In this dissertation we will mainly concentrate on semiconductor quantum dots, with an emphasis on telecom wavelengths. In fact, together with compatibility with conventional semiconductor processing and opto-electronics[16], semiconductor quantum dots display all the characteristics needed for on-demand generation of high-quality single, indistinguishable and entangled photons at high rates [9] and are therefore considered one of the most promising candidates for applications in the field of quantum information and quantum cryptography.

## 2.3 Semiconductor quantum dots

In general, quantum dots (QDs) are three-dimensional nanostructures that confine charged particles within a small volume comparable to their de Broglie wavelength [17]. As a result, they contain just a few discrete energy levels in the conduction and valence bands, each of which can be populated by two electrons or holes of opposite spin. Because of this reason, QDs are often referred to as ‘artificial atoms’ [18].

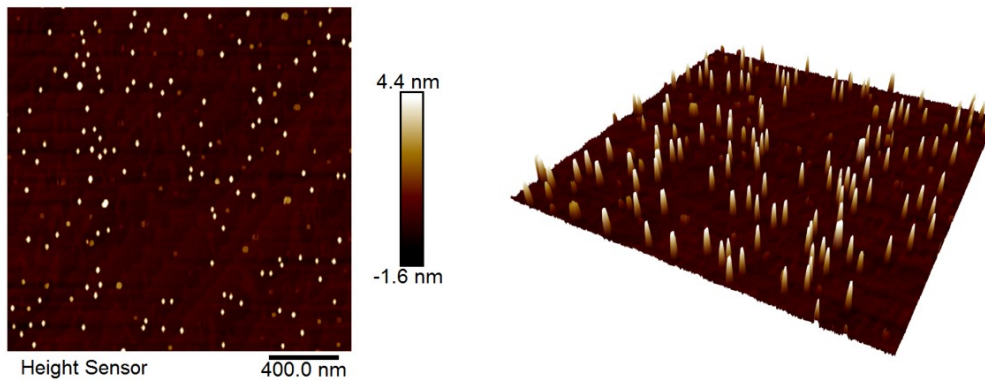


Figure 2.3: Images of InAs quantum dots grown on a GaAs (100) substrate. The images were recorded with an atomic-force microscope (AFM) and kindly provided by Joanna Skiba-Szymanska.

Even if they have been manufactured using various processes, in this dissertation we will focus on epitaxially grown semiconductor QDs [19, 20] which are usually obtained by embedding a low-bandgap material such as InAs ( $\sim 0.4$  eV) into a high-bandgap matrix such as GaAs ( $\sim 1.5$  eV) or InP ( $\sim 1.4$  eV) [21]. Figure 2.3 shows an example of top view and three-dimensional height profile of epitaxially grown InAs/GaAs QDs, which appear as slightly elliptical islands with the major and minor axes oriented along the crystallographic axes of the substrate. More details about the two different processes that have been used to grow the quantum dots employed in this work are provided in Section 3.1.

### 2.3.1 Electronic structure of InAs quantum dots

Both InAs/GaAs and InAs/InP quantum dots may display a rather complex band structure which depends strongly on their geometry and composition [22, 23]. However, the process of photon emission can be understood using the simplified model in Figure 2.4, where a stepwise variation of the electronic band gap creates a quantum well with discrete energy levels.

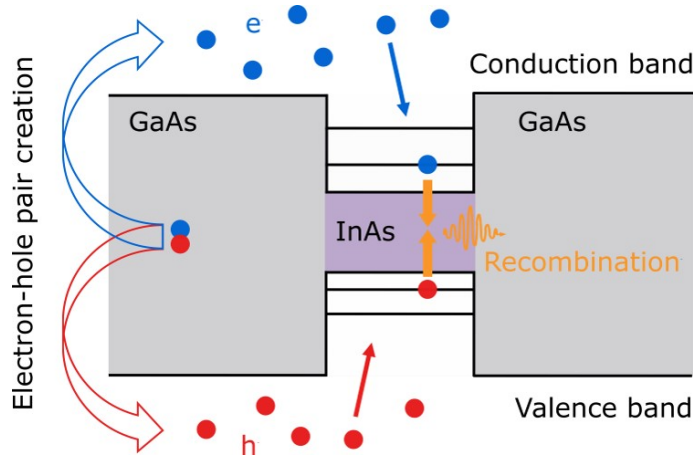


Figure 2.4: Simplified band structure of an InAs/GaAs QD and schematic of the single photon emission process under above-band optical excitation. Shining an above-band laser on the sample excites electrons (blue) in the bulk material, creating electron-hole pairs. The electron-hole pairs can be captured by the QD and occupy a radiative state, from which they recombine with the emission of a single photon (orange).

When a pumping laser with photon energy higher than the bulk material band gap is focused on the sample, electrons and holes are excited over the band edge of the barrier material and then captured by the QD. Here, they lower their energy via phonon interaction and eventually reach a radiative state and recombine with the emission of a single photon [24].

As mentioned above, each of the energy levels can accommodate up to two electrons or holes of opposite spin due to the Pauli exclusion principle. Therefore, QDs can display a plurality of charge configurations depending on the occupancy [25]. The schematic in Figure 2.5 shows the charge configurations that are typically found in semiconductor QDs. The neutral exciton (X) and biexciton (XX) comprise one

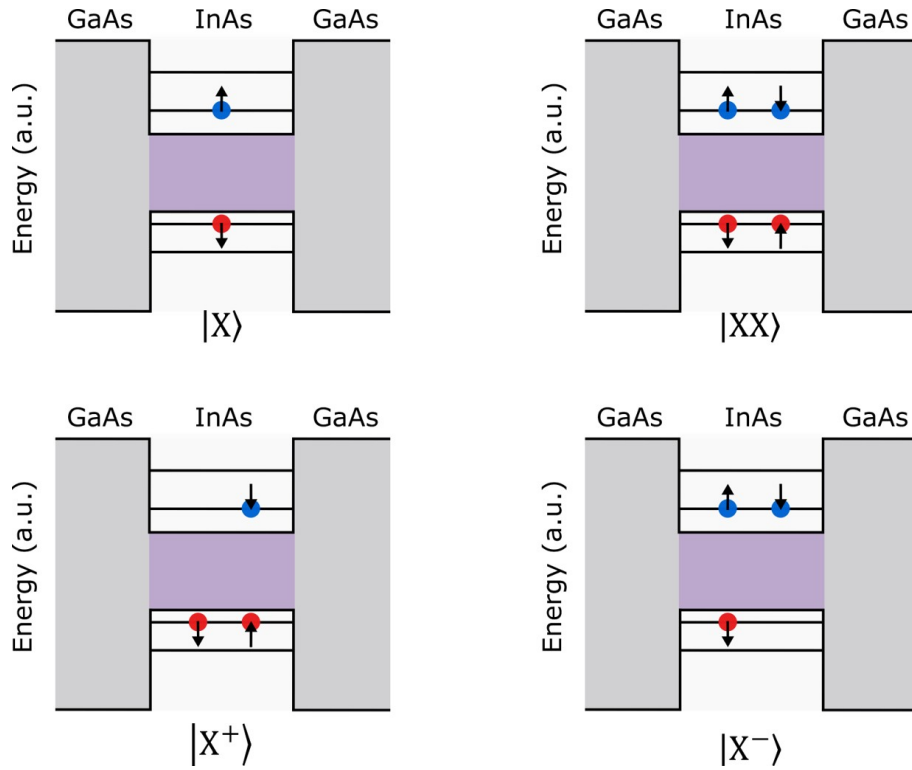


Figure 2.5: Schematic of the most common configurations of trapped electrons and holes into an InAs/GaAs QD: neutral exciton ( $X$ ), neutral biexciton ( $XX$ ), positively charged exciton ( $X^+$ ) and negatively charged exciton ( $X^-$ ).

and two electron-hole pairs, respectively. On the other hand, negatively ( $X^-$ ) and positively ( $X^+$ ) charged excitons (also known as trions) are formed with the addition of a further electron or hole. It is also possible to observe alternative configurations characterized by the presence of additional carriers, however those are not particularly relevant for the work contained in this dissertation.

### 2.3.2 Optical properties of InAs quantum dots

When excited with an above-band laser, the emission spectrum of a QD usually displays a plurality of sharp lines generated by various charge configurations. In the exemplary spectrum of Figure 2.6a, the neutral excitons have been identified using polarization-resolved spectroscopy: in fact, it can be shown that both the  $X$  and  $XX$  transitions are actually linearly polarized doublets with components parallel to the

crystallographic axes of the substrate [25]. This polarization splitting is known as fine structure splitting (FSS) and its magnitude and sign vary among different QDs [26].

The FSS originates from anisotropies in the QD shape or composition, which affect the electron-hole exchange interaction and split the degenerate excitonic eigenstates into a symmetric and an antisymmetric combination, as schematically shown in Figure 2.6b. On the other hand, a vanishing energy splitting is expected for both negatively and positively charged trions [27]. More details on the methods used to identify neutral excitons and trions and to quantify the FSS are provided in Section 3.4.1.

It is also worth noting that in Figure 2.6a, and in general in semiconductor QDs, the X and XX transitions appear at different energies  $E_{XX} \neq E_X$  because of the binding energy related to the Coulomb interaction between carriers [25].

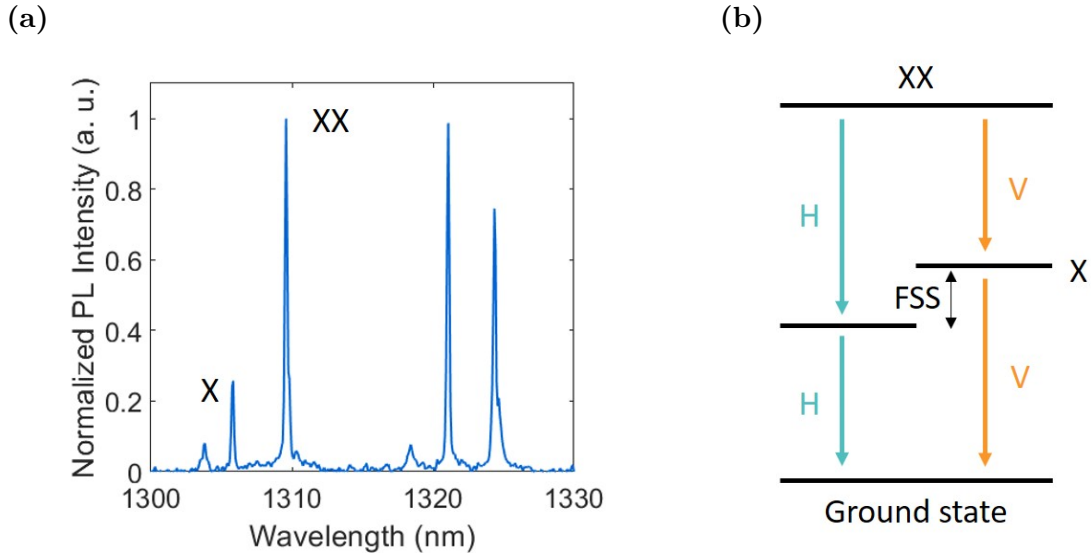


Figure 2.6: (a) Exemplary emission spectrum of an InAs/GaAs QD under above-band laser excitation, with a plurality of transitions corresponding to various charge configurations. (b) Schematic diagram of the biexciton-exciton cascade in semiconductor QDs [25]. FSS represents the fine structure splitting between the exciton eigenstates while H (horizontal) and V (vertical) indicate the two perpendicular linearly polarized decay paths.

## 2.4 Optical microcavities

One of the main advantages offered by solid-state quantum emitters is the possibility to integrate them with various photonic structures, such as waveguides [28, 29, 30] or micro and nanocavities [31, 32, 33, 34] using standard semiconductor processing techniques. This way, one can properly engineer the environment surrounding the emitters and modify the light-matter interaction to increase the efficiency of quantum light sources.

In this section we examine the basic characteristics of optical microcavities and briefly discuss how, in the weak coupling regime, the spontaneous emission rate can be enhanced by the Purcell effect. This effect will be exploited by some of the devices presented in this work. Finally, we introduce the concepts of photon collection efficiency and directivity, which have been widely exploited in geometric approaches such as photonic nanowires [35, 36] or microlenses [37, 38, 39] and will be particularly important for the discussion of circular Bragg gratings (Chapter 5 and 6) and GaP nano-antennas (Appendix A).

### 2.4.1 Working principles of optical microcavities

Optical microcavities, also known as microresonators, are photonic devices that confine photons within small volumes by resonant recirculation [40]. An idealized version of those devices consists of an optical medium surrounded by perfectly reflective faces, where the confinement within the cavity is guaranteed by strong reflection at its boundaries. As a result, the confined light fields propagate back and forth in the medium and are subject to interference: fields of definite frequencies  $f_0$ , which are related to the geometrical parameters of the structure, may interfere constructively and be reinforced. On the other hand, fields with frequencies  $f \neq f_0$  will ultimately interfere destructively and have their intensity strongly suppressed.

The ideal structure described above would permanently confine light fields without any losses and have a discrete set of  $\delta$ -like resonant modes at precise values, one for each eigenfrequency. In a real situation instead, the boundaries are not perfectly

reflective and the consequent energy dissipation and time-limited photon confinement lead to a broadening of the resonance peaks [41]. This deviation from ideal conditions is commonly described using two physical parameters: the quality factor  $Q$  and the mode volume  $V$ .

In the time domain, the quality factor measures the effectiveness of the energy storage within the resonator and can be defined as the angular frequency  $\omega_0 = 2\pi f_0$  times the ratio of the time-averaged energy  $U$  stored in the cavity to the dissipation rate per cycle  $P$  [42]:

$$Q = \omega_0 \frac{U}{P} = \omega_0 U \left| \frac{dU}{dt} \right|^{-1} \quad (2.2)$$

Assuming that the energy stored in the resonator decays exponentially with a time constant  $\tau_c$  as  $U(t) = U_0 \exp(-\tau_c t)$ , one can write [43]:

$$Q = \omega_0 \tau_c \quad (2.3)$$

showing that the quality factor is ultimately a measure of the cavity-mode lifetime.

For a better understanding of the experimental results, it is also worth discussing the equivalent definition in the frequency-domain. In fact, the energy formulation of the uncertainty principle:

$$\Delta E \cdot \Delta t \geq \hbar \quad (2.4)$$

suggests that the time-limited photon confinement causes a broadening of the otherwise  $\delta$ -like resonant modes. Substituting  $\Delta E = \hbar \cdot \Delta\omega$  and  $\Delta t = \tau_c$  gives a lower bound for the broadening  $\Delta\omega$ :

$$\Delta\omega \geq \frac{1}{\tau_c} \quad (2.5)$$

It can be shown that, for real excitation frequencies, the resonance broadening is well described by a Lorentzian function [44] with full width at half-maximum  $\Delta\omega$  which is actually equal to the reciprocal of  $\tau_c$  [41]. Hence:

$$Q = \frac{\omega_0}{\Delta\omega} \quad (2.6)$$

The definition given in Equation 2.6 is particularly important for photoluminescence experiments because it gives the chance to estimate  $Q$  with a straightforward transmission or reflectivity measurement.

While the quality factor quantifies the temporal evolution of the photon confinement within the cavity, the mode volume quantifies its spatial confinement. Depending on the type of resonator there may be multiple ways to calculate the associated mode volume rigorously. However, in general  $V$  can be defined as the volume integral of the energy stored in the mode normalized by its maximum value [45]:

$$V = \frac{\int_{Vol} \epsilon_r |E(r)|^2 \cdot d^3r}{\max[\epsilon_r \cdot |E(r)|^2]} \quad (2.7)$$

where  $\epsilon_r$  is the dielectric constant,  $|E(r)|$  is the electric field strength and  $Vol$  is a quantization volume which includes the resonator.

### 2.4.2 Quantum dot-cavity coupling and Purcell effect

In the previous subsections we summarized the fundamental properties of optical resonators. Now we discuss the enhanced light-matter interaction that arises when coupling a quantum emitter to a microcavity. The investigation of those interactions in coupled systems is commonly known as cavity quantum electrodynamics (cavity QED).

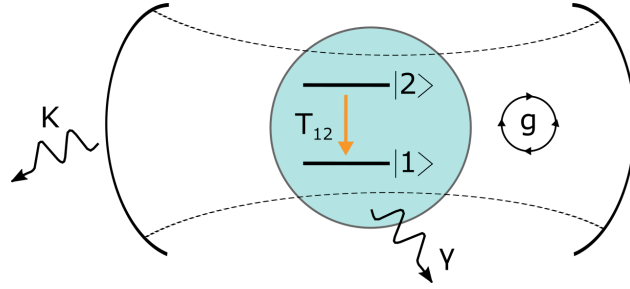


Figure 2.7: Schematic diagram of a two-level system coupled an optical resonator, where  $W_{12} = 1/T_{12}$  represents the radiative decay rate from  $|2\rangle$  to  $|1\rangle$ ,  $g$  is the coupling strength parameter,  $Y$  is the non-resonant decay rate and  $K$  is the photon loss rate.

In a simplified picture, we can model the quantum emitter as the two-level system (TLS) in Figure 2.7, with a ground state  $|1\rangle$  and an excited state  $|2\rangle$ . The decay rate  $W_{12}$  from  $|2\rangle$  to  $|1\rangle$  can be calculated using the Fermi's Golden Rule [46]:

$$W_{12} = \frac{2\pi}{\hbar^2} |M_{12}|^2 \rho(\omega) = \frac{2\pi}{\hbar^2} |\langle 2 | H_{\text{int}} | 1 \rangle|^2 \rho(\omega) \quad (2.8)$$

where  $\hbar$  is the reduced Plank constant,  $M_{12}$  is the matrix element associated to the transition,  $H_{\text{int}}$  is the interaction Hamiltonian and  $\rho(\omega)$  denotes the density of states, i.e. the number of available modes that can accept an emitted photon at a certain frequency  $\omega$ .

It can be demonstrated that the photonic environment can influence the decay rate  $W_{12}$ , as briefly shown in the following subsections. For a rigorous discussion, we refer the reader to Ref. [44].

### Spontaneous emission in free-space

First, we consider the TLS to be in free-space. To simplify the calculation, it is helpful to imagine that the TLS is incorporated in a very large cavity of volume  $V_0$  with negligible effect on its properties. In the approximation of a dipole transition between the two eigenstates with radiative lifetime  $T_{12}$ , the matrix element  $M_{12}$  as the product between the transition dipole  $\mathbf{p}$  and the vacuum electric field  $\mathbf{E}_{\text{vac}}$  [44]:

$$M_{12} = \langle \mathbf{p} \cdot \mathbf{E}_{\text{vac}} \rangle \quad (2.9)$$

By introducing the normalized dipole orientation factor  $\xi$ :

$$\xi = \frac{|\mathbf{p} \cdot \mathbf{E}|}{|\mathbf{p}||\mathbf{E}|} \quad (2.10)$$

it can be demonstrated that [44]:

$$M_{12}^2 = \xi^2 \mu_{12}^2 E_{\text{vac}}^2 \quad (2.11)$$

where  $\mu_{12}$  is the electric dipole matrix element of the transition. By averaging over all the possible orientations of the atomic dipole, one obtains:

$$M_{12}^2 = \frac{1}{3} \mu_{12}^2 E_{\text{vac}}^2 = \frac{\mu_{12}^2 \hbar \omega}{6 \epsilon_0 V_0} \quad (2.12)$$

Since the density of states for photon modes in free space is given by:

$$\rho(\omega) = \frac{\omega^2 V_0}{\pi^2 c^3} \quad (2.13)$$

The decay rate of the TLS in free-space can be written as:

$$W_{\text{free}} = \frac{\mu_{12}^2 \omega^3}{3\pi\epsilon_0 \hbar c^3} \quad (2.14)$$

meaning that it is proportional to the cube of the frequency and the square of the transition dipole moment.

### Weak coupling regime

We now imagine that the TLS is coupled and resonant to a mode  $\omega_0$  of a resonator with volume  $V$  and quality factor  $Q$ . The effect of the cavity on the TLS is not negligible anymore, however we assume that the emission of photons remains an irreversible process. This situation is commonly known as weak coupling regime. Moreover, if we accept that no external field sources are present within the resonator, the matrix element  $M_{12}$  can still be expressed according to Equation 2.11, which was obtained with no further assumptions on the environment surrounding the TLS.

On the other hand, the density of states represents the number of available modes that can accept an emitted photon and therefore is strongly dependent on the photonic environment. In this case, it can be expressed as [44]:

$$\rho(\omega) = \frac{2Q}{\pi\omega_0} \quad (2.15)$$

As a result, confining the TLS within an optical resonator can alter significantly its decay rate  $W_{\text{cav}}$  because the free-space photon modes of Equation 2.13 are redistributed into resonant optical modes. This change in the emission dynamics is conveniently quantified by a parameter called Purcell factor [47]:

$$F_{\text{p}} = \frac{W_{\text{cav}}}{W_{\text{free}}} = \frac{3(\lambda/n)^3 Q}{4\pi V} \quad (2.16)$$

where  $n$  is the refractive index of the medium inside the cavity and  $\lambda$  is the wavelength in free-space. It is important to emphasize the  $Q$  over  $V$  dependence of  $F_p$ , which is qualitatively intuitive: in fact, a longer temporal (high  $Q$ ) and tight spatial confinement of the photon in the cavity lead to a stronger impact of the resonator on the TLS spontaneous emission rate.

It is now clear that placing a quantum dot within a properly designed resonator gives the opportunity to enhance ( $F_p > 1$ , typically when the transition is resonant with a cavity mode) or suppress ( $F_p < 1$ , typically off resonance) the spontaneous emission process at certain frequencies.

### Strong coupling regime

For sake of completeness, it is worth mentioning the existence of a further coupling regime which happens when  $g \gg (K, Y)$ , i.e. when the interaction between the TLS and the photon is faster than the photon losses due to imperfect confinement or non-resonant decay. In this strong coupling regime the emission of the photon becomes a reversible process, meaning that the photon can be re-absorbed by the TLS before escaping from the cavity. In order to achieve strong coupling, cavities with very high  $Q$  factors are required to confine photons in the immediate surroundings of the quantum emitter [48, 49, 50].

### 2.4.3 Photon collection efficiency and directivity

The enhancement of the spontaneous emission rate is not the only advantage offered by photonic structures. In fact, a well-known problem for solid-state quantum light sources is to achieve high extraction efficiencies [51]: if we consider an exemplary quantum dot in a semiconductor matrix, we notice that half of the photons are emitted into the  $2\pi$  solid angle away from the extraction surface and therefore get absorbed in the substrate. Moreover, the angle of total internal reflection  $\theta_c$  at the semiconductor-air interface is usually quite small due to the high refractive index contrast (e.g for GaAs:  $\theta_c = \arcsin(n_{\text{air}}/n_{\text{GaAs}}) \approx 17^\circ$ ). As a result, the photons

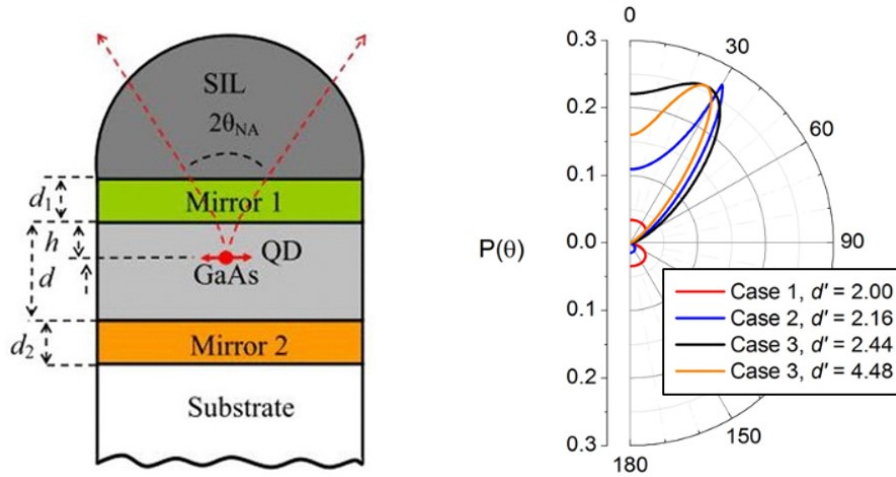


Figure 2.8: Example of broadband structure to improve the photon collection efficiency from Ref. [53]: a quantum dot is embedded in a GaAs membrane of thickness  $d$  sandwiched between two mirrors, and a solid immersion lens (SIL) is attached on the top cavity mirror (mirror 1). The polar plot shows the corresponding simulated angular power distribution of TE modes  $P(\theta)$  for 4 different values of the effective cavity length  $d' = 2dn_{\text{GaAs}}/\lambda$ .

emitted towards the surface but at larger angles remain trapped inside the sample as well, limiting typical collection efficiencies to values around 1% [52].

Integrating quantum dots into optical resonators has the additional benefit of redirecting the radiation in the direction of the cavity mode and may facilitate a more efficient collection of the emitted single photons [33]. However, this is more challenging to implement for an entangled photon source as it requires the simultaneous coupling of two transitions at different energy.

A promising alternative is offered by broadband antennas made from dielectric or semiconductor materials. Unlike optical resonators, those devices have a minimal impact on the spontaneous emission rate. Instead, their main function is to manipulate the wavefront of the emitted radiation and redirect it towards the collection optics [54]. This effect is usually quantified by the directivity, which measures how well the antenna directs radiation towards a particular direction. This parameter is defined the ratio of the radiant intensity  $U(\theta, \phi)$  in a given direction to the average

value over all directions:

$$D(\theta, \phi) = \frac{U(\theta, \phi)}{U_{\text{tot}}} = \frac{U(\theta, \phi)}{P_{\text{tot}}/4\pi} \quad (2.17)$$

An antenna that radiates equally in all directions would have effectively zero directivity, its directivity would be 1. On the other hand, the higher the directivity, the more concentrated is the beam radiated by the antenna.

In this framework, particularly interesting structures have been demonstrated by coupling quantum dots to photonic nanowires [35, 36] or solid immersion lenses (SILs) [53, 37, 38, 39], which provide a versatile and powerful method to enhance the collection efficiency in a broad range of wavelengths. Figure 2.8 shows an example of QD coupled to a broadband structure based on a solid immersion lens and the corresponding angular distribution of the radiated power  $P(\theta)$ .

# 3 | Experimental methods

This chapter gives a general overview of the methods used for growth, fabrication and characterization of the quantum emitters and devices studied in this work.

Since all the nanofabrication techniques used in the cleanroom are standard in the semiconductor processing industry, their description includes only the essential details. A comprehensive illustration of those processes can be found in Ref. [55] and [56].

## 3.1 QDs growth with Molecular Beam Epitaxy

The growth of QDs embedded in semiconductor structures requires the ability to deposit pure crystalline layers with control of the thickness at the atomic level [21]. The samples studied in Chapter 4 and Chapter 5 were grown by Molecular Beam Epitaxy (MBE), an advanced crystal growth technique that enables precise fabrication of two-dimensional layered semiconductors [57].

The MBE process takes place in an ultra-high vacuum chamber ( $\sim 10^{-10}$  mbar), which includes different effusion cells loaded with the required elements such as Ga, As, In and Al (Figure 3.1). The growth rate of those elements can be controlled by adjusting the temperature of each cell and the molecular beams can be blocked by externally controlled shutters [58]. The molecular beams ejected from the cells are directed on a commercially available substrate that, during growth, is typically heated to 450 - 650 °C and usually rotated to compensate for flux variations across its area. Under appropriate conditions, the material coming from the effusion cells can cover the wafer homogeneously with atomically thin layers of material known as monolayers (MLs). Typical deposition rates for MBE growth of QDs can be on the

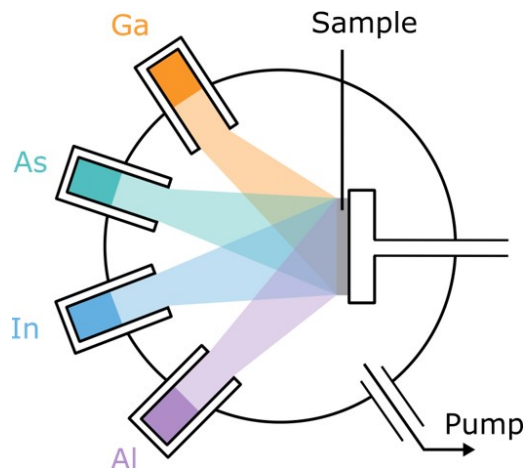


Figure 3.1: Simplified schematic of a ultra-high vacuum chamber for molecular beam epitaxy growth.

order of 1 ML/s and the growth progress is monitored in-situ using diagnostic tools such as a mass spectrometer and a beam flux gauge.

In this work we used two different types of MBE-grown quantum dots, as explained in the following subsections.

### 3.1.1 Stranski-Krastanov QDs

The sample presented in Chapter 5 (wafer W1562) was grown on a (100)-oriented GaAs substrate by Lucy Goff at the Cavendish Laboratory of the University of Cambridge. It contains InAs/GaAs dots that were self-assembled using the Stranski-Krastanov (SK) method [59].

The main steps of the SK growth process are shown in Figure 3.2. First, a GaAs buffer layer is grown on top of the substrate to reduce the surface roughness, followed by In and As deposition for the growth of QDs. The formation of SK QDs relies on the lattice mismatch between different semiconductors, which in the case of InAs and GaAs is around 7% [60]. When atomic layers of InAs are deposited on GaAs, strain builds up and, after a certain critical thickness, QD islands start to appear in order to minimize the surface tension [25]. The final result is a two-dimensional layer, called wetting layer (WL), with a plurality of randomly distributed QDs. SK InAs/GaAs QDs have shown single photon emission in various wavelength ranges, depending

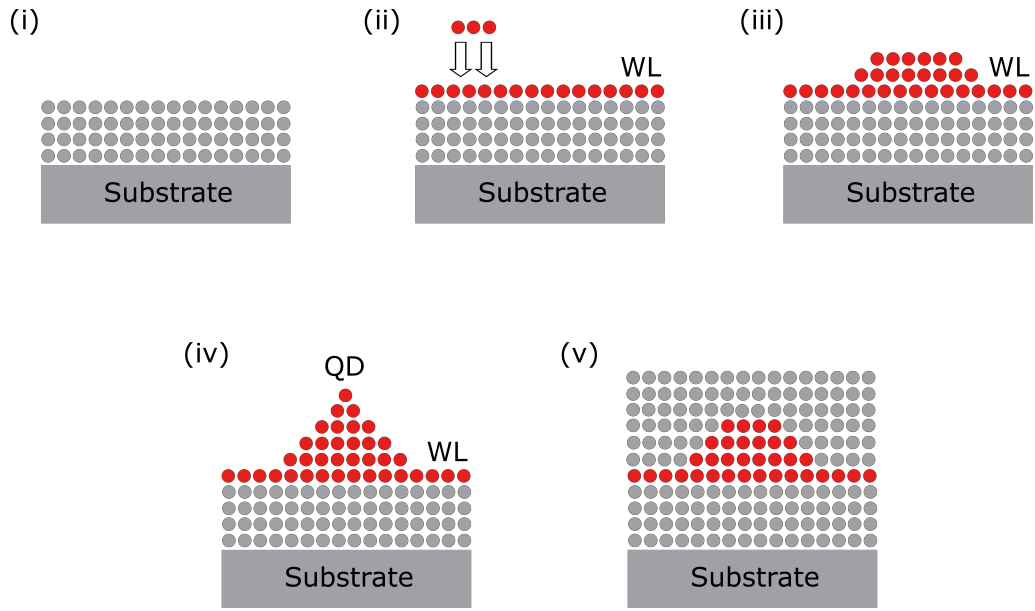


Figure 3.2: Schematic of the Stranski-Krastanov growth mode of InAs/GaAs QDs by molecular beam epitaxy. (i) An epitaxial GaAs buffer layer is grown on a commercial GaAs substrate. (ii) InAs deposition and consequent formation of the WL. (iii) Further InAs deposition leads to the formation of small QDs to minimize the surface tension (iv) The InAs deposition continues until the QDs have reached the desired size and the growth is complete. (v) QDs are capped with a layer of GaAs, which may cause changes in the dot morphology.

on their size. The size of SK dots can be adjusted by tuning the temperature and duration of the material deposition. For example, to obtain QDs emitting in the telecom O-band a constant flow of InAs is usually applied after the initial formation of the dots to push the WL to a second critical thickness and end up with bigger QDs [61]. It is important to underline that the shape of the QDs is likely to change during the capping process. As a result, AFM images (Figure 2.3) are useful to quantify the dot density, but surface dots may show a different morphology compared to the ones buried in the semiconductor matrix.

Finally it is worth mentioning that, due to technical imperfections, a small gradient in the temperature and deposition rate is always experienced during growth. As a result, the process is not perfectly homogeneous and the density and properties of QDs in the centre of the wafer are usually different from the ones at the edge. Therefore, it

is important to characterize every newly grown wafer to find the areas where the dots show the desired emission wavelength and density. In our case, this characterization was performed by cleaving the wafer and measuring photoluminescence on 3 or 5 different chips along the radial direction. The following calibration wafers have been characterized in order to optimize the growth conditions for the final sample: W1532, W1524, W1525, W1528, W1529, W1530, W1534, W1535, W1536, W1540, W1541, W1542, W1556.

### 3.1.2 Droplet Epitaxy QDs

Because of its robustness and simplicity, SK growth is very popular in the research community and has contributed to set the state of the art for quantum light sources based on semiconductor QDs [62, 63]. However, the SK method shows some intrinsic limitations such as the limited number of crystal orientations of the substrate, the limited combinations of exploitable materials leading to a limited range of emission frequencies, the difficulty of controlling the shape of the islands and the residual strain and associated built-in fields [64].

In order to overcome those limitations, there has been an increasing research interest in an alternative growth method known as droplet epitaxy (DE), which originated from Koguchi and his coworkers [65, 66]. The DE method is based on the separation of the group III and group V materials supply during the MBE growth [67]. As a result, the QD preparation consists of two distinct steps, which are summarized in Figure 3.3. First, group III metallic elements such as Ga, In, Al, are deposited on the substrate surface, leading to the spontaneous formation of nanometre-scale droplets. In fact, a compound semiconductor surface is normally terminated with group V atoms due to their strong binding energy to the substrate. After the first monolayer of group III elements is consumed by the surface group V atoms, the excess materials form metallic nanodroplets in the Volmer–Weber growth mode [68]. At this stage it is possible to control the droplet density and size by changing either the temperature of the substrate or the total amount of material deposited per unit area, although high substrate temperatures are usually preferred

to obtain high-quality materials for device development. Those nanodroplets are typically dome-shaped with the contact angle governed by the surface free energies, but different configurations of In nanocrystals with both round and square edges have been reported in literature.

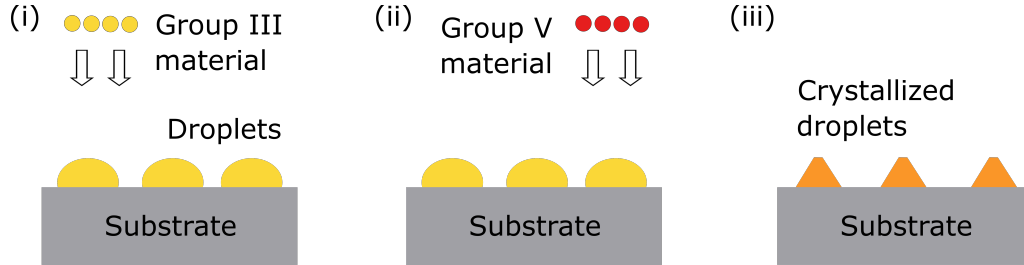


Figure 3.3: Schematic of the Droplet Epitaxy growth mode: (i) Generation of metallic droplets on the surface of the substrate by controlled deposition of a group III element (In for the QDs studied in this work) in a molecular beam epitaxy chamber. (ii) Crystallization of the metallic droplets by annealing in a group-V element atmosphere (As for the QDs studied in this work), during which each single metal droplet becomes the starting point of one nanostructure. (iii) Final result with crystallized 3D nanostructures. It is worth noting that in DE the formation of a wetting layer can be entirely avoided by controlling the surface reconstruction and composition before the droplet formation.

Once the first step is completed, the metal source is closed and the growth continues with the crystallization of the metallic droplets by irradiation of the desired non-metallic group V element, such as As, P, Sb, N. During this second step the impinging As atoms are dissolved into the liquid metal droplet, which is then crystallized by nucleation at the interface with the surface [64]. As a result, each single metal droplet becomes the starting point of one nanostructure whose shape and topology can be controlled by varying the parameters of the process [69]. The morphological features of DE QDs are then reflected in their optical properties.

The QDs studied in Chapter 4 (wafer C200527) were grown using this method on (111)-oriented GaAs substrates by Artur Tuktamyshev at the University of Milan Bicocca. The following calibration wafers have been characterized in order to optimize the growth conditions for the final sample: C200226a, C200226b, C200219a, C200219b, C200226, C200227, C200228, C200603.

## 3.2 Numerical FEM simulations

Numerical simulations are useful tools to study the behaviour of photonic devices and optimise the choice of the design parameters before their fabrication on samples containing QDs. In this work, we employed simulations based on the finite element method (FEM) to design the circular Bragg gratings (CBGs) presented in Chapter 5 and 6.

For the majority of geometries and problems it is not possible to solve analytically partial differential equations (PDEs) such as the wave equation. Instead, by discretizing the domain, one can create an approximation of the PDEs called numerical model equations, which can be solved with numerical methods. The combination of the local solutions to the numerical model equations will give, in turn, an approximation of the real solution to the PDEs over the whole domain of interest [70]. A detailed discussion of the finite element method can be found in Ref. [71] and Ref. [72].

The numerical simulations presented in this work were performed with the Wave Optics module of the commercial software COMSOL Multiphysics [73]. Since the feature sizes of the devices are comparable to the wavelength of interest, we decided to use the frequency domain interface. Figure 3.4 shows an example of frequency domain study applied to a CBG: a CAD model of the desired simulation domain is first created in the software (a) and subsequently divided into smaller tetrahedral mesh elements (b). Then, the time-harmonic wave equation for the electric field:

$$\nabla \times (\mu_r^{-1} \nabla \times \mathbf{E}(\mathbf{r})) - k_0^2 \epsilon_r \mathbf{E}(\mathbf{r}) = 0 \quad (3.1)$$

is solved over each mesh elements to calculate the global electric field distribution at the desired frequency in the near-field region ( $r < \lambda$ ). Finally, the electric field distribution in the far-field region ( $r > 2\lambda$ ) can be extracted from the near-field profile using the Stratton-Chu formula, which for 3D models is:

$$\mathbf{E}_f = \frac{jk}{4\pi} \mathbf{r}_0 \int [\mathbf{n} \times \mathbf{E} - \eta \mathbf{r}_0 \times (\mathbf{n} \times \mathbf{H})] e^{jk\mathbf{r} \cdot \mathbf{r}_0} dS \quad (3.2)$$

Using Equation 3.2 to extract the far-field profile makes it possible to calculate the collection efficiency into a microscope objective or the mode coupling in a single

mode optical fibre without extending too much the dimensions of the simulation domain.

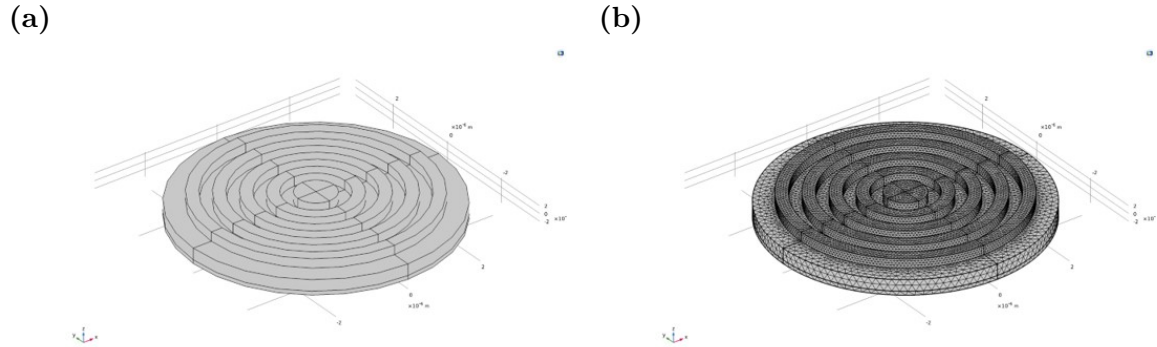


Figure 3.4: (a) Example of a 3D simulation domain for a circular Bragg grating (CBG). The near-field air domain above the CBG is not included in this example to keep the device visible. (b) Domain meshed with tetrahedral elements.

It is important to mention that, in general, optical problems require to resolve the optical wavelength of interest with at least three discrete mesh elements. Refining the mesh by decreasing the size of those elements improves the accuracy of the global solution, but needs longer computational time and larger memory [70]. Therefore, optimizing the mesh is one of the most critical steps in numerical simulations.

Since typical computational requirements for 3D simulations are quite demanding, symmetry properties can be exploited in order to simplify the model. By cutting the devices along the symmetry planes and imposing the proper boundary conditions, the numerical equations can be solved on just a quarter of the domain. This approach is extremely convenient during design optimisations, which usually require many different parametric sweeps.

### 3.3 Device fabrication

This section describes the methods used for the fabrication of the Circular Bragg Gratings presented in Chapter 5. Some specific details of the individual fabrica-

tion steps are considered privileged information and therefore not included in the description.

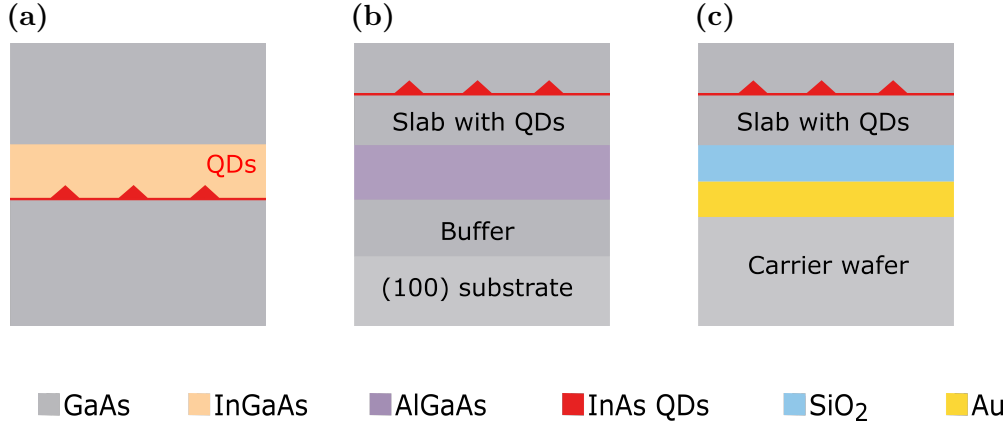


Figure 3.5: (a) Structure of the 240nm thick GaAs slab, incorporating SK InAs/GaAs QDs capped with 5 nm of InGaAs. (b) Schematic of the initial sample structure grown by MBE on GaAs (100) substrate. (c) Schematic of the final sample structure after the flip chip processing, incorporating a backside Au mirror. These drawings are intended to provide an intuitive representation of the wafer structures and the thickness of the layers is not to scale.

The sample used for the fabrication of CBGs is a 240 nm thick GaAs slab incorporating InAs/GaAs SK QDs and a thin InGaAs layer (Figure 3.5a). The sample was initially grown by MBE on a GaAs (100) substrate (Figure 3.5b): the epitaxial structure starts with a 250 nm GaAs buffer, which helps reducing the surface roughness and recovering good crystallinity [74]. Such a buffer is followed by a 200 nm thick  $\text{Al}_{0.8}\text{Ga}_{0.2}\text{As}$  sacrificial layer, and then by the lower half (120 nm) of the GaAs slab. Since  $\text{Al}_{0.8}\text{Ga}_{0.2}\text{As}$  and GaAs are almost lattice-matched ( $a = 5.653 \text{ \AA}$  for GaAs and  $a = 5.669 \text{ \AA}$  for  $\text{Al}_{0.8}\text{Ga}_{0.2}\text{As}$  [75]), they can be grown in sequence with smooth interfaces and no particular limitations on their thickness. In order to end up with a layer of SK quantum dots in the middle of the slab, InAs was deposited on the lower half of the slab. The dots were then capped with 5 nm of InGaAs, which is critical to push the emission wavelength to the telecom O-band because of its lower

bandgap energy compared to GaAs. Finally, another layer of 115 nm of GaAs was grown on top of the InGaAs to complete the slab.

To improve the brightness of the QDs we decided to follow an established approach and integrate in the structure of the sample a backside broadband gold mirror that could redirect towards the collection optics the fraction of photons that usually gets dispersed in the substrate (Figure 3.5c). This solution has been successfully implemented in multiple devices at short wavelength [76, 77, 38]. Nevertheless, to increase the amount of material available for the fabrication of the CBGs we chose to operate on wafer scale, which required the development of a flip-chip post-growth process described in the next subsection.

### 3.3.1 Flip-chip process: wafer bonding and substrate removal

The flip-chip post-growth processing consists of a thermocompression Au-Au wafer bonding followed by mechanical lapping and a selective wet etching to remove the original GaAs substrate.

The main steps of the process are shown in Figure 3.6: first, a film of SiO<sub>2</sub> is deposited on the GaAs slab by plasma enhanced chemical vapour deposition (PECVD). This layer acts as a diffusion barrier for the gold and prevents the penetration of any plasmonic effect within the device, avoiding a direct semiconductor-gold interface. In order to enable the Au-Au bonding, approximately 500 nm of Au are evaporated on top of the SiO<sub>2</sub> and on a bare GaAs (100) wafer that will act as a carrier substrate. Then, the two metallic surfaces are brought into atomic contact applying force and heat simultaneously in order to generate a continuous bond between the interfaces by solid-state diffusion [78].

After the bonding, the majority of the original GaAs substrate is reduced to a thickness of 20-25  $\mu\text{m}$  by mechanical lapping and polishing and then etched in a solution of citric acid (C<sub>6</sub>H<sub>8</sub>O<sub>7</sub>) and hydrogen peroxide (H<sub>2</sub>O<sub>2</sub>) with ratio 5:1. This etching step is highly selective [79] and stops at the AlGaAs interface. A final dip in

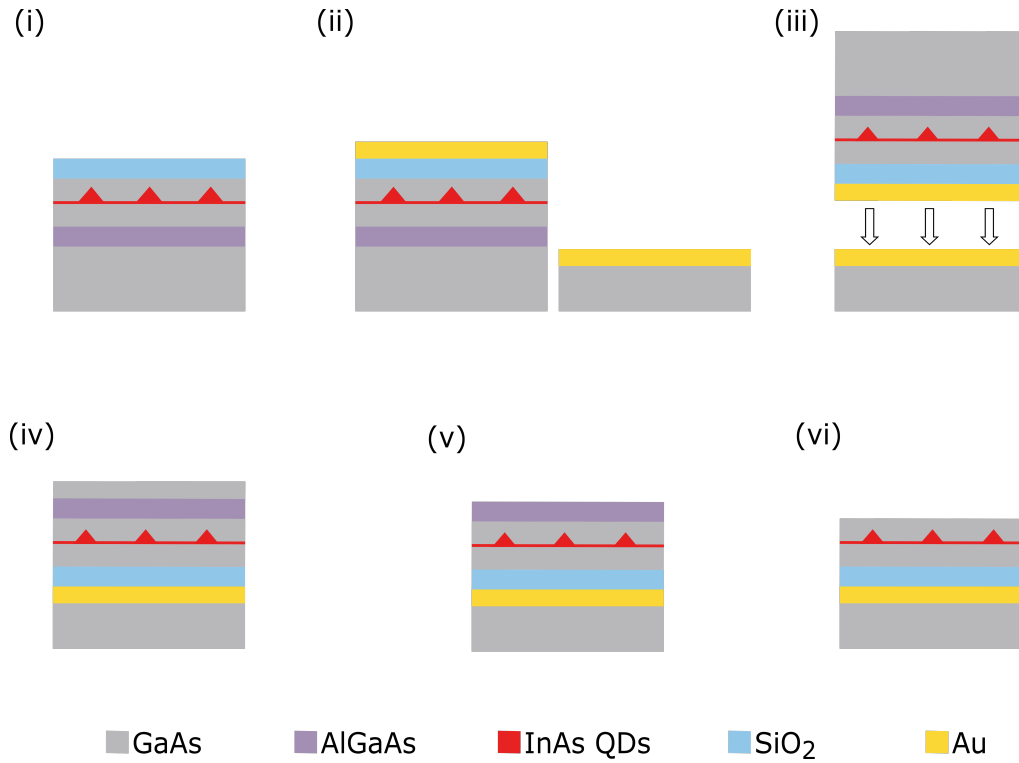


Figure 3.6: Schematic representation of the processing steps. (i) A film of SiO<sub>2</sub> is deposited by PECVD on the GaAs slab with QDs. (ii) A layer of gold is evaporated on top of both the SiO<sub>2</sub> and the carrier wafer. (iii) The sample is flipped and bonded to the carrier wafer using thermocompression Au-Au bonding. (iv) The majority of the original GaAs substrate is removed by mechanical lapping and polishing. (v) The remaining 20-25  $\mu\text{m}$  of GaAs are etched in a solution of citric acid (C<sub>6</sub>H<sub>8</sub>O<sub>7</sub>) and hydrogen peroxide (H<sub>2</sub>O<sub>2</sub>) with ratio 5:1. The solution is highly selective and the etching stops at the interface with the AlGaAs layer. (vi) The AlGaAs sacrificial layer is etched in a solution of diluted HCl, yielding the final sample structure. This second etching step is also highly selective and stops at the interface with the GaAs slab.

diluted HCl dissolves the AlGaAs, yielding the final structure which includes the GaAs slab with QDs, a SiO<sub>2</sub> film and the Au broadband backside mirror bonded to the carrier wafer. The whole process is performed on wafer scale, which makes it time-efficient and minimizes the loss of material due to side-etching effects. Once the removal is complete, the wafer can be cleaved and pre-characterized in order to find a suitable area for the fabrication of circular Bragg gratings by electron beam lithography.

### 3.3.2 Electron beam lithography

Electron beam lithography (EBL) is a powerful technique for the fabrication of nanostructures that are too small to be defined using conventional photolithography, with resolution capabilities of less than 10 nm that have been repeatedly demonstrated [80] [81]. It works by scanning a tightly focused beam of electrons on a sample covered with a thin electron-sensitive film (Figure 3.7), which changes its molecular structure when exposed and enables selective removal of the exposed or non-exposed regions. EBL offers the advantage of direct writing because patterns are written directly from CAD design files, without the need of a physical mask. This enables frequent and cost-free changes and makes it ideal for experimenting and optimising different designs. On the other hand, EBL is more complex than conventional photolithography and has lower throughput, since the beam has to write one device at a time.

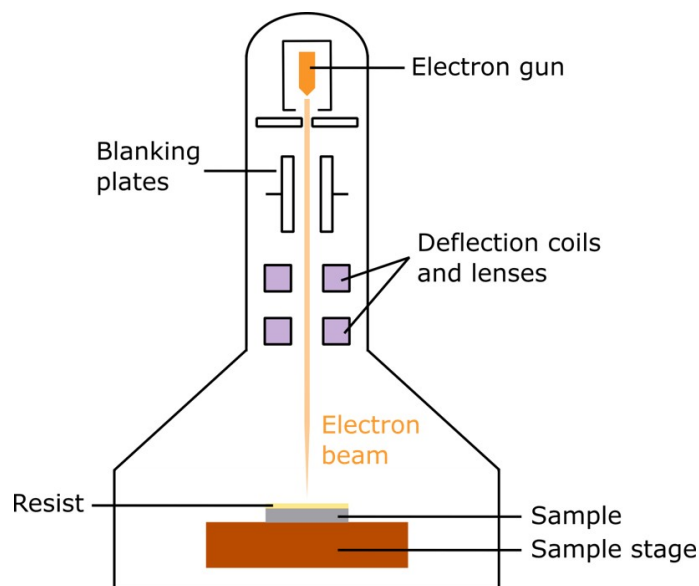


Figure 3.7: Schematic illustration of an electron beam lithography system: an electron gun generates a beam of free electrons, which is accelerated, guided and focused on the sample by a set of electromagnetic lenses and deflection coils. The sample is covered with an electron-sensitive resist which changes its molecular structure when exposed to the electron beam. The movement of the converged electron beam and the movement of the stage are controlled according to the pre-defined lithography pattern.

The main processing steps for the fabrication of nanophotonic devices with EBL are shown in Figure 3.8a. First, the substrate is spin coated with a thin film of an electron sensitive polymer, known as resist. The subsequent exposure to the electron beam changes the molecular structure and therefore the solubility of the film: in case of positive tone resist the molecular bonds are broken, creating short polymer chains that are easily dissolved by an appropriate solvent known as developer. On the other hand, a negative tone resist is cross-linked, becoming more difficult to dissolve in a developer [82]. Once the development phase is completed, the desired mask is ready for the pattern transfer onto the underlying substrate by dry or wet etching.

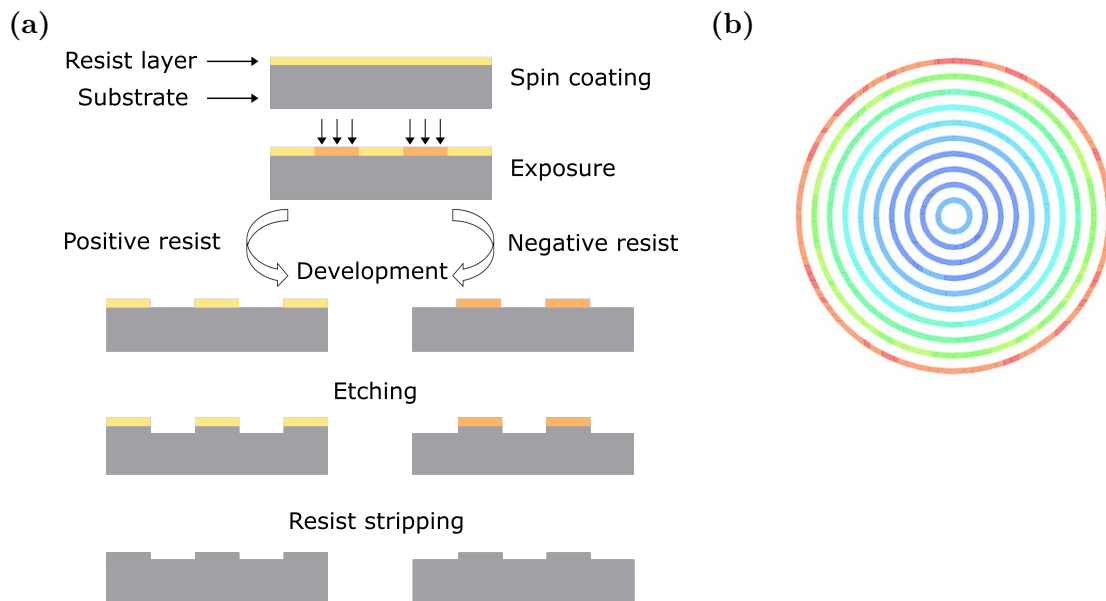


Figure 3.8: (a) Schematic of the main processing steps for the fabrication of nanophotonic structures with electron beam lithography. (b) Example of proximity correction applied to a CBG written on ZEP 520A (positive resist). The corrected dose is represented by the colour of the regions: the blue areas are written with the lowest dose and red areas with the highest.

The circular Bragg gratings presented in this work were written by Jonathan Griffiths at the Cavendish Laboratory of the University of Cambridge using a Leica BV6 UHR system, with a beam voltage of 100 kV, a minimum beam diameter of 3 nm and an in-line resolution of 10 nm (25 nm with 500  $\mu\text{m}$  field). The electron

beam resist we chose was ZEP 520A (Zeon) [83], a positive tone resist that allows for feature sizes down to 10 nm [84] and exhibits high dry etch resistivity [85].

One of the major complexities of EBL is given by the proximity effects during the exposure, i.e. the unwanted exposition of the resist due to backscattered and secondary electrons, which can cause deviations from the original design [86]. These processes are material-dependent and, before writing the pattern, they need to be studied with dedicated simulations when the desired structures require high-resolution. It is then possible to compensate for those effects (proximity correction) by adjusting the exposure dose across the pattern [87]. Figure 3.8b shows an example of proximity correction applied to a CBG pattern written on ZEP 520A, where the colour represents the adjusted dose. After the exposure to the electron beam, the resist was developed in n-amyl acetate, which causes selective removal of the exposed ZEP 520A and produces the desired mask for the following pattern transfer by dry etching.

### 3.3.3 Dry etching and resist stripping

Etching is a step of fabrication where layers of material are removed from the surface of the sample. This can be achieved using either physical or chemical processes. Physical removal is based on directional bombardment of the sample with high-energy particles, while chemical processes rely on interactions with acids or other reactive substances.

It is also important to distinguish between wet and dry etching: wet etching uses liquid chemicals to attack the surface of the substrate, while dry etching can exploit plasma, gas or ion beam and involve both physical and chemical processes. In terms of results, wet etching can be relatively fast and show high selectivity for certain materials, but it is generally isotropic by nature. On the other hand dry etching offers the advantage of directionality, which helps producing straight edges. Therefore, the appropriate etching process is usually chosen according to the materials involved and the desired resulting profile. When performing dry etching, one should also carefully select a proper type of mask. In fact, electron beam resist can be used for

some processes but it will be attached by the etching agent and may be partially or completely removed. Its suitability will ultimately depend on the duration of the process and the target etch depth. In cases that involve long and deep etching, resist is usually not appropriate and it is necessary to use a hard mask made of metallic or dielectric material.

In general, the fabrication of circular Bragg gratings requires a highly directional etching mechanism resulting in straight vertical side walls. Also, those etched surfaces should be as smooth as possible, without any relevant damage. Therefore, we chose a dry process based on an Ar/SiCl<sub>4</sub> inductively coupled plasma (ICP). Since the target etch depth was only 240 nm, the process could be performed directly on the resist mask. After the exposure to plasma during dry etching, the remaining resist is usually hardened and requires an appropriate mechanism to be stripped. The residual ZEP 520A was first exposed to deep UV radiation for a few minutes in order to decompose the polymer and then dissolved at room temperature into Microposit Remover 1165 (Micro Resist Technology) [88], resulting in a clean sample surface.

#### 3.3.4 Quality control

After the fabrication steps described above, a subset of circular Bragg gratings was inspected with a scanning electron microscope (SEM) to evaluate the quality of the resulting devices (Figure 3.9). A qualitative evaluation of the SEM pictures provided information about the etch depth and the profile of the side walls, while a deeper analysis with the ImageJ software package was necessary to measure the size of the fine features and their variation across the chip.

The results of the image analysis were then fed back into the design and fabrication process to optimize each individual step, compensate for processing bias and improve the resulting properties of the devices.

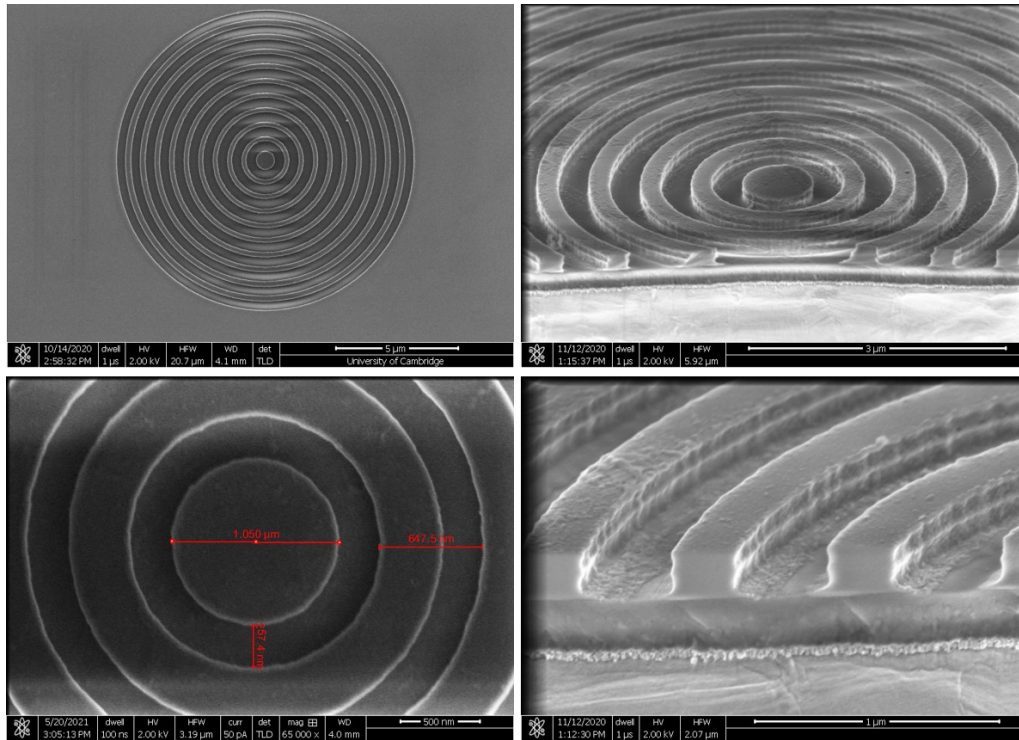


Figure 3.9: SEM pictures of CBGs fabricated on a GaAs slab, with image analysis showing the size of the fine features and an example of cross-section to evaluate the profile of the etched trenches.

## 3.4 Optical characterization

The optical properties of the quantum dots and devices presented in this work were characterized with the spectroscopic techniques described in the following subsections.

### 3.4.1 Micro-PL spectroscopy

Photoluminescence (PL) spectroscopy measures the emission spectrum of a specimen under optical excitation. In the case of quantum emitters, it is often called micro-PL or  $\mu$ PL because a collection spot with a diameter of a few microns is typically used. In general, it involves the excitation of charge carriers by a laser source and the collection of the photons emitted by their recombination. Micro-PL measurements can be used to identify transitions in quantum emitters, to study their power dependence and to

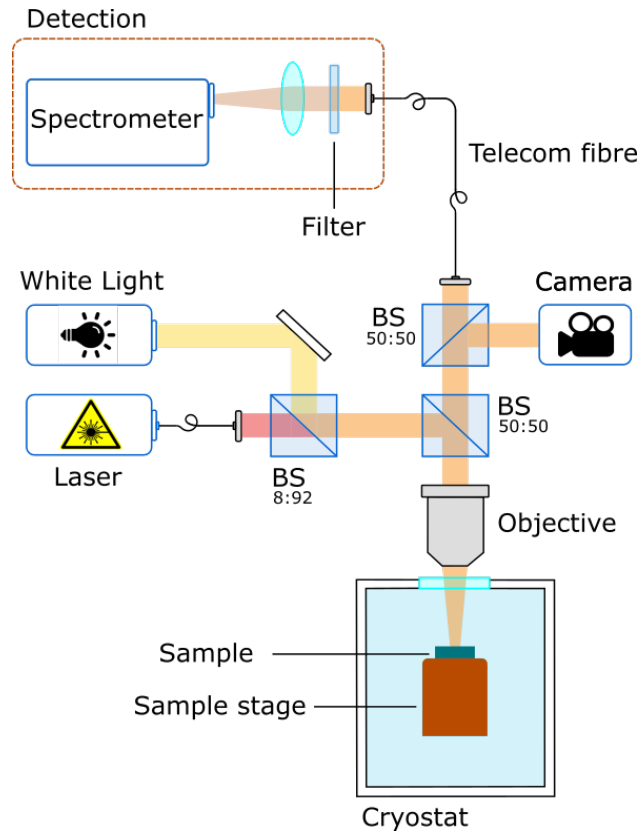


Figure 3.10: Schematic of the home-built setup used for the micro-PL experiments on InAs QDs. Depending on the particular measurement carried out, some additional optical components such as filters, linear polarisers (LP), half-wave plates (HWP) or quarter-wave plates (QWP) might be added in the beam path.

probe cavity modes in photonic devices. They are also used for the characterization of newly grown samples, when it is important to determine the density and emission wavelength of QDs across the wafer.

All micro-PL experiments on InAs QDs have been carried out in a home-built setup in Cambridge. A schematic of the setup is shown in Figure 3.10: the sample is placed in a closed-cycle cryostat able to reach temperatures down to 4K. In order to ensure good thermal contact, it is firmly attached to the cold finger using conductive silver paint and an integrated heater makes it possible to control the temperature between 4K and 300K. The sample is excited from above using laser light that is focused by a vertically mounted microscope objective with a numerical aperture  $NA=0.5$ . The laser used is either a continuous-wave (CW) laser diode emitting at 785

nm, or a pulsed laser diode emitting pulses at a central wavelength of 780 nm, with adjustable repetition rate (10 - 80 MHz) and pulse width  $< 60$  ps around threshold. The objective is mounted on a three-axis translation stage for the positioning of the excitation and collection spots. In order to navigate the sample, its surface is illuminated by a broadband LED emitting around 1310 nm and the live image is recorded by an InGaAs camera. The emission is collected through the same objective, filtered with a long pass filter to remove any residual laser signal and coupled into a spectrometer with cooled InGaAs detector. Finally, a personal computer records the signal and displays the live image and PL spectrum.

An important task in the PL characterization of QDs is to identify transitions corresponding to neutral excitons and to quantify their fine structure splitting (FSS), which creates a decoherence mechanism that complicates entanglement based experiments. As mentioned in Section 2.3.2, both the X and XX transitions are usually linearly polarized doublets with components parallel to the crystallographic axes of the substrate and can be recognized using polarization-resolved spectroscopy. In fact, since the polarization of the emitted photon correlates with its energy, the FSS can be quantified by including a rotating half-wave plate (HWP) and a fixed linear polarizer (LP) in the collection arm of the microscope and measuring the resulting shift in energy at the spectrometer. Occasionally, we also used a variation of this method, which employs a rotating quarter-wave plate (QWP) and can provide additional information such as the birefringence accumulated in optical fibre, as explained in [31].

The identification of the trions as  $X^+$  and  $X^-$  is less straightforward. In general, the  $X^+$  and  $X^-$  lines are expected to be at higher and lower energies than the neutral exciton due to the Coulomb interaction [89]. For QDs embedded in a pin doped structure, this prediction can be verified by observing the shift in relative intensity from  $X^+$  and  $X^-$  for increasing temperature.

### 3.4.2 Time-resolved spectroscopy

The temporal evolution of the excited states in quantum emitters can be studied using time-resolved spectroscopy. The measurements of luminescence lifetimes presented in this work are based on a statistical process known as time-correlated single photon counting (TCSPC), a powerful technique that detects single photons generated under a periodic excitation signal and measures the time delay between the excitation pulses and the detection events [90].

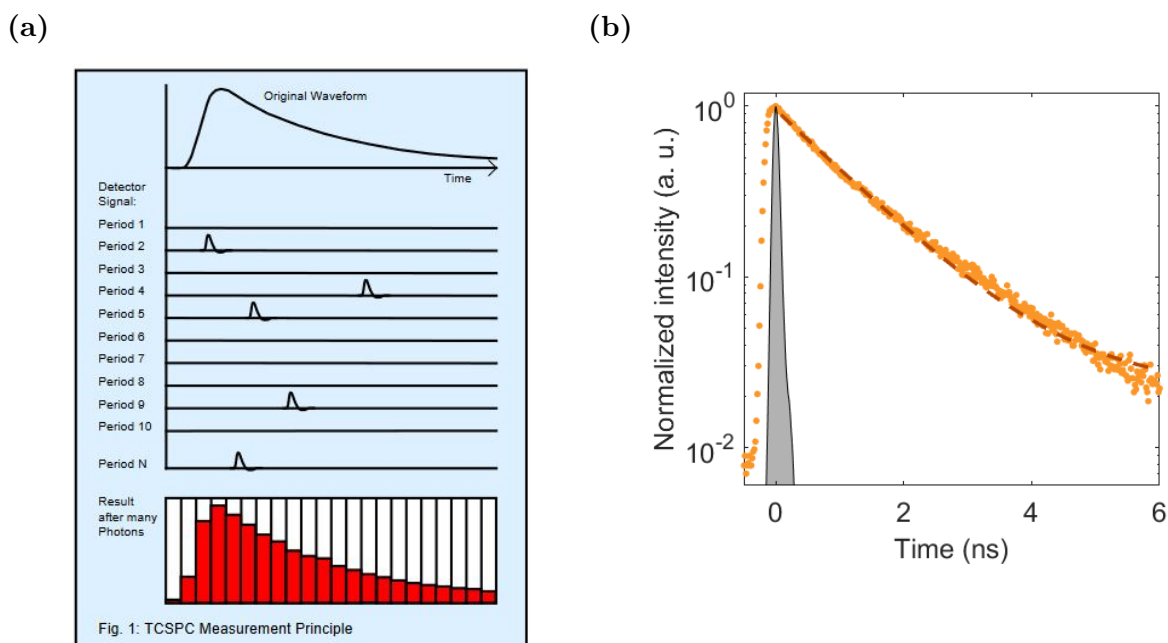


Figure 3.11: (a) Schematic representation of the TCSPC measurement principle, from Ref. [91]. The detector signal consists of a train of randomly distributed pulses due to the detection of individual photons. When a photon is detected, the time of the corresponding detector pulse is measured and recorded in a histogram. After a large enough number of events, the waveform of the optical pulse builds up in the histogram. (b) Exemplary lifetime of a quantum dot transition measured with TCSPC under pulsed laser excitation at 40 MHz. The instrument response function of the setup (IRF, grey area) is determined by the width of the laser pulses and by the response of the electronics and the detectors. The dashed line represents the fit of the experimental data with a single exponential decay function.

The principle of TCSPC is represented in Figure 3.11a: multiple measurements of single-photon events are discretized in time and combined to form a histogram. In fact, for weak and high-repetition rate signals such as luminescence from a quantum emitter under pulsed laser excitation, the light intensity is usually so low that the probability to detect one photon in one signal period is much less than one and the detection of multiple photons can be neglected [91]. Every photon measured by the detector contributes to build the photon distribution and, when the number of events recorded is large enough, the histogram reproduces the profile of the investigated curve.

In the time-resolved measurements performed in this work, the sample is excited with a pulsed laser and the emitted light is filtered with a diffraction grating. The photons belonging to the transition of interest are then detected by a superconducting nanowire single photon detector (SNSPD). An electronic photon counting module records the counts on the detector as a function of the time delay with respect to the trigger signal given by the laser. Figure 3.11b shows an example of decay-time of a single quantum dot transition measured under pulsed laser excitation at 40 MHz. The associated lifetime can then be extracted from the exponential fit of the decaying portion of the curve (dashed line). The resolution of time-resolved spectroscopy, represented by the grey area in Figure 3.11b, depends on the characteristics of the particular PL setup used, since it is determined by the width of the laser pulses and the response of the electronics and detectors.

### 3.4.3 Hanbury Brown and Twiss interferometry

The photon statistics of quantum emitters is usually studied with photon correlation measurements using the Hanbury, Brown and Twiss (HBT) setup. This setup is similar to the one used for the time-resolved measurements described in the previous subsection. However, here the light filtered by the monochromator is split with a 50:50 beam splitter and detected by a pair of single photon detectors (Figure 3.12a). A TCSPC system records the photon coincidences as a function of the delay between the detection events on the two detectors.

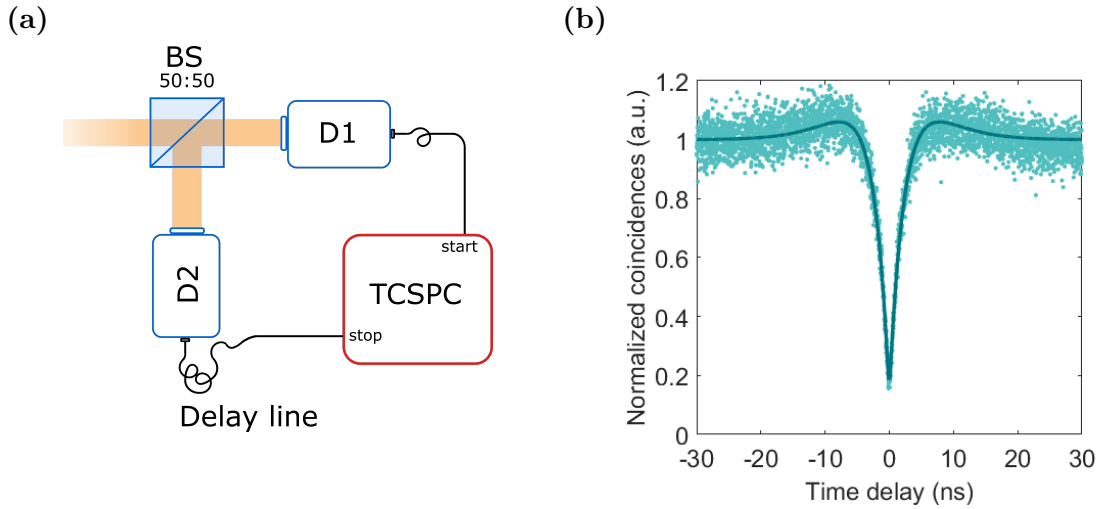


Figure 3.12: (a) Schematic of a Harbury, Brown and Twiss setup: the incoming photons are split with a 50:50 beam splitter and directed towards a pair of single photon detectors (D1 and D2). A TCSPC system records the time-resolved histogram of photon coincidences. (b) Example of second order correlation of a quantum dot transition measured under CW laser excitation. The solid line represents the fit of the experimental data and the value of  $g^{(2)}(0) = 0.19$  demonstrates the single-photon nature of the QD emission.

For low intensities, the histogram built by adding those coincidences (Figure 3.12b) gives an accurate estimate of the second order correlation function  $g^{(2)}(\tau)$ , which describes the correlation between the intensity of the light field  $I$ , with that after a delay  $\tau$  [25, 92]:

$$g^{(2)}(\tau) = \frac{\langle I(t)I(t + \tau) \rangle}{\langle I(t) \rangle^2} \quad (3.3)$$

After the detection of a photon at  $t = 0$  by the first detector, the probability of recording a photon at  $t = \tau$  with the second detector - and therefore the value of  $g^{(2)}(0)$  - is directly correlated to the statistical nature of the light source. For example, a perfectly coherent source will give  $g^{(2)}(\tau) = 1$  for every  $\tau$  since  $I(t) = I(t + \tau)$ . A thermal or chaotic source with high probability of multi-photon states in its statistics will give  $g^{(2)}(0) > 1$ , meaning that there is an increased probability that the detectors would click simultaneously.

On the other hand, for an ideal single-photon source  $g^{(2)}(0) = 0$ . In fact, this source cannot produce more than one photon per excitation period, hence the detectors cannot click simultaneously. However, in experimental measurements,  $g^{(2)}(0)$  is always greater than zero because of multiphoton events related to the background noise. The condition  $g^{(2)}(0) < 0.5$  is usually considered the threshold to demonstrate single-photon emission. In fact, it can be demonstrated that the second order correlation at zero delay for the combination of  $N$  ideal single photon sources can be expressed as [93]:

$$g^{(2)}(0) \simeq 1 - \frac{1}{N} \tag{3.4}$$



# 4 Cavity-enhanced InAs QDs emitting at telecom wavelength grown on GaAs(111)A

This chapter presents the development of InAs/InAlAs droplet epitaxy QDs emitting in the telecom O-band within a DBR microcavity grown on a vicinal ( $2^\circ$  miscut) GaAs(111)A substrate. The first part of the chapter describes the growth and optical characterization of the sample. In the second part we report the results of numerical simulations under the framework of the empirical pseudopotential and configuration interaction method that were employed to study the impact of the miscut angle on the optical properties of the QDs. The epitaxial sample studied in this work was grown by Artur Tuktamyshev from the research group led by Prof. Stefano Sanguinetti at the University of Milan Bicocca. The numerical simulations were carried out by Geoffrey Pirard from the group led by Prof. Gabriel Bester at University of Hamburg.

## 4.1 Introduction

Single and entangled photon emitters are fundamental building blocks for emerging technologies such as quantum communication protocols and quantum networks [94, 95]. In this framework, sources of entangled photon pairs based on the biexciton (XX) – exciton (X) recombination cascade in semiconductor quantum dots [31, 96, 97] offer multiple advantages such as electrical control, tuneability and integration with various photonic structures including waveguides, cavities or microlenses [30, 28, 98,

34, 99, 38, 39]. However, quantum dots typically show a fine structure splitting (FSS) larger than the natural linewidth of the excitonic transitions [26, 100], which is caused by anisotropies in their shape or composition and complicates entanglement-based experiments. One of the possible solutions for the development of highly symmetric QDs with low FSS is to self-assemble them on (111)-oriented substrates due to the natural  $C_{3v}$  symmetry of the surface [101, 102].

Moreover, for long-distance quantum communications and integration with the existing fiber infrastructure it is necessary to select a material system that provides emission at telecom-wavelength, such as InAs/GaAs or InAs/InP QDs [103, 104]. It is worth noting that InAs QDs cannot be grown on GaAs (111) surfaces with the common Stranski-Krastanov (SK) method. Instead, they require the more advanced Droplet Epitaxy (DE) technique [64] which, as explained in Section 3.1.2, relies on the formation of group-III metal droplets followed by crystallization in a group-V atmosphere.

The formation of telecom-wavelength InAs/InAlAs QDs with FSS as low as 16  $\mu\text{eV}$  on GaAs(111)A has been recently demonstrated [105]. However, previous works on (100) substrates suggest that incorporating those emitters in a one-dimensional microcavity could significantly improve the photon collection efficiency and generate sufficient signal intensity for applications, [106, 107, 108]. Unfortunately, the deposition of distributed Bragg reflectors (DBRs) on singular (111) substrates presents further complications because very low growth rates below 0.03 nm/s are usually required to obtain flat epilayers [109].

In this chapter we demonstrate self-assembly of InAs/InAlAs DE QDs emitting in the telecom O-band within a DBR microcavity grown on a vicinal ( $2^\circ$  miscut) GaAs(111)A substrate. Thanks to the presence of the miscut, the growth rate can be up to one order of magnitude higher ( $\approx 0.14 - 0.28$  nm/s) and therefore similar to the ones used on standard GaAs(100) [110, 111]. Moreover the propensity of twin defects in the AlGaAs layers, which often limit the quality of structures grown on singular (111) substrates [110], is strongly reduced.

## 4.2 Sample growth

The sample (wafer C200527) was grown by Artur Tuktamyshev at the University of Milan Bicocca. The epitaxial structure (Figure 4.1a) was deposited on an undoped vicinal GaAs(111)A substrate with  $2^\circ$  miscut along the  $[\bar{1}\bar{1}2]$  direction in a solid source MBE system. After a GaAs buffer layer, a bottom DBR with 25 repeats of  $\lambda/4$   $\text{Al}_{0.5}\text{Ga}_{0.5}\text{As}/\text{GaAs}$  layers was grown at  $600^\circ\text{C}$  using deposition rates of 0.28 nm/s and 0.14 nm/s respectively. Such a DBR was designed provide high reflectivity for a wavelength range centred around 1310 nm and its morphology (Figure 4.1b) was optimized for the subsequent growth of InAlAs metamorphic buffer layer (MMBL) and DE QDs. The relatively low 50% Al concentration in the  $\text{Al}_{0.5}\text{Ga}_{0.5}\text{As}$  layers was chosen to obtain the best compromise between refractive index contrast and low surface roughness. In fact, we noticed an increased propensity of stacking fault and twin defects for high Al content caused by the lower mobility of Al adatoms compared to Ga [110].

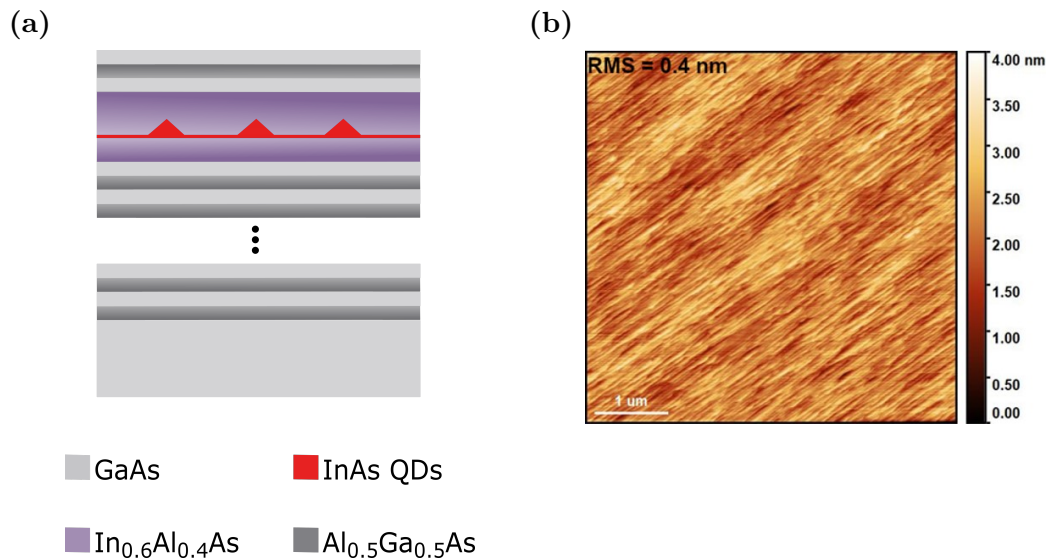


Figure 4.1: (a) Schematic drawing showing the layer structure of the sample. (b) AFM scan showing the topography of the  $\text{Al}_{0.5}\text{Ga}_{0.5}\text{As}/\text{GaAs}$  DBR structure grown on vicinal GaAs(111)A substrate.

Next, DE InAs QDs with an approximate density of  $1 \times 10^8 \text{ cm}^{-2}$  were formed in the middle of a  $\lambda/2$  cavity consisting of 201.6 nm of  $\text{In}_{0.6}\text{Al}_{0.4}\text{As}$  by supplying 1 ML (monolayer) of In at  $370^\circ\text{C}$  with a deposition rate of 0.003 nm/s and then crystallizing for 8 minutes in  $\text{As}_4$  atmosphere at  $300^\circ\text{C}$ . During the In deposition the residual  $\text{As}_4$  beam equivalent pressure (BEP) was kept below  $3 \times 10^{-9}$  torr. The  $\text{As}_4$  valve was then opened for the crystallization step, resulting in a BEP of  $3 \times 10^{-5}$  torr. These parameters are similar to those previously developed for growth on singular GaAs(111) substrates. Finally, a weakly reflective top mirror consisting of three  $\lambda/4$  layers (GaAs/  $\text{Al}_{0.5}\text{Ga}_{0.5}\text{As}$ / GaAs) was deposited with the same conditions used for the bottom DBR.

## 4.3 Experimental results

The sample was characterized using the PL setup described in Section 3.4.1. Unless stated otherwise, the measurements presented below were taken at a cryogenic temperature of approximately 5K.

### 4.3.1 Reflectivity measurements

The asymmetric cavity described in the previous section was designed to limit the photon leakage into the substrate and direct the emitted photons towards the collection optics. As shown in Figure 4.2a, the bottom DBR is meant to provide a reflectivity  $> 90\%$  for a broad wavelength range in the telecom O-band and the structure supports a cavity mode centred at 1310 nm.

In the first step of the characterization process we probed the presence of the expected cavity mode using reflectivity measurements: we illuminated the devices with uncollimated light emitted by an O-band broadband LED source ( $\sim 70$  nm FWHM) and recorded the reflected signal with the spectrometer. In order to cancel the effects of the wavelength dependence in the LED emission, in some of the optics and in the efficiency of the detector, the signal collected from the sample was normalized by the signal reflected by a gold mirror. As reported in Figure 4.2b, the

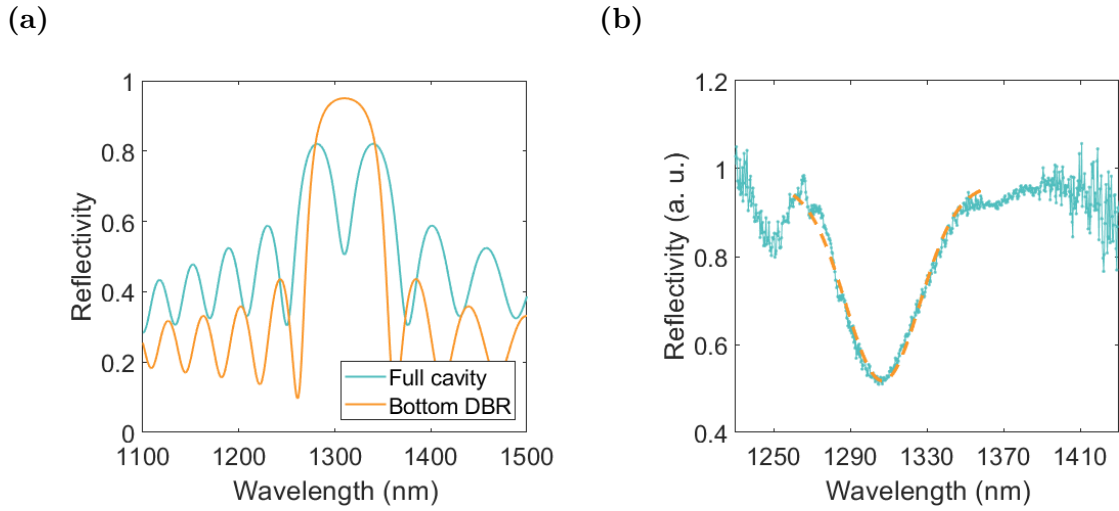


Figure 4.2: (a) Reflectivity of the bottom DBR mirror and the optical cavity simulated with the transfer matrix method. (b) Reflectivity measurement taken on the optical cavity and corresponding Gaussian fit (dashed line), showing a mode centered at 1307 nm with FWHM = 39 nm.

dip in the reflectance spectrum confirms the existence of a cavity mode at the desired wavelength. The dashed line represents the fit with a Gaussian curve centered at 1307 nm (39 nm FWHM), only 3 nm away from the design value.

### 4.3.2 Micro-PL measurements

Figure 4.3a shows a typical O-band photoluminescence spectrum from the sample. The comparison with an exemplary PL measurement taken in the same setup on InAs/InAlAs QDs grown without DBR mirrors (Figure 4.3b) confirms that the presence of the optical cavity leads to an enhancement of the signal intensity by a factor  $> 5$ . The FWHM of the spectral lines is extracted with a Gaussian fit as shown in Figure 4.3c. Fitting 30 different transitions reveals no correlation between the emission wavelength and the linewidth, which varies between 100  $\mu\text{eV}$  and 550  $\mu\text{eV}$  (Figure 4.3d). Those rather broad linewidths are consistent with previously reported values [105] and originate from the presence of point defects and threading dislocations in the InAlAs barrier layers. We also notice an improvement in the

signal/background ratio and an important reduction in the density of spectral lines, which makes it possible to isolate the emission pattern of single QDs.

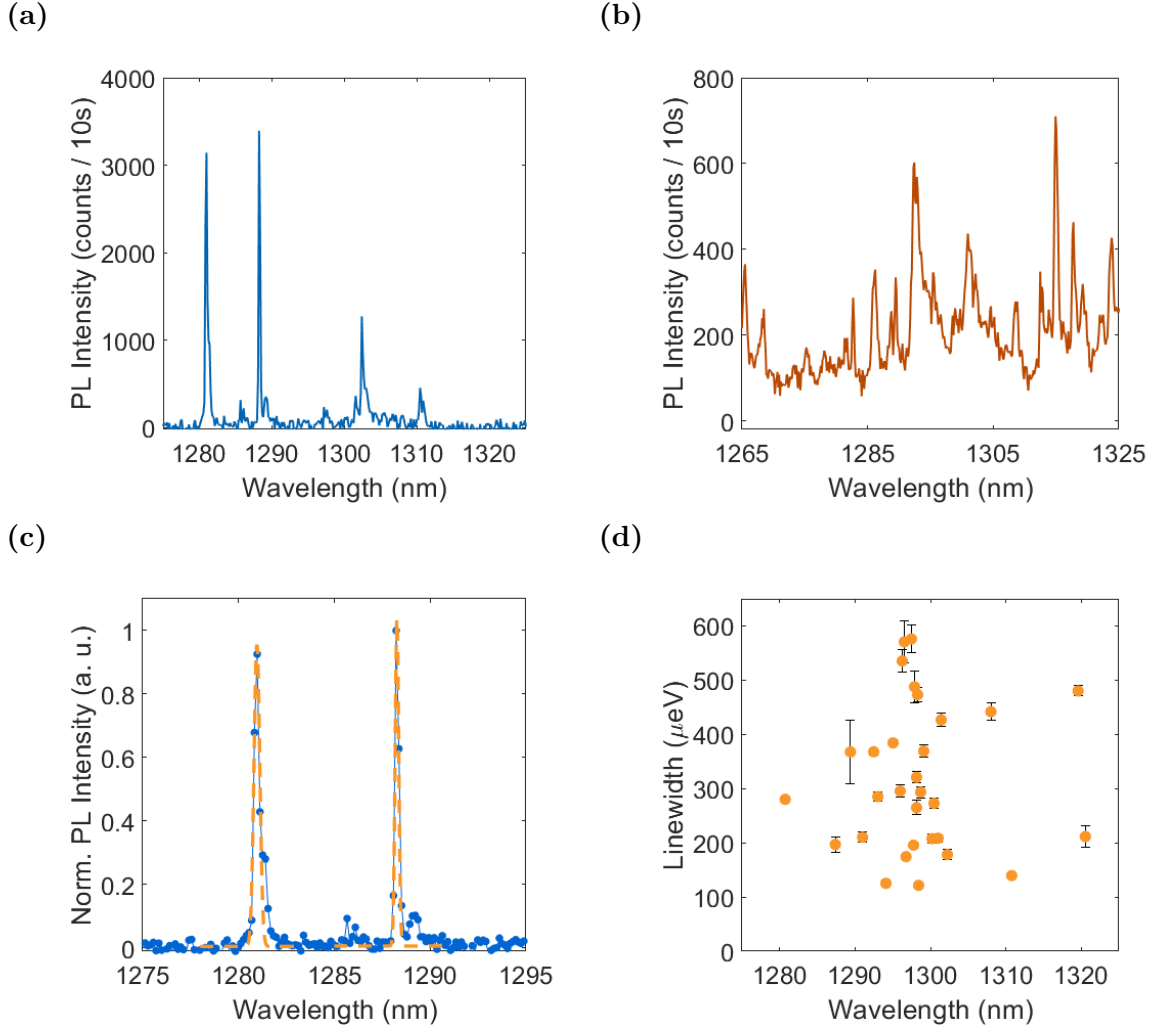


Figure 4.3: (a) Typical PL emission of an individual InAs QD within the optical cavity under CW laser excitation at 785 nm. (b) Example of PL emission measured in equivalent conditions on a different sample [105] with the same InAs/InAlAs QDs but no DBR mirrors. (c) Example of Gaussian fit of the two brightest transitions from the spectrum reported in panel (a). (d) Linewidth statistics obtained from the Gaussian fit of 30 spectral lines.

To quantify the FSS, we employed the well-established half-wave plate (HWP) method [112, 31] by sending the PL signal through a rotating HWP and a fixed linear polarizer (LP) mounted in the collection arm of the setup and measuring the resulting shift in energy at the spectrometer. An example of FSS measurement is

shown in Figure 4.4a, where the energy shift as a function of the wave-plate angle follows the expected sinusoidal behavior (dashed line). A statistical distribution was obtained by repeating the measurement on 35 lines of unidentified species in the telecom O-band: as reported in Figure 4.4b, approximately 50% of the QDs investigated show a FSS  $< 50 \mu\text{eV}$ , while larger values between  $70 \mu\text{eV}$  and  $300 \mu\text{eV}$  are recorded in the other cases.

The presence of emitters with large FSS may originate from unexpected anisotropy in some of the QDs examined. To gain more insight into this phenomenon, we carried out an additional investigation focusing on the orientation of the neutral excitons. First, we adjusted the position of the sample in the cryostat such that it was possible to identify the direction of the miscut steps with respect to the lab frame and to the optics mounted in the collection arm of the confocal microscope. Then we repeated the FSS measurements over different QDs and selected 35 neutrally charged excitons with splitting larger than 10% of the linewidth. For the majority of those emitters we found that the oscillations of the energy offset display the first maximum for a similar HWP rotation, suggesting that the dipoles are aligned along one preferential direction. The Gaussian fit in Figure 4.4d shows that the statistical distribution is centred around  $\Delta\phi = 3.1^\circ (\pm 2.2^\circ)$ , indicating that the component of the excitonic doublets higher in energy tends to be polarized along  $[11\bar{2}]$ . In fact, the small discrepancy of  $\approx 3^\circ$  can easily be attributed to limited accuracy while mounting the sample.

Interestingly, a small group QDs exhibits perpendicular polarization aligned with  $[1\bar{1}0]$ . As it was not possible for most emitters to clearly identify a XX-X pair and the FSS was extracted from one spectral line only, it may be possible that these values originate from a XX transition and consequently have the highest energy component oriented at  $90^\circ$  with respect to the exciton due to conservation of energy and spin. In summary, these results suggest that the presence of a  $2^\circ$  miscut introduces a privileged direction in the natural  $C_{3v}$  symmetry of the system.

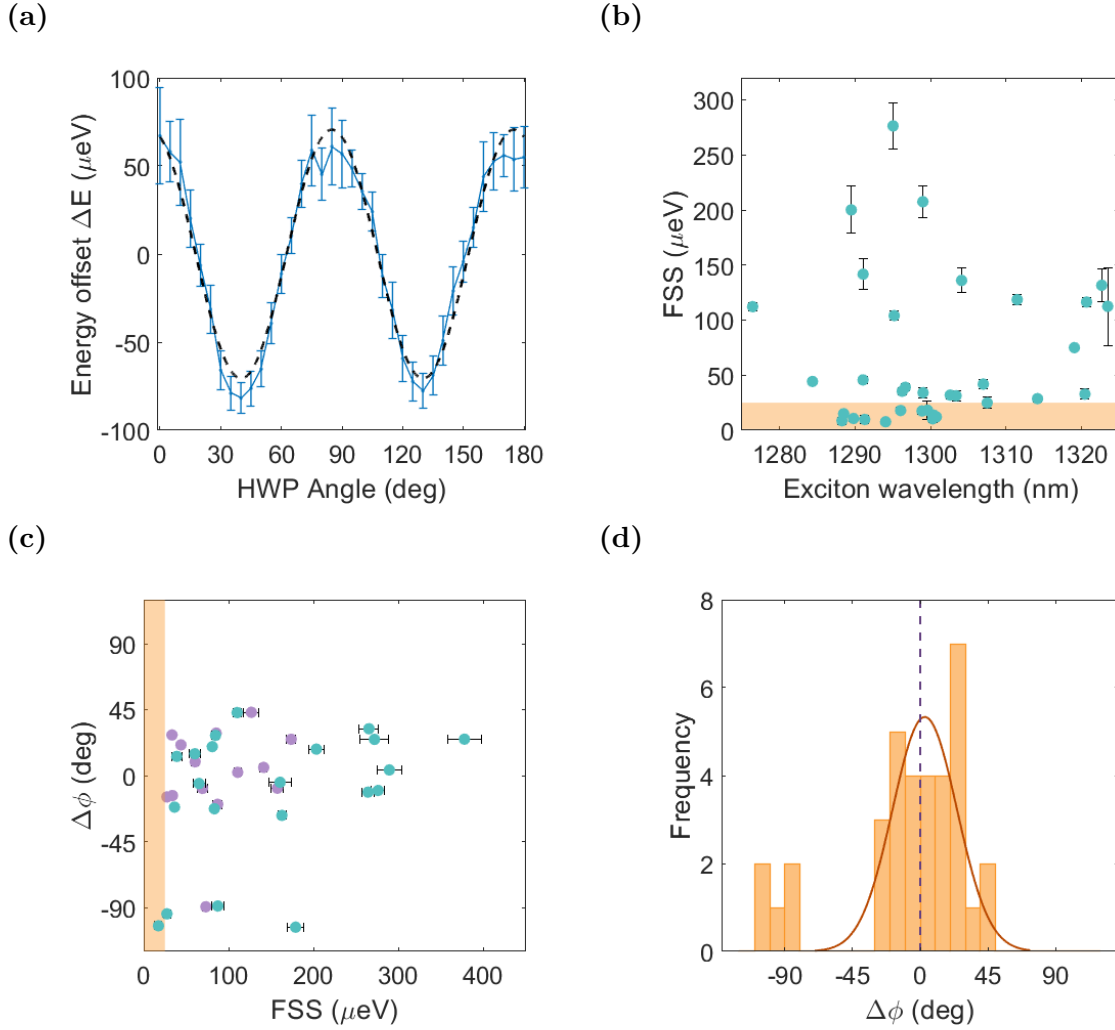


Figure 4.4: (a) Example of FSS measured on an InAs QD emitting in the telecom O-band using the HWP method. The dashed line is the sinusoidal fit of the energy offset. (b) Statistical distribution obtained by measuring the FSS of 35 spectral lines of unidentified species. The orange area indicates the estimated resolution limit for a transition with  $250 \mu\text{eV}$  linewidth. (c) Dipole orientation of the neutral excitations as a function of the FSS measured on 35 QDs.  $\Delta\phi$  is the angular offset with respect to the  $[\bar{1}\bar{1}2]$  direction while the orange area indicates the estimated resolution limit for a transition with  $250 \mu\text{eV}$  linewidth. The data points are plotted in violet when it was possible to identify clearly a XX-X pair and in blue when FSS and  $\Delta\phi$  were extracted from one line only. (d) Corresponding histogram with Gaussian fit of the statistical distribution. The vertical dashed line shows the direction of the miscut steps.

## 4.4 Numerical simulations

Following the experimental observations presented above, our collaborator Geoffrey Pirard from the University of Hamburg carried out numerical simulations to better understand the impact of the miscut on the optical properties of the QDs. This section contains a brief description of the model and the simulations to facilitate the interpretation of the experimental results.

### 4.4.1 Numerical model

Since the structure of the sample could not be reproduced because of computational limitations, we considered 3 simplified material systems. First we studied GaAs/AlAs(111) QDs, which is a simple case with no strain or alloy. Then we examined GaAs/Al<sub>0.15</sub>Ga<sub>0.85</sub>As(111) QDs to isolate the effects of alloying and finally InAs/GaAs(111) QDs, which is an idealised version of the sample and reveals the impact of strain.

The dots were modelled as hexagonally based truncated pyramids with a diameter of 70 nm, a height of 4 nm and a variable miscut angle ranging from 0° to 3° along  $[\bar{1}\bar{1}2]$ . They were placed at the centre of a cubic simulation box filled with the barrier material and the structure was allowed to relax in order to minimise the strain energy using a generalised valence force field (GVFF) model [113, 114]. The single-particle Schrödinger equation was then solved under the framework of the empirical pseudopotential method (EPM) [115] using a strained linear combination of bulk Bloch bands (SLCBB) [116] as a basis to expand the wave functions. Next, the many-body problem was addressed through a configuration interaction (CI) scheme [117], in which the correlated exciton wave functions are described as a linear combination of singly excited Slater determinants while the Hamiltonian is constructed from the electron-hole Coulomb and exchange integrals. The latter were calculated from the SLCBB wave functions and screened according to the Resta model [118].

### 4.4.2 Influence of the miscut on the optical properties of the QDs

Figure 4.5 shows the polarisation of the two decay paths from the exciton state, with polar diagrams of the squared optical transition dipole matrix element calculated for the 3 cases described above as a function of the miscut angle  $\alpha$ . For GaAs/AlAs(111) QDs characterized by the exact  $C_{3v}$  symmetry, the two decay paths from the exciton state are indistinguishable at  $\alpha = 0^\circ$  and therefore can be represented by circularly polarised emission with equal intensity in the linearly polarised measurements.

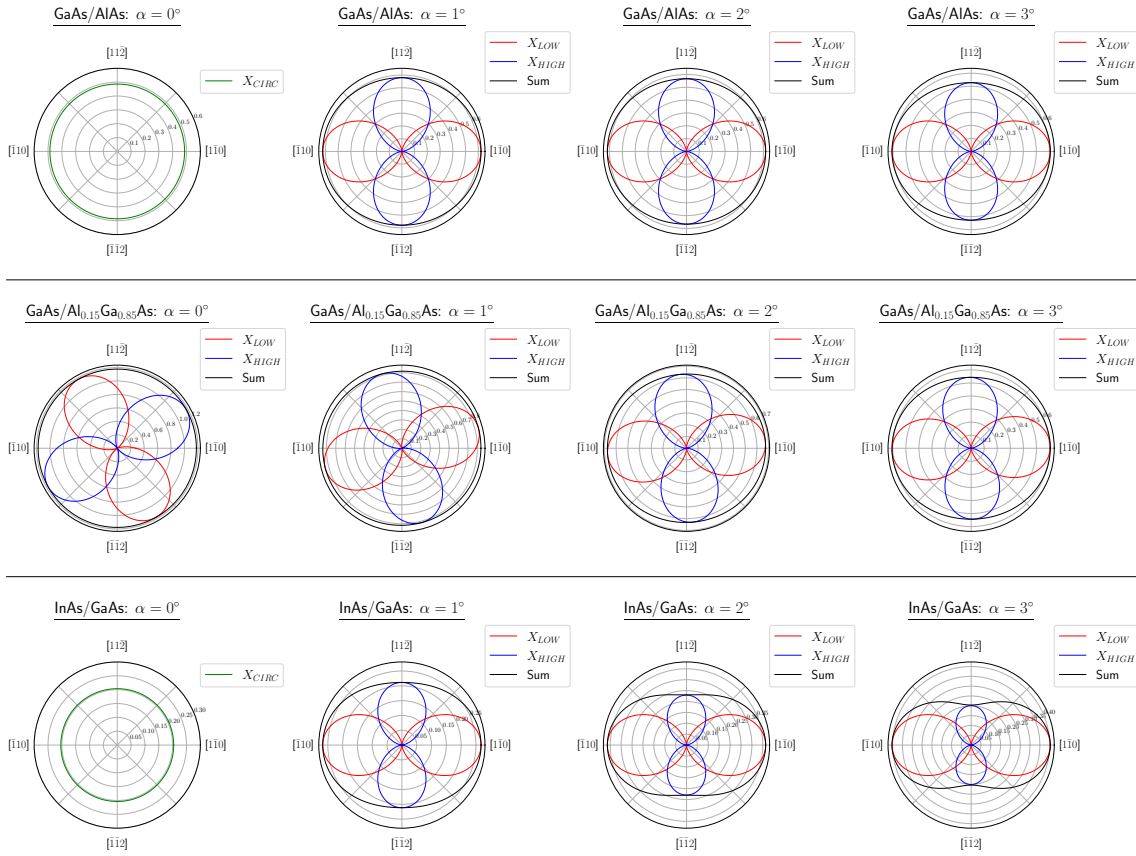


Figure 4.5: Polar diagrams showing the square of the optical transition dipole matrix element calculated for GaAs/AlAs (top panel), GaAs/Al<sub>0.15</sub>Ga<sub>0.85</sub>As (middle panel) and InAs/GaAs (bottom panel) QDs assuming different values of the miscut angle  $\alpha$ . ‘X<sub>LOW</sub>’ (‘X<sub>HIGH</sub>’) represents the lowest (highest) lying bright exciton state in energy. When two exciton bright states are degenerate, they are labelled ‘X<sub>CIRC</sub>’. The black line labeled ‘Sum’ represents the net total polarization from which the DLP is extracted.

When a miscut is introduced, the decay paths become distinguishable and the polarisation of the emitted photons reconfigures such that the lowest lying bright exciton state ( $X_{\text{LOW}}$ ) is polarised along the  $[1\bar{1}0]$  crystal axis whereas the polarisation of second bright exciton ( $X_{\text{HIGH}}$ ), higher in energy, is oriented perpendicularly along  $[11\bar{2}]$ . The net total polarisation aligns with  $[1\bar{1}0]$  and the degree of linear polarisation (DLP) increases slightly with the miscut.

If the AlAs barrier is replaced with  $\text{Al}_{0.15}\text{Ga}_{0.85}\text{As}$  the degeneracy of the exciton states for  $\alpha = 0^\circ$  is broken, presumably because of the inhomogeneous composition. Furthermore, the rotation of the polarisation as a function of the miscut becomes smoother such that perfect alignment with the crystallographic axes is only achieved for higher values of  $\alpha$ . Finally, InAs/GaAs(111) QDs shows the same behaviour already described for GaAs/AlAs(111), but with a steeper increase of the DLP.

These simulations explain the experimental results reported in Figure 4.4c and 4.4d, indicating that the miscut is directly responsible for an abrupt change in polarisation and the appearance of a clear preferential orientation in all the material systems considered. We observe that effects of alloying are weaker than the impact of the miscut, which dominates for  $\alpha > 1^\circ$  and is enhanced by the addition of built-in strain. From these findings, we also conclude that the 5 data points in Figure 4.4c with polarization oriented along  $[1\bar{1}0]$  are most likely biexciton transitions.

To clarify the physical origin of this behaviour, Figure 4.6 presents the calculated charge densities of the electrons ( $e_0$ ) and holes ( $h_0$ ) in the conduction and valence ground states for GaAs/AlAs(111) and InAs/GaAs(111) QDs. In strain-free QDs both the hole and electron wave functions have a circular s-like symmetry for  $\alpha = 0^\circ$ . The introduction of the miscut steps makes the side of the QD towards  $[11\bar{2}]$  thicker than the one towards  $[1\bar{1}2]$  (Figure 4.7). As a result, the wave functions localise at the thicker edge of the dot and their spatial distribution becomes strongly elongated in the  $[1\bar{1}0]$  direction. The same situation is observed in the alloyed case, except for the distortion in the otherwise circular wave function that it causes.

The picture becomes more complicated in InAs/GaAs(111) QDs: in fact, the electron wave functions can spread more than in the strain-free case and they are

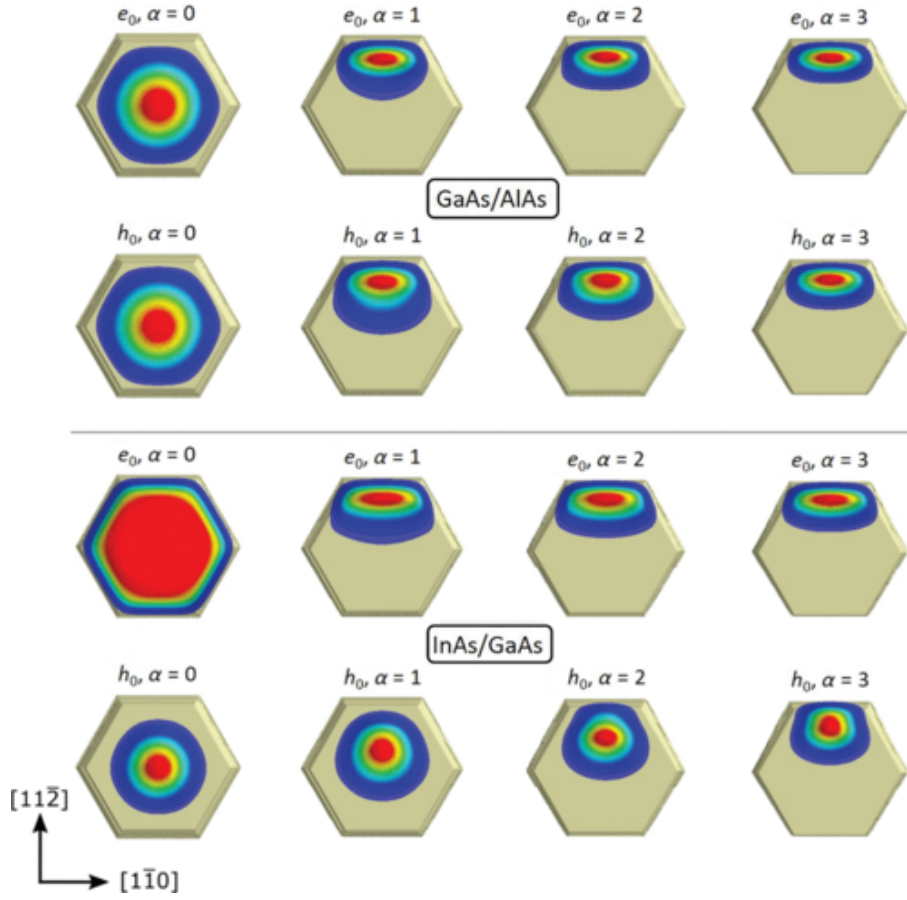


Figure 4.6: Spatial profile of the electron ( $e_0$ ) and hole ( $h_0$ ) wave functions calculated for GaAs/AlAs QDs (top panel) and InAs/GaAs QDs (bottom panel) with miscut angle  $\alpha$  ranging from  $0^\circ$  to  $3^\circ$ . The quantisation axis, i.e.  $[111]$ , is pointing towards the reader.

also found to be more elongated in the  $[1\bar{1}0]$  direction. At the same time, the holes are more confined so that their progression towards the edge of the QD as  $\alpha$  increases is slower and their charge densities are less elongated than in GaAs/AlAs(111) QDs. The elongation of the electron wave function increases with the miscut and is responsible for the growth of the intensity of polarisation along  $[1\bar{1}0]$  ( $I^{[1\bar{1}0]}$ ), in agreement with previous studies on elongated QDs [119]. Nevertheless, because of the different progression of the wave functions towards the edge of the dot, there may be a second motivation behind the optical anisotropy which derives directly from the definition of the dipole moment and is not only function of the elongation but also of the spatial separation between opposite carriers ( $d_{eh}$ ). In fact, such a

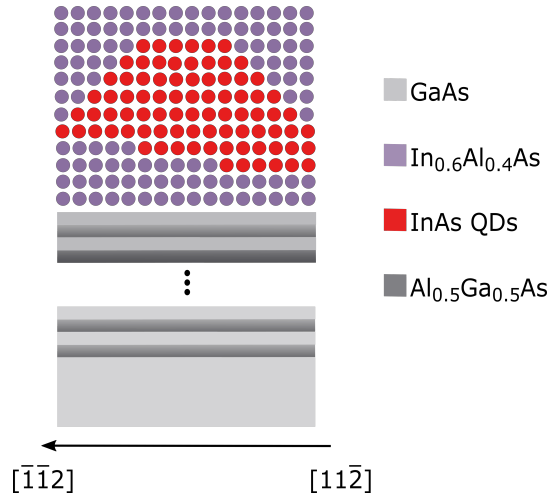


Figure 4.7: Schematic diagram showing a cross-section of an InAs QD deposited on a (111)-oriented surface with miscut towards  $[\bar{1}\bar{1}2]$ . The presence of miscut steps makes the side of the QD towards  $[11\bar{2}]$  thicker than the one towards  $[\bar{1}\bar{1}2]$

distance remains nearly constant and close to zero in the  $[1\bar{1}0]$  direction but keeps diminishing along  $[11\bar{2}]$  as  $\alpha$  increases, which ultimately provokes a lowering of the intensity of polarisation along  $[11\bar{2}]$  ( $I^{[11\bar{2}]}$ ).

The combination of the two phenomena discussed above lies behind the optical anisotropy in QDs grown on (111) vicinal substrates and the resulting preferential orientation for the polarisation of the neutral excitons observed in our measurements. It is now clear that in GaAs/AlGaAs QDs the anisotropy originates from the elongation of the electron and hole wave functions which are localised within the same effective volume of interaction. On the other hand, in InAs/GaAs QDs, the two effects discussed above come into play so that  $I^{[\bar{1}\bar{1}2]}$  is modulated by the magnitude of  $d_{eh}$ . As a result, when a  $2^\circ$  miscut is introduced the polarisation aligns with the direction of the steps in both cases, but with a different DLP.

## 4.5 Conclusions

Previous reports have demonstrated the growth on GaAs(111)A vicinal substrates of DE InAs/InAlAs QDs with low FSS that can be used to generate entangled photons at telecom wavelength. However, for their practical use in quantum communica-

tion applications it is desirable to improve the extraction efficiency of the emitted photons.

In this chapter we reported the formation of telecom-wavelength InAs/InAlAs droplet epitaxy QDs within an optical cavity on a vicinal GaAs(111)A substrate. First, we demonstrated that incorporating the QDs in an optical microcavity based on GaAs/AlGaAs distributed Bragg reflectors produces an enhancement of the brightness by a factor  $> 5$  in the telecom O-band, together with a remarkable reduction in the density of spectral lines and background. The optical characterization of the sample also revealed that the fraction of emitters with less than  $50 \mu\text{eV}$  splitting is approximately 50%. Because of the wide applicability of the DE growth scheme, those results can be easily transferred to different wavelengths or material systems. Further improvements in the extraction efficiency can be achieved by etching nanostructures such as mesas or micropillars. Also, linewidths and FSS can be reduced by changing the composition of the barrier layer from InAlAs to InGaAs [105, 120] and employing a smaller miscut angle, respectively.

Finally, our measurements showed that, despite the symmetry of the (111)-oriented substrate, the QDs tend to have dipoles aligned along a specific direction. In fact, numerical simulations based on the EPM and CI methods carried out by collaborators at the University of Hamburg have confirmed that presence the miscut modifies the spatial distribution of the electron and hole wave functions, leading to their elongation in the  $[1\bar{1}0]$  direction. This phenomenon influences the polarization of the excitonic states introducing a clear preferential orientation in the natural  $C_{3v}$  symmetry of the surface, while the addition of strain due to lattice mismatch modulates and enhances this effect.

# 5 | Bright Purcell-enhanced single-photon sources in the telecom O-band

This chapter presents the integration of InAs/GaAs QDs emitting in the telecom O-band with hybrid circular Bragg gratings (CBGs), which are a promising route to provide broadband optical enhancement of the radiation emitted by single and entangled photon sources. The first part of this chapter describes the design of CBGs operating in the telecom O-band and the fabrication of those devices on a GaAs slab with InAs QDs. The second part presents the characterization of the fabricated devices using photoluminescence spectroscopy and time-resolved measurements.

## 5.1 Introduction

As explained in Section 2.4.3, semiconductor quantum dots usually show low extraction efficiencies. In fact, half of the photons are emitted away from the surface and get absorbed in the substrate. Moreover, the high refractive index contrast at the semiconductor-air interface keeps most of the radiation trapped inside the sample. The first issue is usually addressed by creating a reflective backplane that “recycles” the light and redirects it towards the objective. In epitaxial structures a bottom mirror can be introduced by growing distributed Bragg reflectors (DBRs), i.e. a series of layers with thickness  $\lambda/4n_i$ , where  $n_i$  is the refractive index of the material  $i$ . As shown in Chapter 4, this concept can be exploited further by growing also a weaker top DBR and forming an optical microcavity with improved collection efficiency for certain frequencies [106, 121]. By increasing the number of layers in the top and bottom DBRs the effect of such a resonant cavity is usually intensified over

a narrower spectral range, however typical efficiencies for those structures saturate around 10% to 20% [122] and no relevant Purcell enhancement is predicted for planar microcavities [123].

Alternatively, better performances can be achieved with more elaborated devices: fabricating nanocavities like photonic crystals [28] and micropillars [124, 98] leads to high extraction efficiencies and strong Purcell enhancement, but their working principle is intrinsically narrowband. As a result, those devices require further efforts to achieve spectral overlap with the cavity mode and may not be suitable for the enhancement of entangled photon pairs. On the other hand, geometric approaches like microlenses [38] are generally easier to implement and provide efficiencies larger than 50% over a large bandwidth, but cannot guarantee any Purcell enhancement.

In this framework, hybrid circular Bragg gratings (also known as bullseye cavities) emerged as a promising alternative thanks to a novel flip-chip process for the integration of a broadband backside gold mirror, which eliminates the loss of photons into the substrate as well as the issue of a fragile free-standing membrane [125, 126]. The first experiments with those structures set new benchmarks for the entanglement fidelity, the photon indistinguishability and the single photon and entangled photon pair collection efficiency [76, 77], but they focused on the short wavelength range (780 nm - 880 nm). Despite the progress in the O-band achieved in more recent works [127, 128], comparable results at telecom wavelength have not been achieved yet. Moreover, all those reports demonstrated the operation of a single optimized device, while the reproducibility of their performances remains an open question.

In this chapter we present the design and characterization of efficient quantum light sources in the telecom O-band based on InAs QDs into hybrid circular Bragg gratings. First, we investigate and optimize the performances of those devices using 3D FEM simulations in the frequency domain. Then, we characterize the fabricated CBGs demonstrating efficient and Purcell-enhanced single-photon emission. Finally, we address the question of reproducibility by benchmarking the performances of multiple devices.

## 5.2 Device design

A hybrid circular Bragg grating consists of a set of concentric trenches etched with periodicity  $a$  in a semiconductor slab around a central disk, with QDs grown at half the slab thickness (Figure 5.1). The refractive index contrast at the trenches causes strong in-plane reflections, leading to a cavity resonance localized in the central disk. Meanwhile, part of the in-plane emission is directed vertically by the concentric rings which meet the second-order Bragg condition.

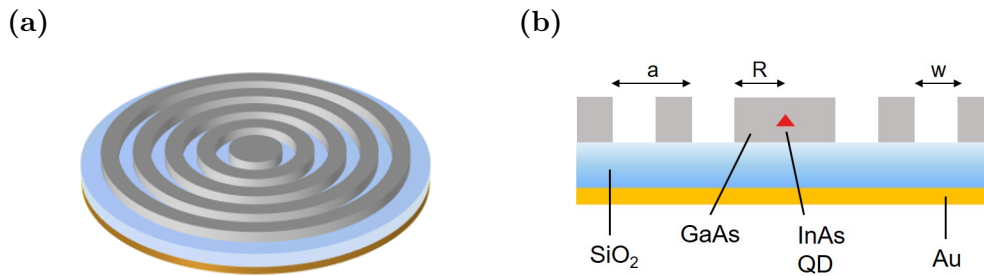


Figure 5.1: (a) Schematic representation of a hybrid CBG on GaAs. (b) Schematic cross-section of the device showing the different layers and the most important design parameters, i.e. the lattice constant  $a$ , the width of the trenches  $w$  and the radius of the central disk  $R$ .

Since half of the emitted photons would be dispersed in the substrate, the device includes a backside broadband gold mirror separated from the slab by an insulating layer of SiO<sub>2</sub>. This layer not only prevents the diffusion of gold within the device, but also acts as a barrier for any plasmonic effect that could form at the semiconductor-metal interface. If the thickness of SiO<sub>2</sub> is properly designed, almost all the photons leaking into the substrate can be effectively reflected from the gold mirror and redirected upwards, where the bright emission can be collected with high efficiency by the objective lens.

### 5.2.1 Numerical simulations

In order to fabricate CBGs operating at telecom wavelength we first studied and optimized the performances of those devices using the COMSOL simulation suite:

in particular, we ran 3D FEM simulations in the frequency domain using the Wave Optics module. More details about FEM simulations are given in Section 3.2.

In our simulations, the CBG is excited with an electric dipole source oriented along the  $y$  axis and placed in the centre of the GaAs disk ( $x=0, y=0$ ) at half of the slab thickness, reproducing the photon emission from an individual quantum dot. Moreover, the model is surrounded by perfectly matched layers (PMLs), i.e. artificial strongly absorbing layers that avoid undesired reflections of the emitted radiation. The Purcell factor  $F_p$  is obtained as the ratio between the power emitted by the dipole source embedded in the CBG and the power emitted by the same dipole in semi-infinite GaAs. The ability of the device to direct photons towards the collection optics is estimated using the following quantities [129, 127]:

1. The extraction efficiency is the percentage of emitted radiation that can escape into the air domain above the device.
2. The far-field efficiency in a certain numerical aperture (NA) is the far-field intensity integrated on such NA divided by the far-field intensity in the upper air hemisphere.
3. the dipole collection efficiency (DCE) in a certain NA is the product of the extraction efficiency and the corresponding far-field efficiency.

We based the initial choice of parameters on the results of a recent design study published by *Rickert et al.* [127], which demonstrated that a single device can support a broad cavity mode ( $\lambda = 1319$  nm,  $F_p = 15$ , FWHM = 11.9 nm) and display high extraction efficiency in the whole telecom O-band. This broadband version of the CBG structure should also guarantee an improved robustness against common fabrication imperfections and spatial displacement of the emitter. Since the GaAs wafer used in this work showed a high-density QD emission centred around 1290 nm, we investigated the influence of the lattice constant  $a$  and the radius  $R$  of the central disk on the resonance wavelength of the CBGs in order to re-optimize the device design. In fact, the resonance condition for an optical cavity consisting of

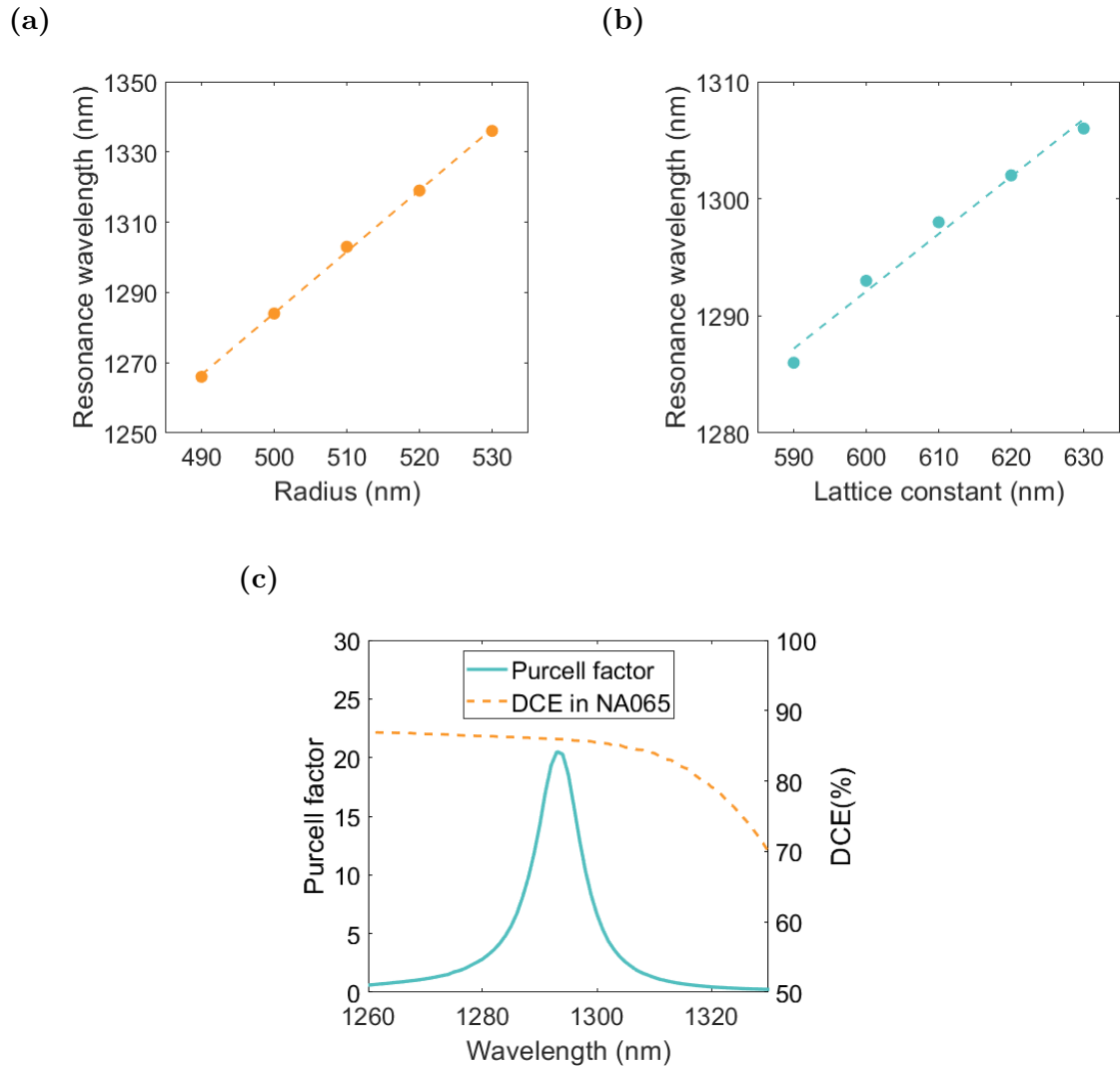


Figure 5.2: (a) Resonance wavelength as a function of the radius  $R$  for a GaAs CBG ( $t_{\text{GaAs}} = 240$  nm,  $t_{\text{SiO}_2} = 300$  nm) with 4 rings  $w = 300$  nm and  $a = 620$  nm. The dashed line represents the linear fit of the data points. (b) Resonance wavelength as a function of the lattice constant  $a$  for a GaAs CBG ( $t_{\text{GaAs}} = 240$  nm,  $t_{\text{SiO}_2} = 300$  nm) with 4 rings,  $w = 300$  nm and  $R = 510$  nm. The dashed line represents the linear fit of the data points. (c) Simulated performance of the optimized CBG ( $t_{\text{GaAs}} = 240$  nm,  $t_{\text{SiO}_2} = 300$  nm,  $R = 510$  nm,  $a = 600$  nm,  $w = 300$  nm) with Purcell factor (solid line) and DCE in NA = 0.65 (dashed line) as a function of wavelength.

the central disk and diffractive grating can be written as [129]:

$$(n_{\text{slab}} \cdot 2R) + (n_{\text{grating}} \cdot l_{\text{eff}}) = m \cdot \lambda \quad (5.1)$$

where  $n_{\text{slab}}$  and  $n_{\text{grating}}$  are the effective refractive indexes experienced by the guided TE mode in the central disk and in the grating respectively,  $l_{\text{eff}}$  is the effective mirror length (i.e. the penetration depth of the mode into the grating) and  $m$  the mode index.

As shown in Figure 5.2, the resonance wavelength shifts linearly with  $R$  and  $a$ : a  $\sim 17$  nm red-shift of the cavity mode is observed when increasing  $R$  by 10 nm, with negligible effect on the Purcell factor. On the other hand, the red-shift caused by the lattice constant is less pronounced, approximately 5 nm when  $a$  is increased by 10 nm, but it has a stronger effect on  $F_p$  because this parameter is directly related to the reflectivity of the grating and therefore to the confinement capability and  $Q$  factor of the cavity. The final set of design parameters produced by our optimization is:  $t_{\text{GaAs}} = 240$  nm,  $t_{\text{SiO}_2} = 300$  nm,  $R = 510$  nm,  $a = 600$  nm,  $w = 300$  nm. The optical performances of the optimized device are summarized in Figure 5.2c, which shows a collection efficiency in  $\text{NA} = 0.65$  above 80% for a 50 nm wavelength range, in addition to a cavity mode around 1294 nm, with Purcell factor  $F_p \sim 20$  and  $\text{FWHM} = 10.2$  nm.

### 5.2.2 Final mask

From the results of the calculations presented in the previous section, we created an electron-beam mask for test chips where the CBGs are arranged in matrices with eleven rows and thirteen columns (Figure 5.3). The parameters that are varied within a matrix are the lattice constant and the radius of the central disk, while the width of the trenches changes when moving from a matrix to another. This variation of multiple parameters is necessary to cover the QD emission range as well as to maximize the chances of having efficient devices: in fact the bonding process might have slightly altered the structure of the sample and there also needs to be some room to compensate for fabrication imperfections. In order to speed up the

characterization we etched ten concentric rings for each device: according to the simulations, the outer rings do not improve the optical properties of the CBGs but make it easier to find them under the microscope.

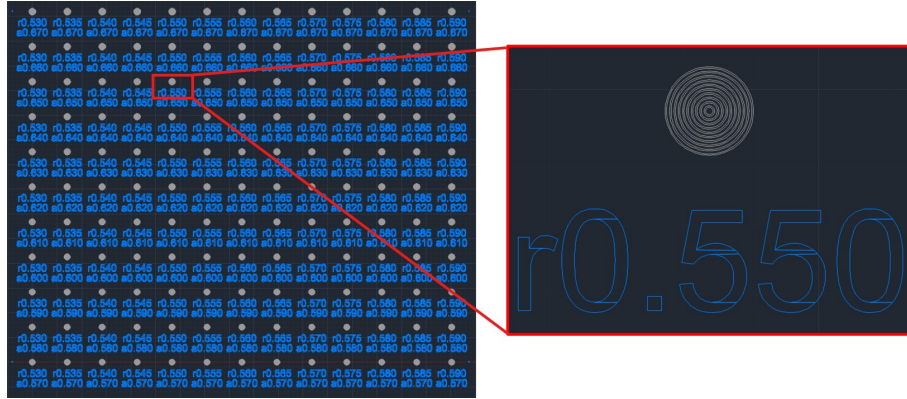


Figure 5.3: Exemplary matrix from the electron-beam mask where the lattice constant and the radius of the central disk are varied between different devices. The detail on the right-hand side shows a close-up of one device with part of its label.

In total, we fabricated seven test samples on wafer W1562 following the methods described in section 3.3. Once the lithography was optimized, we restricted the set of parameters in the mask and tried to target the area of the wafer with the lowest dot density.

## 5.3 Experimental results

All the fabricated CBGs were characterized using the PL setup described in Section 3.4.1. Unless stated otherwise, the measurements presented below were taken at a cryogenic temperature of approximately 5K.

### 5.3.1 Reflectivity measurements

The first step of the characterization process focuses on the optical response of the CBGs disregarding the presence of QDs. In particular, we investigated the presence of cavity modes localized in the central disk using reflectivity measurements: we illuminated the devices with uncollimated light emitted by an O-band broadband LED

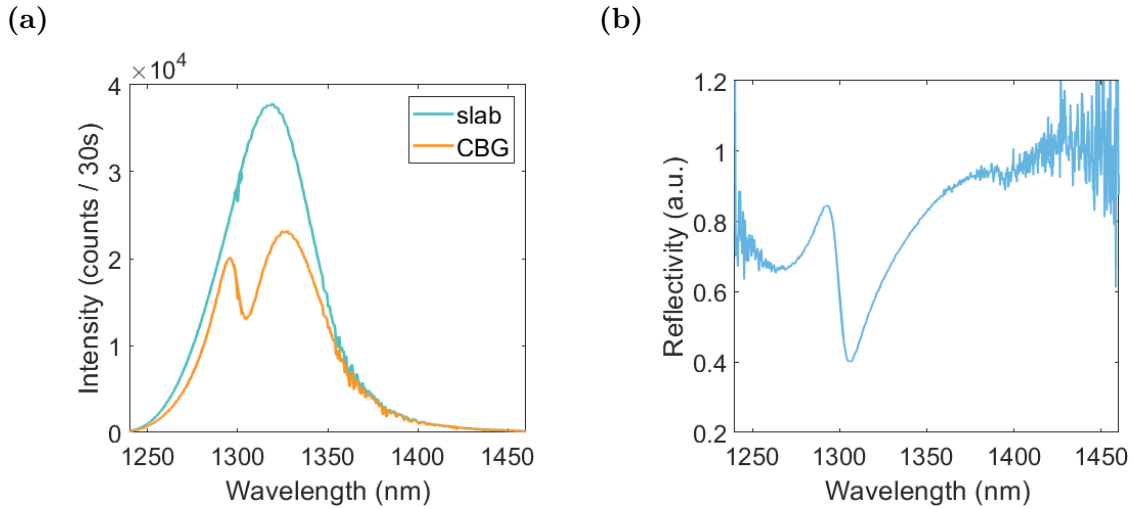


Figure 5.4: (a) Reflectivity signal collected on a CBG (orange) and on an unpatterned region of the sample (teal) illuminated with a broadband LED emitting around 1310 nm. (b) Reflectivity spectrum obtained normalizing the signal collected on the device by the one collected on an unpatterned region of the sample. The presence of a cavity mode is indicated by the dip around 1305 nm.

source ( $\sim 70$  nm FWHM) and recorded the reflected signal with the spectrometer. To compensate for the effects of wavelength dependence in various components of the setup (i.e. the LED emission, the optics and the efficiency of the detector) as well as in the layer stack of the wafer and focus only on the modes confined in the centre of the devices, the signal collected from a CBG was normalized by the signal collected on an unpatterned region of the sample (Figure 5.4). In these measurements the presence of a mode usually appears as a dip in the spectrum, indicating that some of the LED light has been coupled into the cavity [130]. As explained above, such a dip is expected to shift towards longer wavelength for devices with bigger lattice constant or radius of the central disk.

An example of this behaviour is reported in Figure 5.5, where we show the cavity modes (i.e. reflectivity<sup>-1</sup>) measured on CBGs with the same design parameters but increasing values of  $R$  or  $a$ . Despite some small differences in the resonance wavelength, the experimental results show that the fabricated devices operate in the desired spectral range around 1300 nm. We also observe the expected redshift of

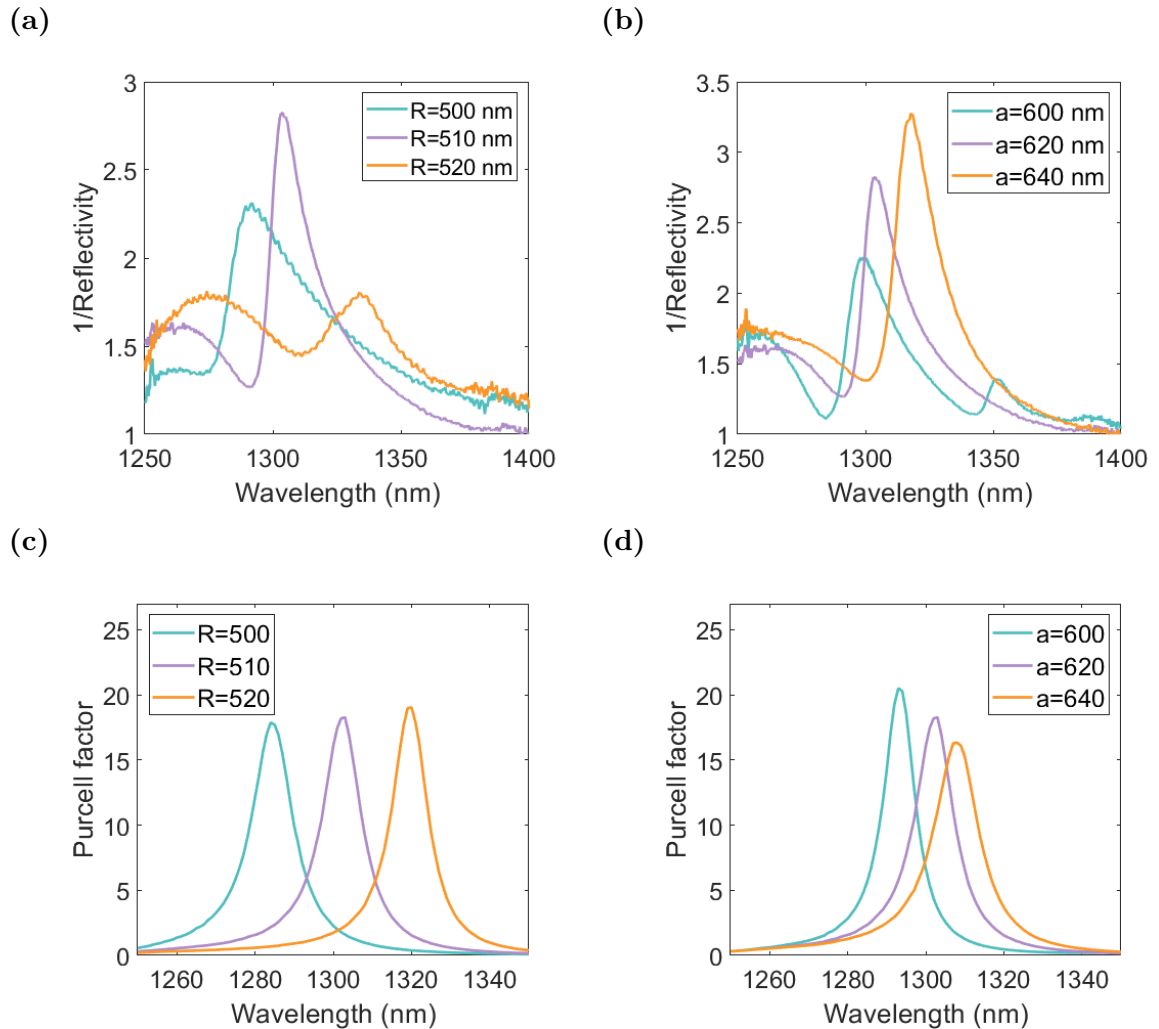


Figure 5.5: (a) Cavity modes measured on 3 CBGs with the same lattice constant  $a = 620$  nm but different radius of the central disk ( $R = 500$  nm, 510 nm and 520 nm). (b) Cavity modes measured on 3 CBGs with the same radius  $R = 510$  nm but different lattice constant ( $a = 600$  nm, 620 nm and 640 nm). (c) Simulated cavity modes for 3 CBGs having the same design parameters of the ones measured in panel (a). (d) Simulated cavity modes for 3 CBGs having the same design parameters of the ones measured in panel (b).

the resonance when increasing the radius of the central disk (Figure 5.5a and 5.5c) or the lattice constant (Figure 5.5b and 5.5d), with a more pronounced effect of  $R$  as predicted by our calculations. This ability to adjust the resonance wavelength is important for future optimizations, where a QD with optimal quantum properties can be pre-selected and a CBG can be fabricated around it using in-situ electron beam lithography. Finally, we notice that the modes are broader than expected from the simulations and there are considerable differences in the bandwidth when moving from a device to another, with FWHM varying from  $\sim 18$  nm to  $\sim 29$  nm. It is not unreasonable to attribute all those discrepancies to the presence of imperfections in the fine features.

### 5.3.2 Micro-PL measurements

As discussed in Section 3.4.1, we employed micro-PL spectroscopy to characterize the emission spectrum of the QDs under above-band laser excitation. In Figure 5.6a we report an exemplary PL spectrum from an unetched region of the sample, which confirms the presence of QDs in the slab after wafer bonding and substrate removal. In particular, the spectrum is characterized by emission lines in the telecom O-band sitting on a broader background, which is centred around 1290 nm and indicates a high-density QD distribution. It is worth noting that the density seems to decrease on the tail of the distribution, where it is possible to observe isolated QD lines with low background around 1330 nm and above (Figure 5.6b).

Figure 5.7a shows a typical micro-PL signal from a CBG ( $a = 610$  nm,  $R = 520$  nm) under above-band laser excitation. The spectrum indicates a clear enhancement of the PL intensity by approximately two orders of magnitude compared to the bare slab. Such an enhancement originates from both the efficient out-of-plane coupling and the presence of a cavity mode. Moreover, we observe a reduced density of spectral lines, which makes it possible to isolate the emission pattern from single QDs in the spectral region above 1330 nm. Unless stated otherwise, the measurements described below and in the following subsections will refer to the QD reported in Figure 5.7b.

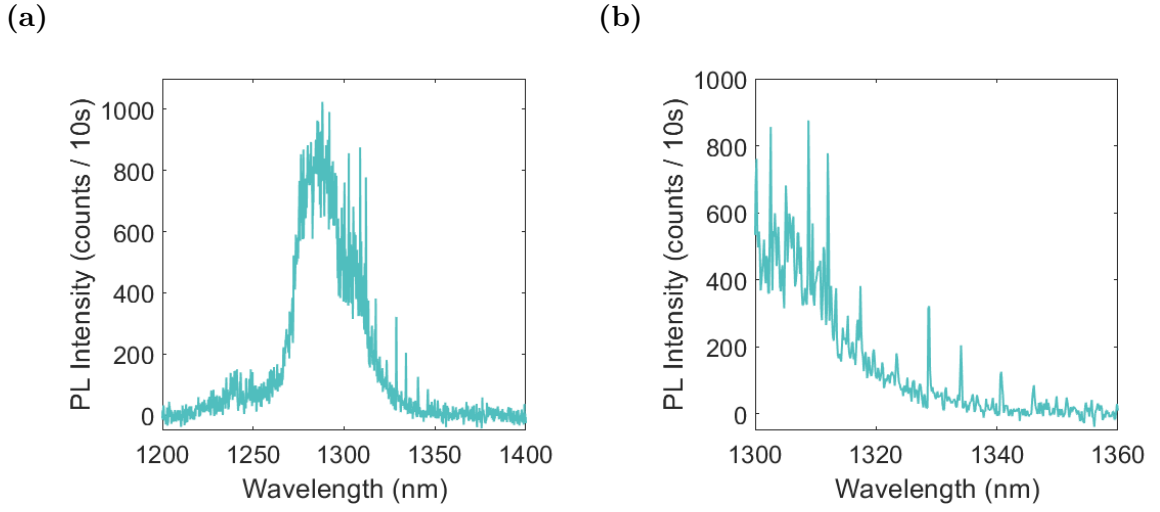


Figure 5.6: (a) Micro-PL signal from an unetched area of the sample under  $3 \mu\text{W}$  above-band CW laser excitation, showing the presence of QDs in the GaAs slab after wafer bonding and substrate removal. (b) Detail of the isolated emission lines on the tail of the distribution.

Since the PL spectrum of such a dot is characterized by the presence of individual lines from various charge configurations, we performed polarization resolved measurements (Figure 5.7c) as described in Section 3.4.1, which allowed us to clearly determine the neutral X and XX states. As shown in Figure 5.7d, the energy shift as a function of the quarter wave-plate angle follows the expected behaviour [31], indicating a fine structure splitting of  $93.8(\pm 1) \mu\text{eV}$ .

In Figure 5.8 we study the power dependence of the PL response. For single QDs the maximum number of emitted photons is limited by the lifetime of the excited state and therefore a saturation of the PL intensity is expected [131]. The integrated PL intensity ( $I$ ) with respect to the optical excitation power ( $P$ ) is usually described by the equation:

$$I = I_{\text{sat}} \frac{P}{P + P_0} \quad (5.2)$$

where  $I_{\text{sat}}$  is the integrated PL intensity at saturation and  $P_0$  is the normalized power value, i.e. the excitation power such that  $I(P_0) = \frac{1}{2}I_{\text{sat}}$ .

From Figure 5.8a, we observe that the background contribution increases significantly at high laser power. This effect is consistent with previous observations [128]

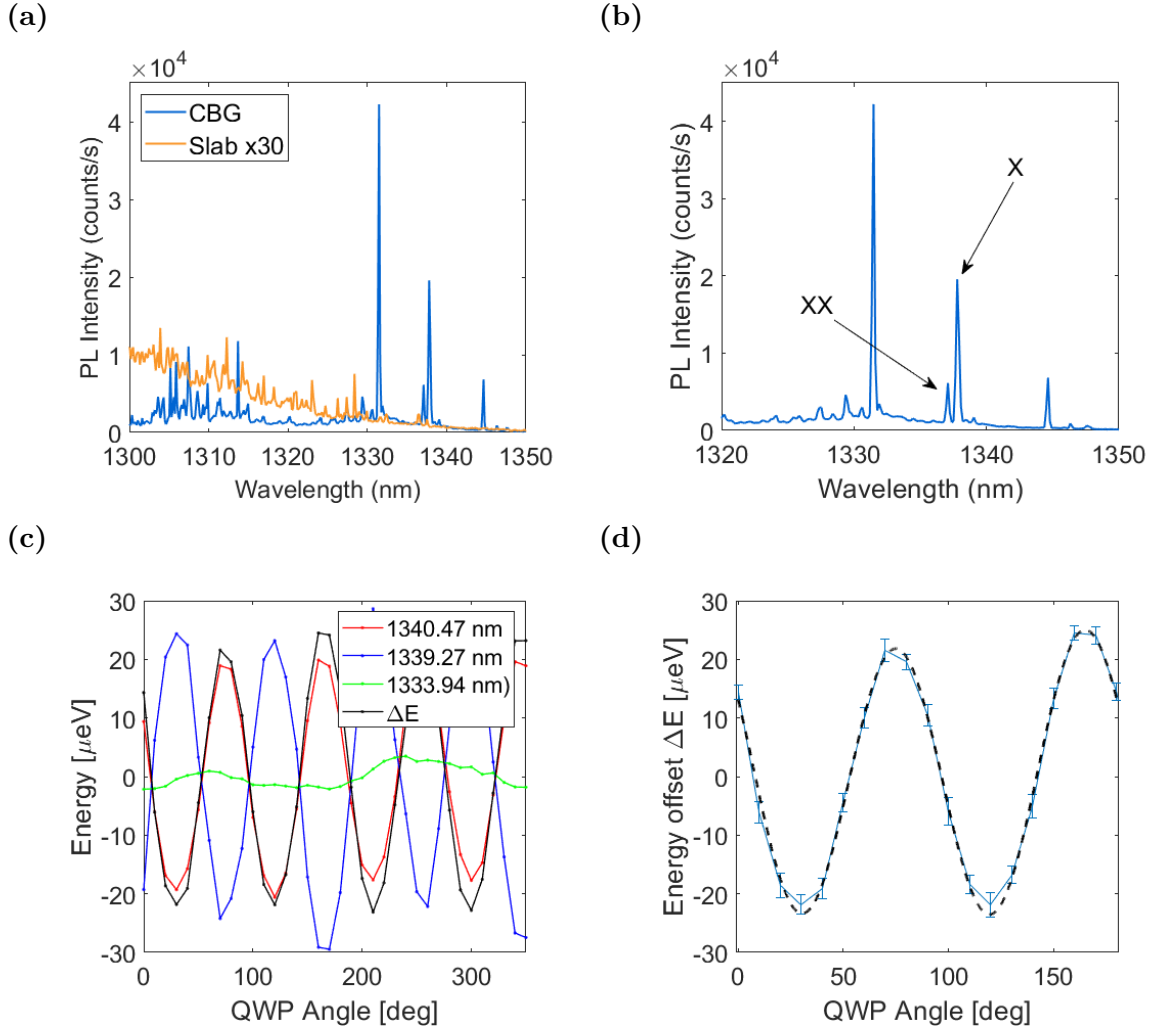


Figure 5.7: (a) Comparison between the micro-PL signal from a CBG (blue line) and from an unetched area of the sample (orange line) under above-band CW laser excitation. The signal measured on the slab is multiplied by a factor of 30. (b) PL emission spectrum of a single QD integrated into a CBG under above-band CW laser excitation. (c) Example of fine structure splitting measurement using the QWP method. The energy offset  $\Delta E$  (black line) is obtained as the half-difference of X (red line) and XX (blue line). (d) Fit of the energy offset from (c) according to [31], indicating a fine structure splitting of  $93.8(\pm 1) \mu\text{eV}$ .

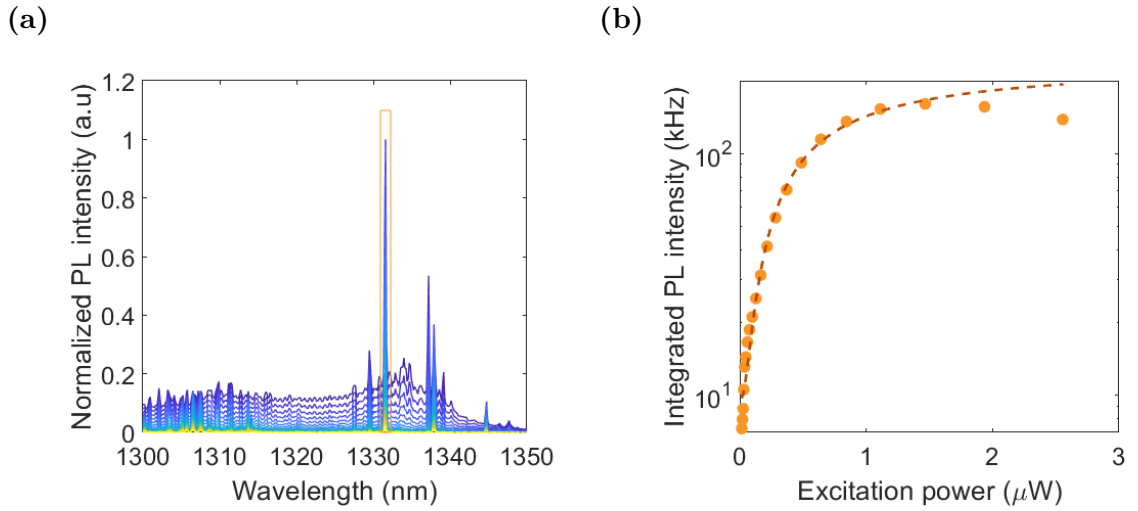


Figure 5.8: (a) Power dependent PL spectra under above-band CW laser excitation. (b) Background corrected saturation curve for the brightest emission line at 1331 nm highlighted in orange.

and can be partly attributed to background emission from QDs located in the outer rings, which becomes more relevant for high excitation power and is guided towards the collection optics by the diffraction grating. Nevertheless, after subtracting the background, the power dependent data fit well with Equation 5.2 as shown in Figure 5.8b for the brightest emission line at 1331 nm highlighted in orange.

It is also worth noting that saturation is reached for a pump power  $P_{\text{sat}}$  of approximately  $1 \mu\text{W}$ , much lower than the one required to observe clear PL emission from the slab. This is due to the presence of the diffraction grating, which may help focusing the incoming laser radiation towards the central disk for a more efficient excitation of the dot.

### 5.3.3 Emission dynamics

To probe the overlap between the transitions of the QD and the cavity mode and quantify the Purcell enhancement provided by the CBG, we studied the temporal evolution of the carrier populations using time-resolved spectroscopy as described in Section 3.4.2. In Figure 5.9a we report the time-resolved luminescence trace for

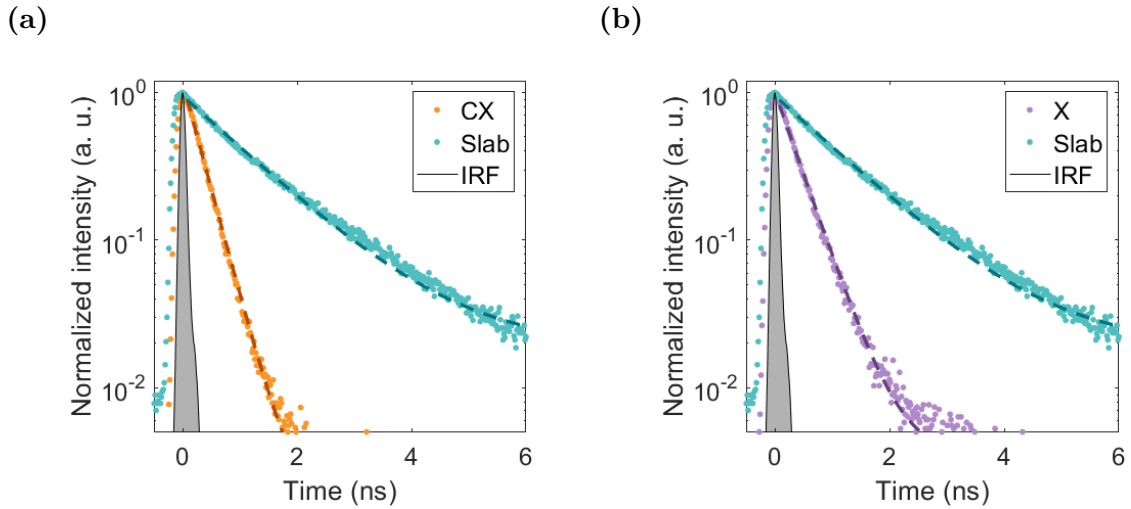


Figure 5.9: (a) Photoluminescence decay traces of the brightest CX emission line from the CBG at  $\lambda=1331$  nm and of an exemplary reference line from the unetched slab measured under above-band pulsed excitation at 40 MHz. The dashed lines represent the exponential fit of the decay traces, yielding a lifetime of 289 ps for the CX transition and 1.57 ns for the exemplary reference line in the slab. (b) Photoluminescence decay traces of the X line from the CBG and an exemplary reference line from the unetched slab. The dashed lines represent the exponential fit of the decay traces, with a lifetime of 358 ps for the X transition.

the brightest transition at 1331 nm, which appears to decay much faster than an exemplary spectral line measured outside the device. In fact, a single exponential fit yields a time constant of 289 ps and 1.571 ns, respectively.

In order to create a baseline for a more meaningful comparison, we repeated the same time-resolved measurement on 17 further transitions from 5 different locations on the slab, obtaining a set of 18 data points with average lifetime of  $\tau_{\text{slab}} = 1.584$  ns and standard deviation  $\sigma_{\text{slab}} = 254$  ps. As a result, we estimate a Purcell factor of  $\sim 5.5$  for the brightest transition at 1331 nm. Also, a similar lifetime of 358 ps is observed for the X transition at 1337 nm (Figure 5.9b), demonstrating that the device can enhance the radiative decay rate by a factor  $> 4$  over a wavelength range of 7 nm. We attribute the deviation from the simulated maximum Purcell factor of  $\sim 15$  to the presence of imperfections in the fine features and to a possible

displacement of the emitter from the centre of the device due to the nondeterministic fabrication process. In future works the performances of the CBG may be improved using deterministic fabrication techniques such as in-situ electron beam lithography, which offers high lateral accuracy  $< 30$  nm [126, 132].

In summary, the results presented so far showed Purcell enhanced emission of a single InAs QD coupled to a circular Bragg grating operating in the telecom O-band. However, the main motivation behind the work presented in this chapter was the demonstration of an efficient quantum light source and therefore a study of the photon statistics is presented in the following section.

### 5.3.4 Photon statistics

The non-classical nature of the QD emission is particularly important for the use of the CBG as a source of single photons in the telecom O-band. Therefore, we concluded the characterization of the device by studying the photon statistics of the brightest transition at  $\lambda=1331$  nm using a fiber-based Hanbury, Brown and Twiss (HBT) interferometer, as described in Section 3.4.3. To probe the maximum emission rate of the source, second-order correlation measurements were carried out under CW laser excitation. In this pumping regime new charge carriers are captured by the QD immediately after a radiative recombination, such that main limit to the single photon emission rate is given by the radiative lifetime of the transition examined. In Figure 5.10a we report the normalized histogram of coincidences measured under 250 nW above-band CW laser excitation at 785 nm. At a time delay  $\tau = 0$  ns we observe a pronounced sign of anti-bunching, with strongly suppressed coincidences indicating single photon emission. By fitting such a dip, a value of  $g^{(2)}(0) = 0.13$  can be extracted. The coincidences recorded at zero delay represent occasional multi-photon events, that we attribute to background emission.

Given the increasing background contribution observed in Figure 5.8a, we repeated the characterization of the photon statistics for different excitation powers. Figure 5.10b summarizes the results of this study, showing the extracted values of  $g^{(2)}(0)$  as a function of the total single photon rate recorded on a pair of SNSPDs with  $\sim$

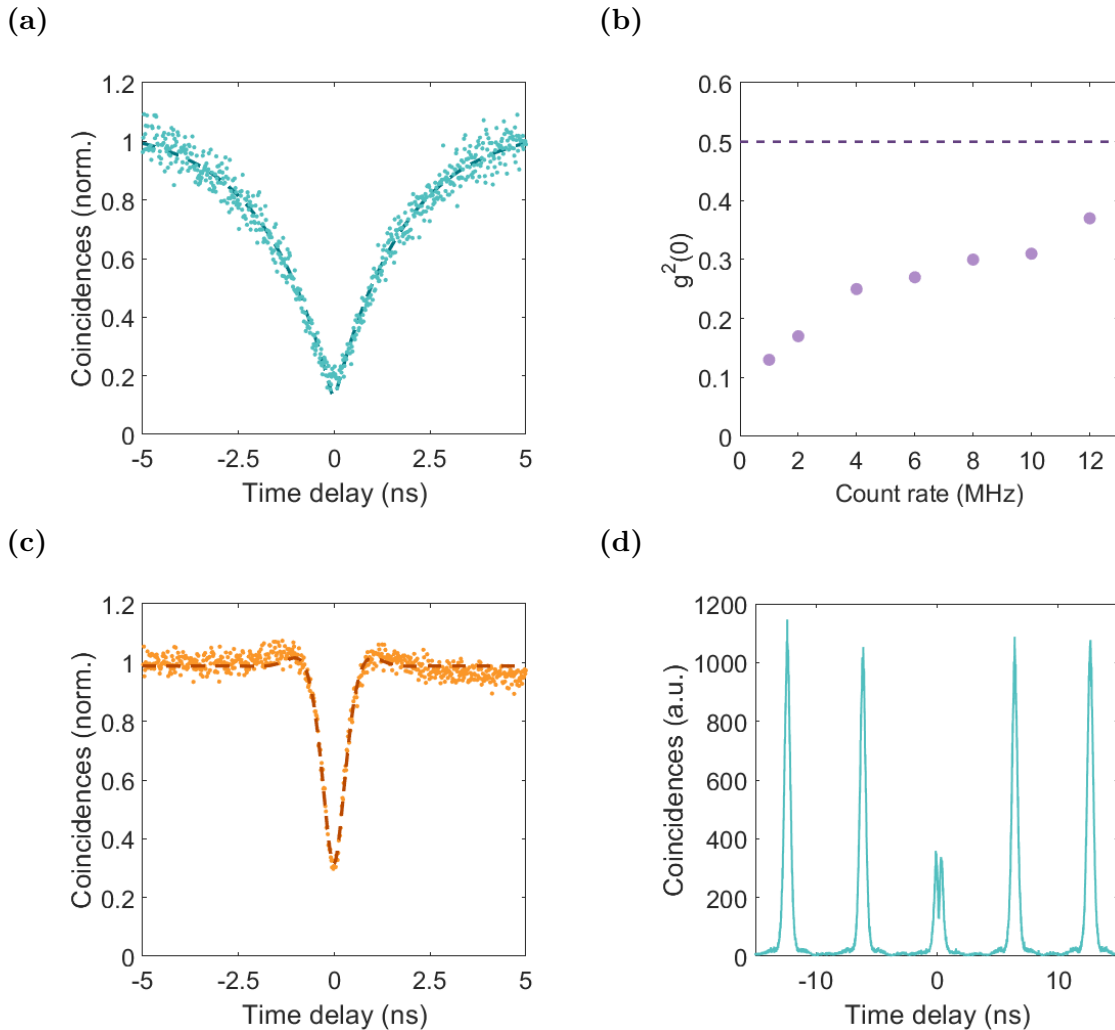


Figure 5.10: (a) Example of second order photon correlation measured on the brightest transition at  $\lambda = 1331$  nm under 250 nW above-band CW laser excitation. The dashed line represents the fit of the experimental data and the reduced coincidences at zero delay time with  $g^{(2)}(0) = 0.13$  indicate single photon emission. (b) Extracted values of  $g^{(2)}(0)$  as a function of the single photon rate measured using increasing excitation power and SNSPDs with  $\sim 60\%$  efficiency at 1310 nm. The dashed line represents the limit for the condition  $g^{(2)}(0) < 0.5$ . (c) Second order photon correlation measured under 850 nW above-band CW laser excitation, corresponding to a single-photon rate of 10 MHz. (d) Coincidence histogram acquired under above-band pulsed laser excitation at 80 MHz.

60% efficiency at 1310 nm. We observe that the occurrence of multi-photon events increases for higher pump power, due the saturation of the transition examined and increasing background emission. However, the condition  $g^{(2)}(0) < 0.5$  is fulfilled for count rates  $> 10$  MHz (Figure 5.10c), placing this device among the brightest QD-based single photon sources at telecom wavelength reported in literature at the time of writing [133, 134, 135, 136, 128, 137, 138]. For future improvements, resonant excitation schemes have been shown to maximize the non-classicality of the emitted light and lead to essentially background-free single photon emission [139, 140]

Since applications in quantum communication and quantum information processing require the generation of single photons on-demand , we also characterized the photon statistics when the sample is excited with an 80 MHz pulsed diode laser emitting at a wavelength of 780 nm. As shown in Figure 5.10d, the corresponding histogram exhibits obvious accumulations of coincidences at time delays multiple of 12.5 ns. The maximum single photon count rate recorded on the detectors under those conditions is 2 MHz, equivalent to 2.5% system efficiency, while a value of  $g^{(2)}(0) = 0.28$  can be inferred by normalizing the area of the central peak to the one of the neighbouring peaks.

Finally, to underline that the improved brightness provided by the CBG can be advantageous for real-world applications, we repeated the second-order correlation measurements after adding a variable length of standard SM telecom fiber between the photon source and the detectors. In Figure 5.11a we report the count rate recorded on the SNSPDs and the corresponding value of  $g^{(2)}(0)$  as a function of the fiber length when the device is pumped with a CW laser power of  $\sim 0.75P_{\text{sat}}$ . While the signal intensity drops exponentially with distance because of the attenuation  $\alpha = 0.31$  dB/km, the value of  $g^{(2)}(0)$  remains almost constant around 0.25 for a fiber length up to 50 km, demonstrating that the non-classical nature of the CBG emission is preserved over long distances. When moving to 75 km of fiber, an appreciable signal intensity on the detectors can only be recorded by raising the pump power to  $P_{\text{sat}}$ . As a result, we observe an increased  $g^{(2)}(0) = 0.40$  due saturation of the QD transition and increasing background contribution.

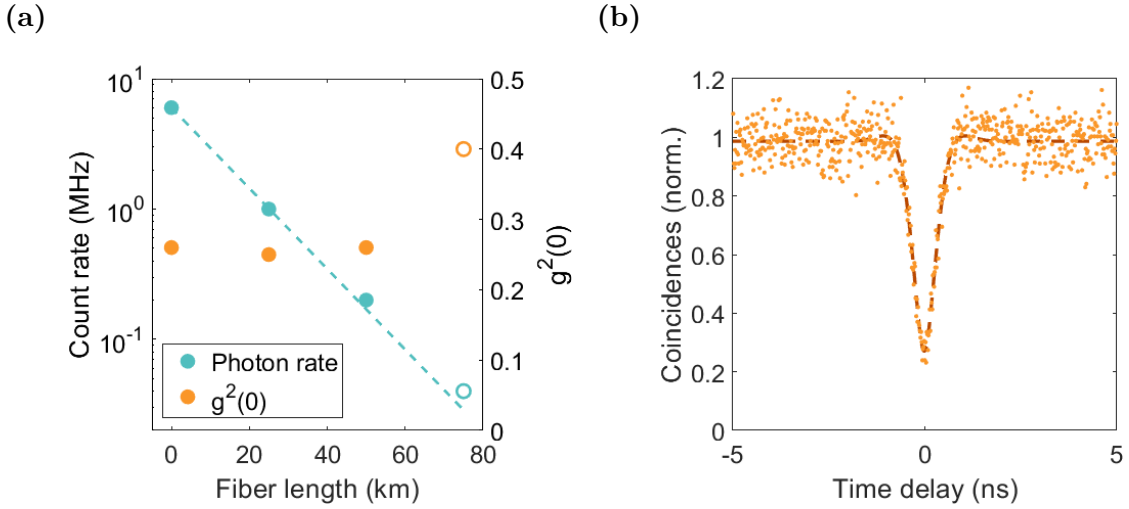


Figure 5.11: (a) Single photon rates and extracted values of  $g^{(2)}(0)$  as a function of the fiber length between the source and the SNSPDs measured on the brightest transition at  $\lambda=1331$  nm under above-band CW laser excitation. The empty circles indicate data acquired after raising the pump power to  $P_{\text{sat}}$ . The attenuation value of 0.31 dB/km is extracted by fitting the first 3 data points (dashed line). (b) Second order photon correlation measured with 50 km of fiber between the source and the SNSPDs.

### 5.3.5 Reproducibility

For large-scale applications of QD-based single photon sources, the fabrication of multiple devices with similar performance is highly desirable. Despite the excellent results reported in literature for individual optimized bullseyes [76, 77, 128], the repeatability of their performance remains an open question. In this framework, our wafer scale flip-chip process described in Section 3.3.1 offers the advantage of yielding a large amount of material ready for the fabrication of CBGs. In Section 5.3.1 we reported a good agreement between the reflectivity measurements over different CBGs and the corresponding numerical simulations. Here we show reproducibility of the emission properties of QDs embedded into CBGs with similar design parameters by repeating the micro-PL and time-resolved characterization over multiple devices.

The results for a second exemplary CBG ( $a = 600$  nm,  $R = 520$  nm) are reported in Figure 5.12a: once again we observe a plurality of emission lines from a single QD,

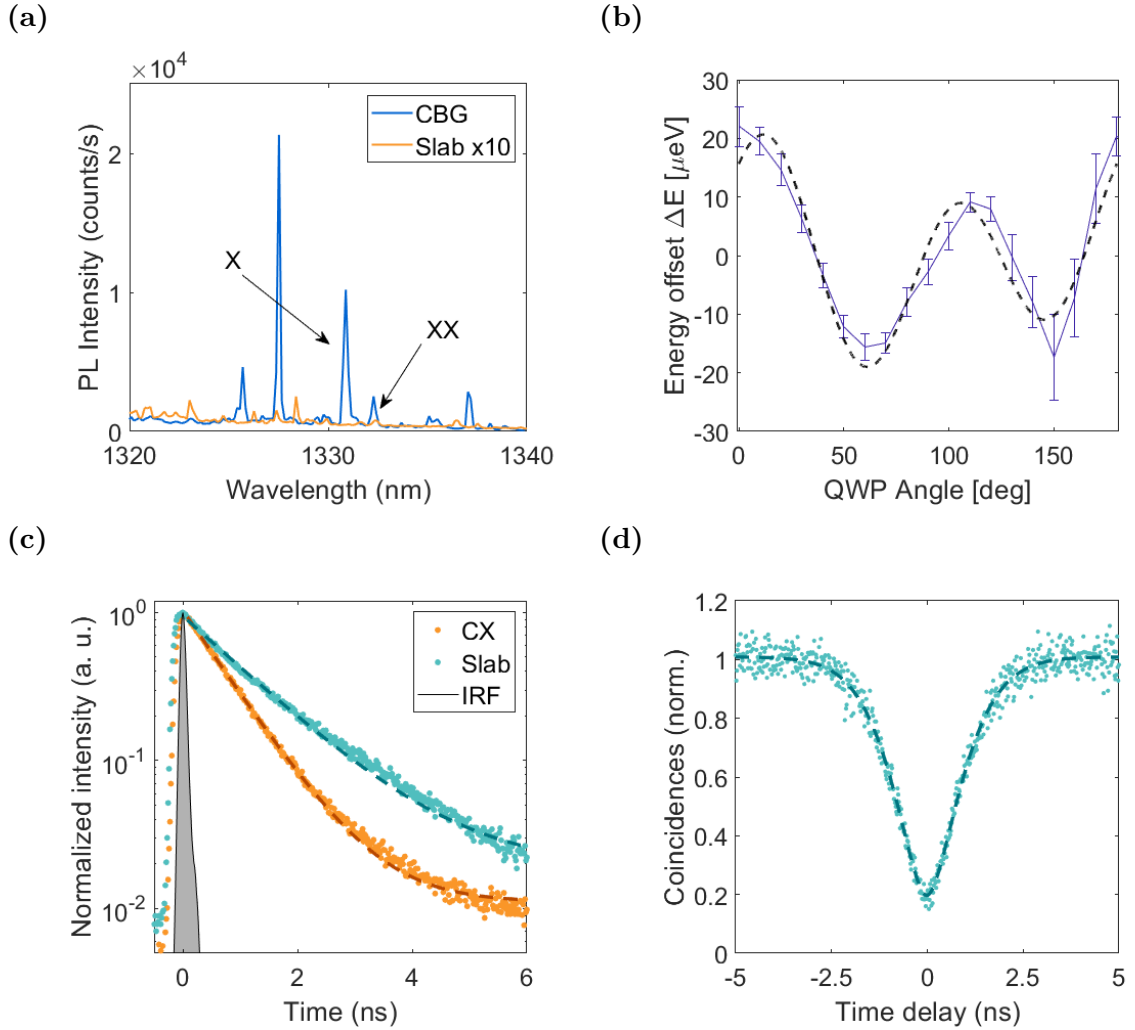


Figure 5.12: (a) Micro-PL signal from a CBG (blue) and from an unetched area of the sample (orange) under above-band CW laser excitation. The signal measured on the slab is multiplied by a factor of 10. (b) Fine structure splitting measurement with fit of the energy offset according to [31], indicating a fine structure splitting of  $84.1(\pm 2.9) \mu\text{eV}$ . (c) Decay trace of the brightest CX transition from the CBG at  $\lambda=1328 \text{ nm}$  and of an exemplary reference line from the unetched slab measured under above-band pulsed excitation at 40 MHz. The dashed lines represent the exponential fit of the decay traces, yielding a CX lifetime of 756 ps. (d) Example of second order photon correlation measured on the brightest transition at  $\lambda=1328 \text{ nm}$  under above-band CW laser excitation, with  $g^{(2)}(0) = 0.22$ .

much brighter than the orange line representing a typical PL spectrum acquired on the unetched area of the sample multiplied by a factor of 10. The comparison confirms that the CBG provides a clear enhancement of the signal intensity, although slightly less pronounced with respect to the device analyzed previously. Similarly to the pattern reported in Figure 5.7b, the brightest charged transition is followed by an exciton-biexciton pair at longer wavelength, with a fine structure splitting of  $84.1(\pm 2.9) \mu\text{eV}$  extracted from polarization-resolved measurements (Figure 5.12b).

Figure 5.12c shows the time-resolved photoluminescence signal of the charged transition at  $\lambda=1328$  nm, which decays with a time constant of 756 ps. From the comparison with the average lifetime of  $\tau_{\text{av}} = 1.584$  ns measured on the slab we estimate a Purcell factor of  $\sim 2$ . Given the similar design parameters and the fact that a similar lifetime was extracted for the X line, we attribute the difference with the CBG analyzed in the previous sections to a larger displacement of the QD from the centre of the device. As expected, the coincidence histogram of the charged transition (Figure 5.12d) exhibits a dip at  $\tau=0$  ns with  $g^{(2)}(0) = 0.22$ , which confirms the non-classical nature of the emitted light.

In Figure 5.13a we compare the integrated PL intensity at saturation  $I_{\text{sat}}$  for 40 transitions measured on those CBGs (orange, 4 data points per device) and 40 transitions measured on various positions of the unetched slab (teal). The average PL intensity at saturation recorded on the bare slab is  $I_{\text{sat}}^{\text{slab}} = 297$  cts/s with a standard deviation of 190 cts/s. As for the CBGs, we observe an average PL intensity of  $I_{\text{sat}}^{\text{CBG}} = 24129$  cts/s (standard deviation: 22129 cts/s), corresponding to an average enhancement factor of almost two orders of magnitude with no dependence on the operational wavelength. The Purcell-enhanced CX transition shown in Figure 5.7b exhibits the brightest PL signal ( $I_{\text{sat}} \sim 160470$  cts/s), corresponding to a remarkable enhancement factor of  $\sim 540$  compared to the bare slab.

It is important to underline that more than half of the transitions included in Figure 5.13a are not coupled to any cavity mode. Nevertheless, they still benefit from the improved extraction efficiency over a broad spectral range guaranteed by the CBGs. Furthermore, we observe that QDs embedded into a CBG require a lower

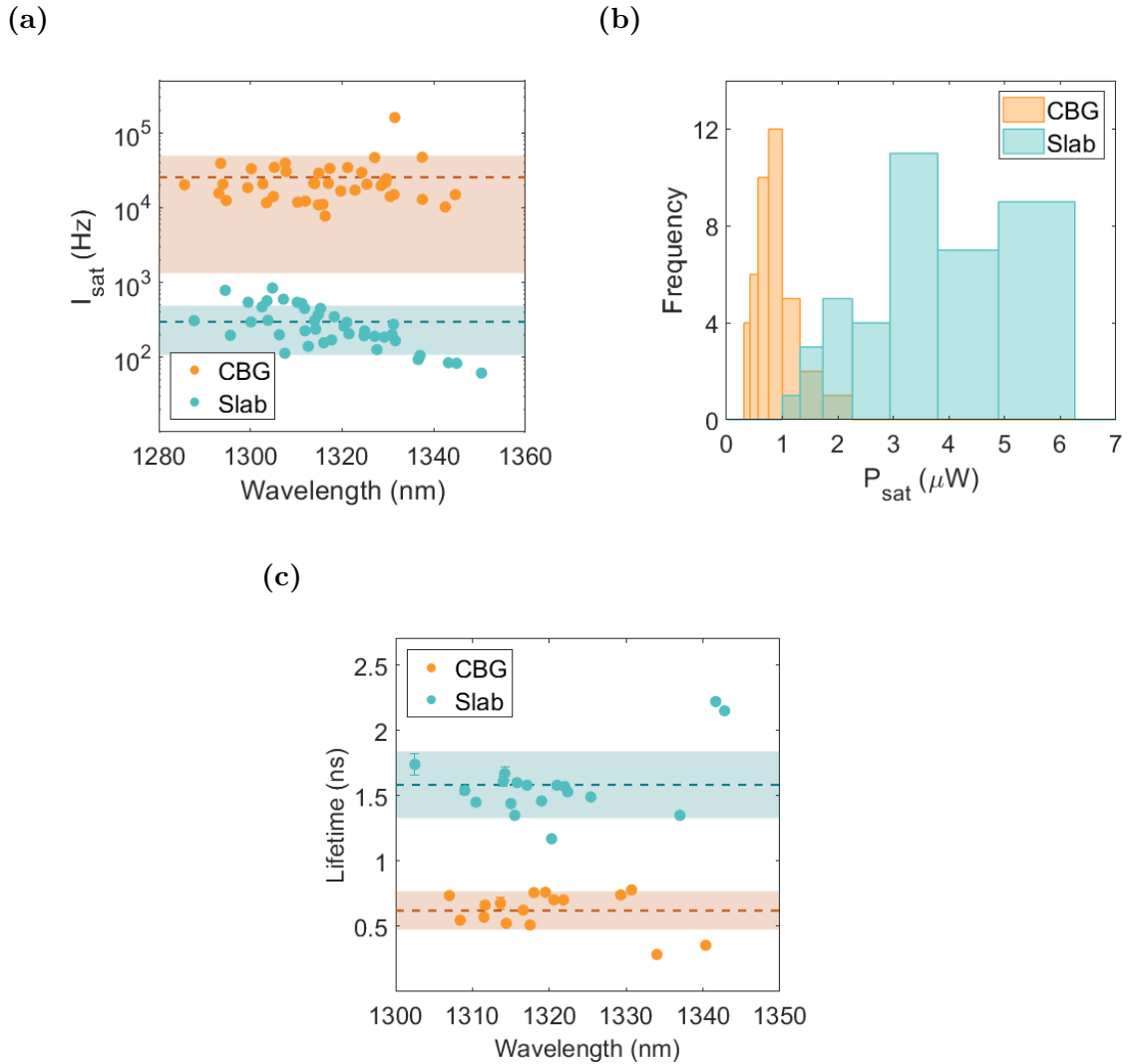


Figure 5.13: (a) Integrated PL intensity at saturation  $I_{\text{sat}}$  of 40 transitions measured on 10 different CBGs (orange) and 40 transitions measured on the unetched slab (teal). The dashed lines and shaded areas represent the mean values and corresponding standard deviation, respectively. (b) Laser power  $P_{\text{sat}}$  required to reach saturation of the QD emission. (c) Radiative lifetimes of 16 transitions measured on 10 different CBGs (orange) and 18 transitions measured on unetched slab (teal). The dashed lines and shaded areas represent the mean values and corresponding standard deviation, respectively.

pump power  $P_{\text{sat}}$  to reach saturation (Figure 5.13b). This result confirms our initial hypothesis that the presence of the circular grating helps focusing the incoming light towards the central disk for a more efficient laser excitation that may reduce the charge noise around the QD.

Finally, Figure 5.13c summarizes the results of our time-resolved measurements over multiple devices. As mentioned previously, the teal data points indicate the radiative lifetimes of 18 transitions from 5 different locations on the bare slab. The corresponding average lifetime of  $\tau_{\text{slab}} = 1.584$  ns and standard deviation  $\sigma_{\text{slab}} = 254$  ps are represented by the teal dashed line and shaded area, respectively. On the other hand, the orange data points show the radiative lifetimes of 16 spectral lines from 10 different CBGs, with a mean value of  $\tau_{\text{CBG}} = 620$  ps and standard deviation  $\sigma_{\text{CBG}} = 146$  ps. Consequently, we estimate an average Purcell factor of  $\sim 2.5$  for the 10 devices examined with no dependence on the operational wavelength. Those results confirm that the broadband properties of the CBGs facilitate the production of multiple devices with similar performances even with a non-deterministic fabrication method.

## 5.4 Conclusions

In conclusion, this chapter presents the design and characterization of single-photon sources in the telecom O-band based on InAs QDs in hybrid circular Bragg gratings. First, starting from the results of a previous theoretical work [127] we investigated and optimized the performances of the devices using 3D FEM simulations in the frequency domain. Then, the devices were fabricated on a GaAs sample obtained with a flip chip post-growth process consists of thermocompression Au-Au wafer bonding followed by mechanical lapping and a selective wet etching. It is important to underline that this process happens on wafer scale, which is crucial for the scalability of the technology.

Using an optimised device we showed bright single-photon emission from an individual QD, with Purcell factor  $> 5$  and single-photon rate  $> 10$  MHz measured

using SNSPDs with  $\sim 60\%$  efficiency at 1310 nm. We also demonstrated that such a source can provide a Purcell factor  $> 4$  over a broad wavelength range of 7 nm, leading to the simultaneous enhancement of multiple transitions and facilitating the spectral overlap with the cavity mode. Moreover, we showed that the non-classical nature of the CBG emission is preserved over long distances, with a remarkable rate of 200 kHz recorded after the propagation in 50 km of standard optical fiber. Finally, we investigated the reproducibility of the performances and demonstrated that the optical and quantum properties are replicated for QDs embedded into CBGs with similar design parameters. An average Purcell factor of  $\sim 2.5$  was extracted from the characterization of 10 different devices, proving that, even with a non-deterministic fabrication method, the design is quite robust against common fabrication issues in terms of imperfect sidewalls etching and lateral displacement of the QD as predicted by a previous theoretical work [127].

The source presented in this chapter may be useful for fiber-based single-photon applications, such as long-distance quantum communications and distributed quantum computing.



# 6 Design of high-performance single-photon sources in the telecom C-band

In the previous chapter we showed that circular Bragg gratings fabricated on GaAs slabs can be used for the efficient extraction of photons from InAs/GaAs QDs emitting in the telecom O-band. Here we extend that approach to the telecom C-band, presenting a design optimization for circular Bragg gratings fabricated on InP slabs and operating around 1550 nm. We also study a design variation compatible with electric field control.

## 6.1 Introduction

The last few years have seen an important progress in the development of single and entangled photon sources based on semiconductor quantum dots, which have started reshaping the landscape of optical quantum technologies [141]. However, the most mature devices are based on InAs/GaAs QDs and operate in a wavelength range around 900 nm [76, 77, 34]. This prevents the integration with the standard optical fibre infrastructure, since light at 900 nm is not single mode in telecom fibres and experiences a strong attenuation  $> 1$  dB/km. Recent efforts have focused on devices operating in the telecom O-band [128, 135, 142] where the attenuation is only 0.35 dB/km, but for long-distance quantum communication it is desirable to exploit the low-loss window of silica fibres in the telecom C-band, where attenuation can be as little as 0.12 dB/km [143].

Quantum light sources based on InAs QDs emitting directly around 1550 nm have been recently developed using two different approaches: they can be either grown on

GaAs-based materials by employing metamorphic buffer layers for strain relaxation [104] or on InP substrates, which have smaller lattice mismatch with respect to the QD material and therefore allow for the deposition of larger and less strained islands with consequently longer emission wavelength [144, 145]. Between those two approaches, QDs grown on InP have shown superior performances in the coherence of the emission [146, 147], which is a crucial figure of merit for efficient quantum communication protocols. However, those results have been achieved with simple structures such as planar DBR microcavities and the investigation and development of more complex devices such as circular Bragg gratings is highly desirable to improve the efficiency of quantum light sources based on the InP material system.

Moreover, the original layout of hybrid CBGs is not compatible with electric field control because the central disk is completely isolated from the rest of the semiconductor slab. A recent work [148] tried to overcome this problem by combining a CBG with a doped bottom DBR mirror, achieving an efficiency of 24%. The more advanced concept of incorporating a CBG into a vertical hybrid passive cavity [149] could in principle increase the efficiency up to 79% for a 8 nm bandwidth, but appears very challenging to implement in practice because it requires etching narrow trenches with straight sidewalls and aspect ratios around 10:1. Overall, none of the variations proposed so far can provide the combination of moderate Purcell enhancement and high extraction efficiency in a broad range that makes the original design so attractive.

In this chapter we present a theoretical investigation of hybrid CBGs fabricated on InP slabs: first we perform an in-depth analysis of the design parameters and their influence on Purcell factor and extraction efficiency. Then we focus on the direct coupling in a SM fibre, which is crucial for applications that require compact and deployable quantum light sources that can be used outside of the lab environment. Finally, we propose a modified device design that is compatible with electric field control and maintains optical performances similar to the ones shown by the original structure.

## 6.2 Device modeling

Figure 6.1a shows a schematic cross-section of the device investigated, which consists of an InP disk surrounded by a grating, an insulating layer of SiO<sub>2</sub> and a backside gold mirror. Literature values are used for the refractive indices of all materials, as summarized in Table 6.1.

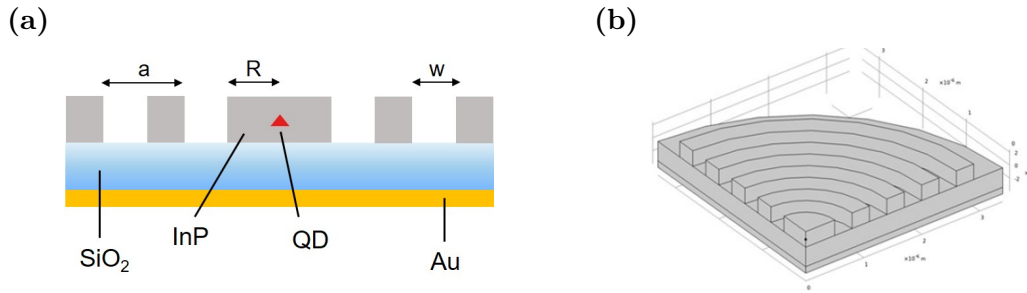


Figure 6.1: (a) Schematic of the cross-section of the CBG structure investigated in this design study, with a single quantum dot embedded in the central disk. (b) Three-dimensional simulation domain, reduced to a quarter by exploiting the symmetry in the  $xz$  and  $yz$  planes as explained in Section 3.2.

Material	$n$	$k$	Ref.
InP	3.1544	0	[150]
SiO <sub>2</sub>	1.45	0	[151]
Au	0.402	10.844	[152]

Table 6.1: Refractive index values used in the numerical simulations.

The design parameters initially studied are the thickness of the different layers ( $t_{\text{InP}}$ ,  $t_{\text{SiO}_2}$ ,  $t_{\text{Au}}$ ), the radius  $R$  of the central disk, the number  $N$  of concentric InP rings, their lattice constant (i.e. periodicity)  $a$  and the width of the trenches  $w$ . For this design study we employed 3D FEM simulations in the frequency domain using the Wave Optics module of COMSOL Multiphysics. A view of the three-dimensional simulation domain is reported in Figure 6.1b. As already explained in Section 3.2,

we exploit symmetry properties to reduce the size of the model and solve only one quarter of the full domain. In particular, we set a first cut line along the  $xy$  plane with perfect electric conductor boundary conditions ( $n \times E = 0$ ) and a second one along the  $yz$  plane with perfect magnetic conductor boundary conditions ( $n \times H = 0$ ) [126].

Meshing the domains is a particularly important step in simulations that involve a 3D model because it has a direct impact on both the computational requirements (memory and time) and the accuracy of the solution. In electromagnetic simulations each wavelength must be resolved with a minimum of three elements, even if it is good practise to use at least five for accurate results. The main challenge is therefore given by the elements with higher refractive index (InP in this case), where the shorter effective wavelength requires very fine mesh elements. Since we expect the optical mode to be confined in the central area of the CBG, the central disk and the first three concentric rings are meshed more finely with seven elements per wavelength, while we use only three for the outer rings. All the other domains are meshed with five elements per wavelength. The model is also surrounded by perfectly matched layers (PMLs, not shown in Figure 6.1b), i.e. artificial strongly absorbing layers that simulate open boundaries and avoid undesired reflections of the emitted radiation. The PMLs are meshed with a rectangular swept mesh. Finally, an electric dipole source oriented along the  $y$  axis is placed in the centre of the InP disk ( $x=0, y=0$ ) at half of the slab thickness, in order to simulate the single photon emission from a quantum dot.

## 6.3 Numerical simulations

### 6.3.1 Optimization of Purcell factor and collection efficiency

The aim of the first set of simulations is to design a device that can offer simultaneously moderate Purcell enhancement and high efficiencies in a broad range of wavelengths. As explained in Section 5.2.1, the Purcell factor  $F_p$  is obtained as the ratio between

the power emitted by the dipole source embedded in the CBG and the power emitted by the same dipole in semi-infinite InP. In order to evaluate the efficiency of the devices and identify any potential source of losses, we also define three additional quantities [129, 127]:

1. The extraction efficiency is the percentage of emitted radiation that can escape into the air domain above the device.
2. The far-field efficiency in a certain NA is the far-field intensity integrated on such NA divided by the far-field intensity in the upper air hemisphere.
3. the dipole collection efficiency (DCE) in a certain NA is the product of the extraction efficiency and the corresponding far-field efficiency.

The design process consists of a series of FEM simulations aiming to find the best compromise between Purcell factor, extraction efficiency and bandwidth. The choice of the initial parameters was based on previous works at shorter wavelengths [125, 129, 127]. In particular, we set the initial thickness of InP to  $t_{\text{InP}} = \lambda_{\text{eff}}/2$  to have only a single TE mode supported by the slab, the initial grating period to  $a = \lambda/n_{\text{TE}}$  to satisfy the second-order Bragg condition and the radius of the central disk to  $R = \lambda_{\text{eff}}$ . Starting values for the width of the trenches and the thickness of SiO<sub>2</sub> and Au were arbitrarily set to  $w = 0.5 \cdot a$ ,  $t_{\text{SiO}_2} = 300$  nm and  $t_{\text{Au}} = 100$  nm. It is worth noting that the thickness of Au required for thermocompression wafer bonding is usually around 1  $\mu\text{m}$ . Nevertheless, we observed that a 100 nm layer is enough to create an efficient mirror and therefore decided to keep this parameter fixed to minimize the size of the computational domain.

### Optimized design

The final set of design parameters produced by the numerical optimization is:  $t_{\text{InP}} = 280$  nm,  $t_{\text{SiO}_2} = 360$  nm,  $R = 660$  nm,  $a = 785$  nm,  $w = 350$  nm,  $N = 4$ . The performance of the optimized device are summarized in Figure 6.2a, which shows that collection efficiencies close to 90% in NA=0.65 are expected in the whole telecom

C-band, together with a cavity mode exhibiting  $\text{FWHM} = 16 \text{ nm}$  and Purcell factor up to 15. It is important to underline the large bandwidth of the device, which guarantees moderate Purcell enhancement and efficient photon collection in a broad range of wavelengths encompassing both the X and XX spectral lines, typically separated by 5-10 nm in InAs/InP QDs [108, 147]. Moreover, the presence of the diffractive grating combined with the backside Au mirror makes the emission from the CBG highly directional, which is clearly observable both in the near-field and far-field intensity distribution. This directionality guarantees high collection efficiency even in smaller NA, with DCE already close to 80% for  $\text{NA}=0.4$  (Figure 6.2b).

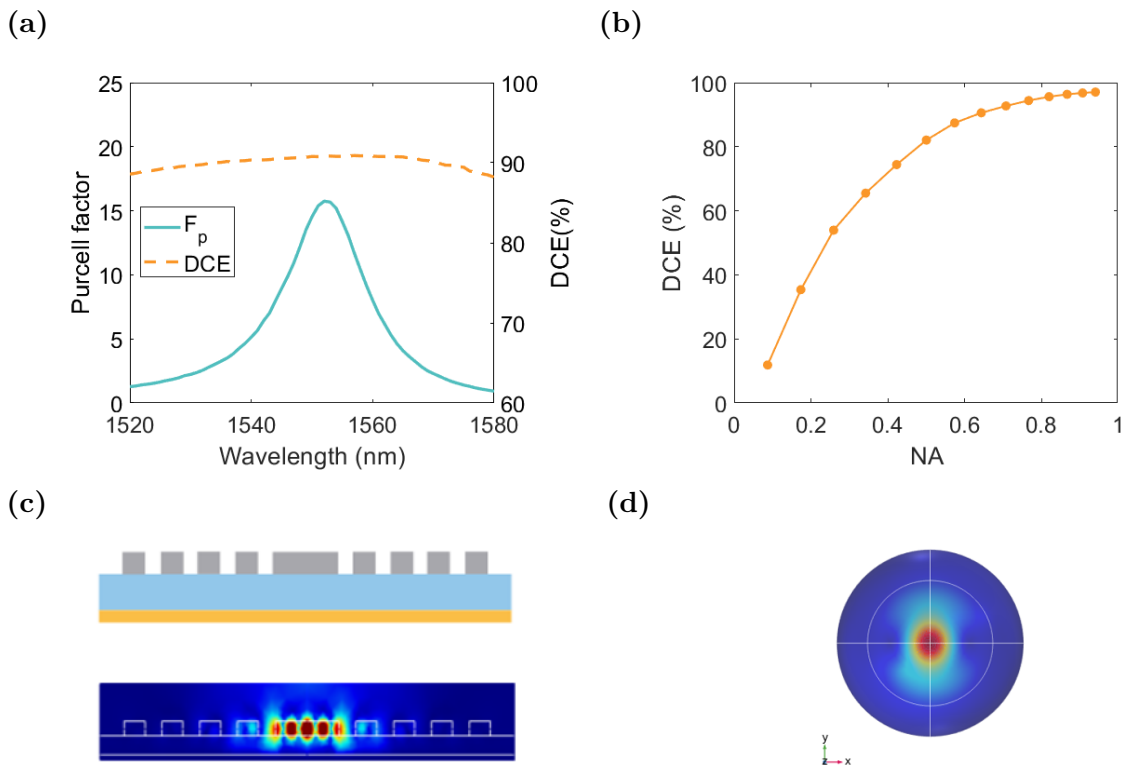


Figure 6.2: (a) Performance of the optimized CBG with Purcell factor (solid line) and DCE in  $\text{NA}=0.65$  (dashed line) as a function of wavelength. (b) DCE of the optimized CBG calculated for  $\lambda=1552 \text{ nm}$  as a function of the collecting NA. (c) Near-field intensity distribution of the optical mode localized in the central disk. (d) Corresponding far-field intensity distribution at resonance projected on a sphere with radius  $r = 1 \text{ mm}$ . The inner circle represents  $\text{NA}=0.65$ .

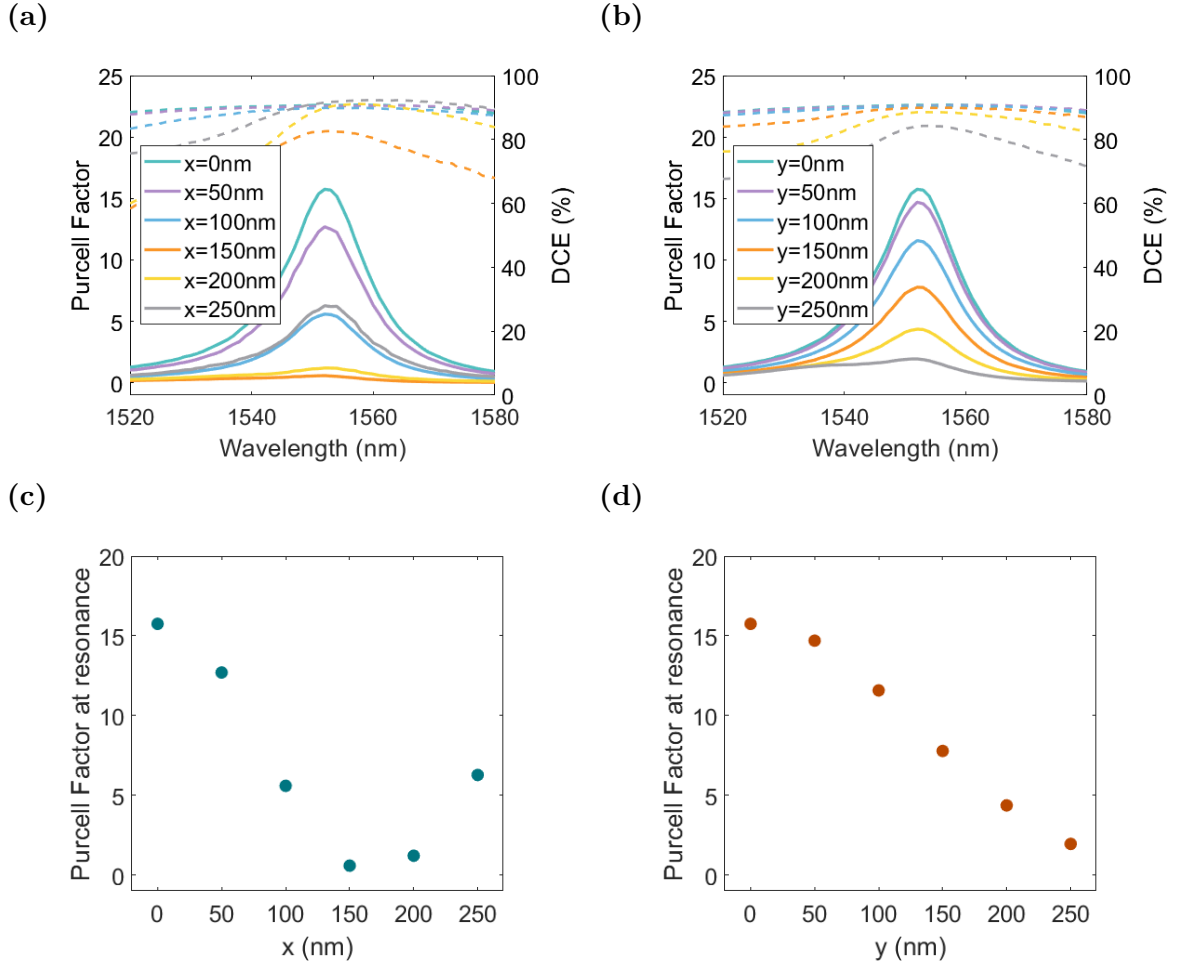


Figure 6.3: (a) Purcell factor (solid lines) and DCE in  $NA=0.65$  (dashed lines) for different positions of the dipole along the x axis ( $y=0$ ). (b) Purcell factor (solid lines) and DCE in  $NA=0.65$  (dashed lines) for different positions of the dipole along the y axis ( $x=0$ ). (c) Purcell factor at resonance ( $\lambda=1552$  nm) as a function of the dipole position along the x axis. (d) Purcell factor at resonance ( $\lambda=1552$  nm) as a function of the dipole position along the y axis.

When a CBG is fabricated, it is unlikely to find a quantum dot in the ideal position ( $x=0, y=0$ ) at the centre of the disk. For an accurate estimate of the behaviour of a real device it is important to simulate this imperfection by moving the dipole source away from the centre. Therefore, we ran a second set of simulations maintaining the original orientation of the dipole, but placing it at different positions along the  $x$  and  $y$  axes as shown in Figure 6.3. When the dipole is moved along the  $x$  axis the DCE stays almost constant up to  $x = 100$  nm, then it drops to 80% around resonance with a more pronounced wavelength dependence. On the other hand, the Purcell factor decreases steeply, giving  $F_p = 5$  for  $x = 100$  nm. In order to keep  $F_p$  closer to the original value of 15, a smaller displacement up to 50 nm is desirable. A similar behaviour of the DCE is observed for the  $y$  axis, while the Purcell factor drops slowly as a function of the displacement. This asymmetrical behaviour originates from the preferential orientation of the dipole source and the consequent profile of the emitted field.

Thanks to the recent progress in marker-based fabrication techniques [153], where first a PL imaging system is used to localize a single QD with respect to alignment features [154, 155] and then the device is fabricated around the target emitter by EBL, deterministic fabrication of CBGs with high lateral accuracy ( $< 30$  nm) has already been achieved [126, 132]. Therefore, the fabrication of the proposed InP CBG is expected to show good robustness against a lateral displacement of the QD embedded in the device.

### **Influence of the design parameters**

After determining the optimal device design, it is important to analyze the individual design parameters and understand their influence on the performance of the CBG. First, we focus on the effect of the wafer structure (i.e.  $t_{\text{InP}}$  and  $t_{\text{SiO}_2}$ ) on the Purcell factor and collection efficiency. As shown in Figure 6.4a, a variation of 10 nm in the slab thickness leads to a 10 nm wavelength shift in the cavity mode, maintaining a DCE around 90% at resonance.

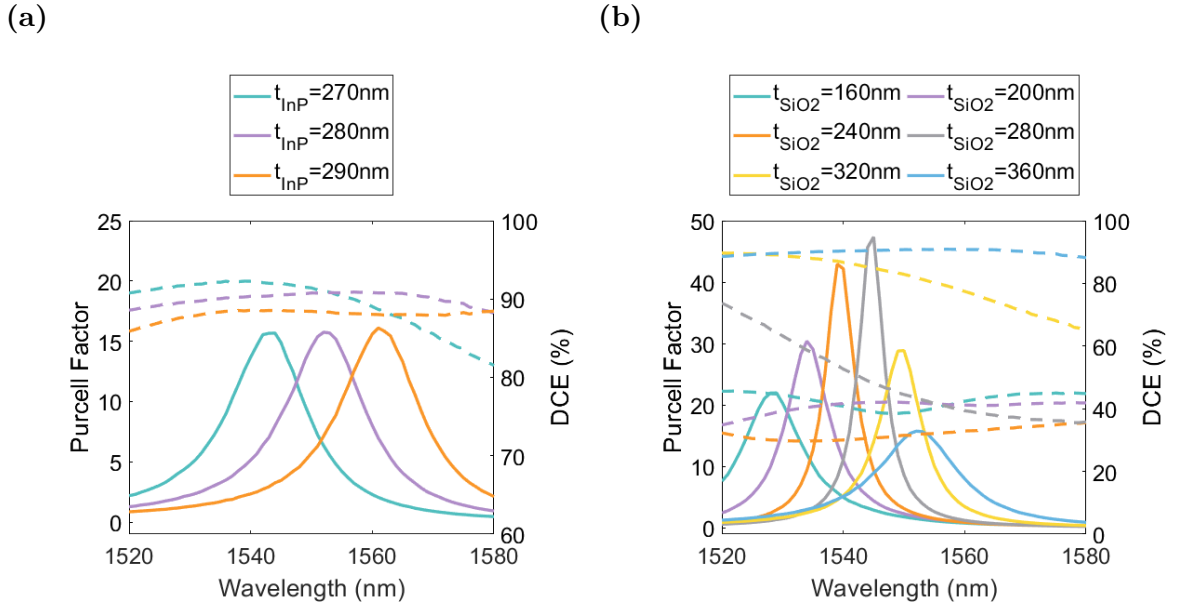


Figure 6.4: Influence of the wafer structure on the performance of the CBG: Purcell factor (solid lines) and DCE in  $\text{NA}=0.65$  (dashed lines) as a function of wavelength for (a) three different values of  $t_{\text{InP}}$  and (b) six different values of  $t_{\text{SiO}_2}$ .

Modifying the thickness of  $\text{SiO}_2$  leads to stronger variations in both  $F_p$  and DCE (Figure 6.4b). As explained by Rickert et al. [127], the variation of  $F_p$  originates from the change in the Q-factor of the vertical cavity created by the presence of the Au mirror. As a result, the maximum Purcell factor is achieved when the optical path between the dipole source and the mirror is close to a multiple of  $\lambda/2$ . On the other hand, maximizing  $F_p$  does not guarantee a good collection efficiency. In fact,  $t_{\text{SiO}_2}$  influences also the optical path difference between the photon directly emitted into the air and the ones reflected by the Au mirror and, consequently, the result of their interference which determines the far-field distribution. In our case, the choice of  $t_{\text{SiO}_2} = 360\text{ nm}$  leads to a lower  $F_p$  but allows us to achieve a high and almost wavelength-independent DCE in the whole telecom C-band. It is worth noting that both InP and  $\text{SiO}_2$  can be deposited with high accuracy by MBE (or MOVPE) and PECVD respectively, therefore we do not expect any deviation from the ideal behaviour related to fabrication imperfections.

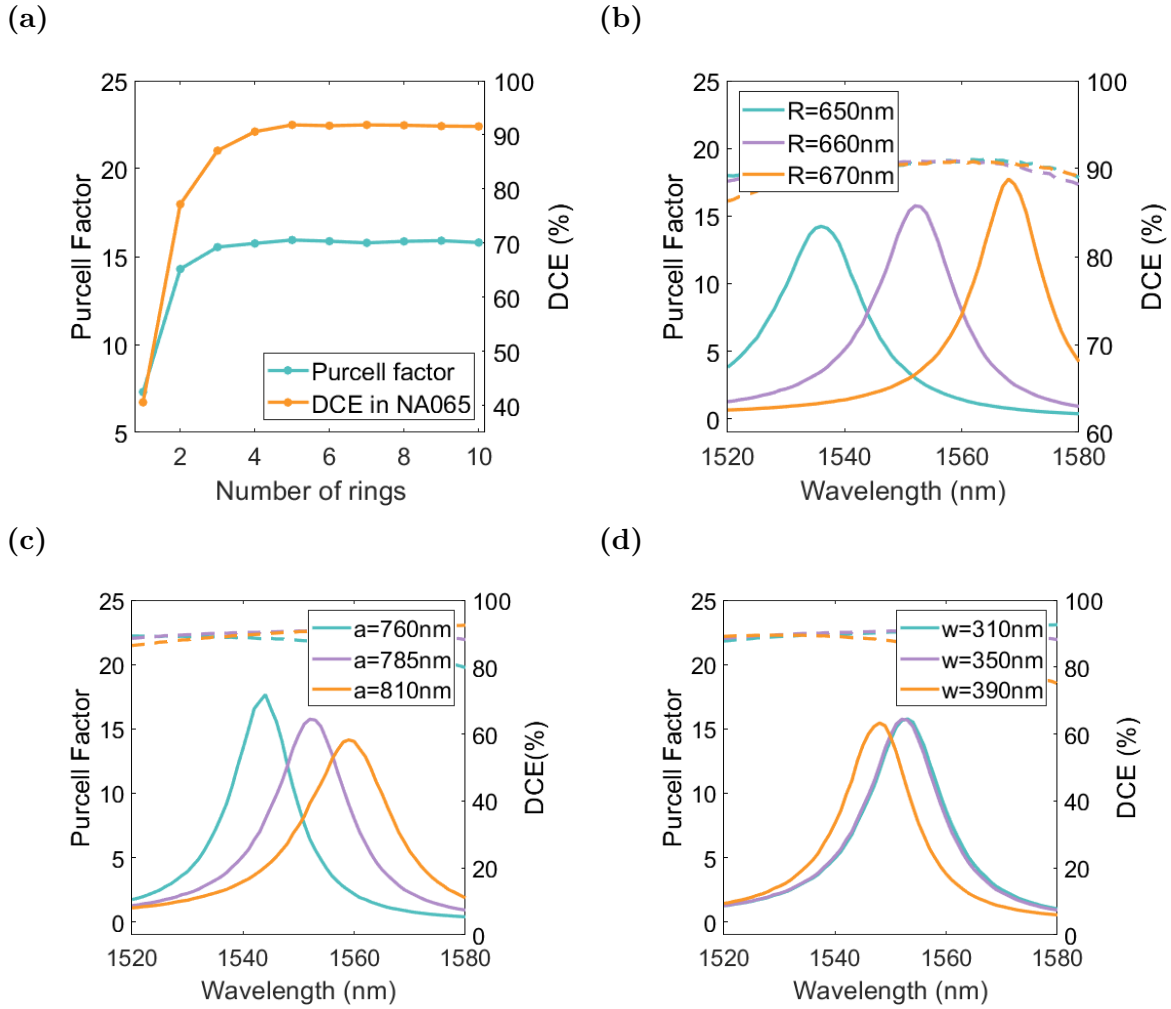


Figure 6.5: Influence of the etching parameters on the performance of the CBG. (a) Purcell factor and DCE in NA=0.65 calculated for  $\lambda=1552$  nm as a function of the number  $N$  of concentric rings. (b-d) Purcell factor (solid lines) and DCE in NA=0.65 (dashed lines) as a function of wavelength for three different values of (b) the central disk radius  $R$ , (c) the lattice constant  $a$  and (d) the width of the trenches  $w$ .

Next, we examine the effect of the individual device parameters. Figure 6.5a shows that the InP CBG requires only 4 rings to achieve the desired performance. Such a low number of grating elements is probably not practical in a real device since such a small area would be challenging to find under the optical microscope. However, this result demonstrates that only the first few rings must be free from fabrication imperfections in order to guarantee the desired outcome. Figure 6.5b presents the influence of the central disk radius on the optical properties of the CBG, where a 10 nm variation of  $R$  shifts the resonance wavelength by approximately 20 nm but at the same time has negligible effect on the DCE. A similar but less pronounced red-shift happens when the lattice constant is increased (Figure 6.5c): here the cavity mode moves by approximately 10 nm when  $a$  is changed by 15 nm and again the DCE does not show dramatic alterations. Finally, small variations of  $w$  have a negligible effect on the cavity mode, but accentuate the wavelength dependence of the DCE which may now drop faster when moving off resonance (Figure 6.5d). These calculations demonstrate that small variations of  $R$  and  $a$  can be used to adjust the resonance wavelength of the InP CBG with minimal impact on the collection efficiency. This ability is crucial for the fabrication of optimized devices, with the pre-selection of an optimal QD and the subsequent definition of the CBG by in-situ electron beam lithography.

### 6.3.2 Direct coupling into SM fibre

For the development of compact and user-friendly QD-based sources intended to be used outside the lab environment, direct fibre coupling of the emitted photons is most desirable [156, 157]. In fact, having an optical fibre directly attached to the devices would reduce the size and complexity of the system and guarantee high alignment robustness [158, 159]. Therefore our second set of simulations investigates the coupling into SM fibre: we select the best fibre to achieve high coupling efficiency and present a further optimization of the CBG aiming to maximize this parameter, which is the most crucial figure of merit for a bright plug-and-play quantum light source.

### Simulations of coupling efficiency

In our study we consider 4 types of commercial SM fibres (Nufern), with specifications at  $\lambda=1550$  nm reported below (Table 6.2).

Fibre	$n_{\text{core}}$	$d_{\text{core}}$ (um)	$n_{\text{cladding}}$	$d_{\text{cladding}}$ (um)	NA
980HP	1.4507	3.6	1.4457	125	0.12
UHNA1	1.4709	2.5	1.444	125	0.28
UHNA3	1.4858	1.8	1.444	125	0.35
UHNA4	1.4858	2.2	1.444	125	0.35

Table 6.2: Specifications of the SM fibres investigated in our numerical simulations.

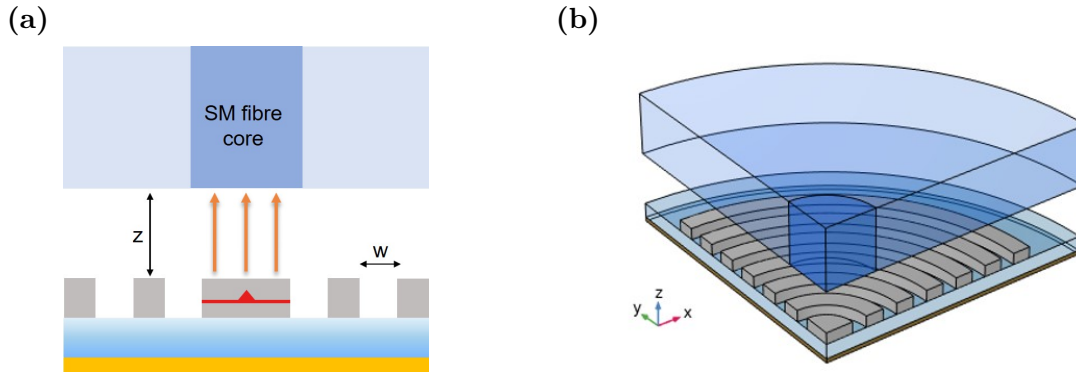


Figure 6.6: (a) Schematic of the model created to investigate the fibre coupling efficiency, with a SM fibre at a distance  $z$  from the device. (b) Corresponding simulation domain in Comsol.

The first step to determine the coupling efficiency is the calculation of the propagating modes supported by each fibre. Since those depend only on the characteristics of the fibres which are invariant in the propagation direction, the simulations can be carried out on a 2D cross-section reducing the computational requirements. Then, we determine the profile of the field emitted by a dipole source embedded in the CBG. The presence of a fibre near the device influences this profile and therefore must be included in the three-dimensional model. Figure 6.6 shows our simulation domain,

where we assume that the fibre is attached on top of the device at a distance  $z$ , perfectly aligned in the axial direction and with vacuum ( $n=1$ ) in the gap. The last step is the evaluation of the overlap between the emitted field  $\mathbf{E}_s$  and the fundamental mode of the fibre  $\mathbf{E}_m$ . According to [160], the overlap integral can be calculated using the z-component of the Poynting vector:

$$S_{s,m} = \frac{1}{2} \int \mathbf{E}_s \times \mathbf{H}_m^* dS \quad (6.1)$$

where the integration is performed over a cross-section of the fibre. The power flux coupled into the mode  $m$  is then given by:

$$P_{s,m} = |S_{s,m}|^2 \quad (6.2)$$

and the mode coupling efficiency (MCE) can finally be extracted dividing  $P_{s,m}$  by the total power emitted by the dipole source.

In Figure 6.7a we report the coupling efficiency as a function of the distance  $z$  between the fibre and the device calculated at  $\lambda=1550$  nm for the four different SM fibres described above. Only a small fraction (up to 22.8%) of the light emitted by the CBG is coupled into the 980HP fibre, while using the UHNA1 (NA=0.28) fibre allows a remarkable improvement of the MCE up to 64.4%, with an initial plateau followed by a linear decay for  $z > 2 \mu\text{m}$ . Even higher efficiencies can be achieved with the more extreme versions UHNA3 and UHNA4. All the curves also exhibit moderate oscillations caused by Fabry-Perot interference in the gap region, with the maximum coupling efficiency at  $z \sim 800$  nm.

Next, we examine the wavelength dependence of the MCE. As shown in Figure 6.7b, the coupling into 980HP suffers from significant losses, while all the UHNA fibres enable efficient coupling in the whole telecom C-band. Once again, the best performances are delivered by the UHNA4 fibre, which guarantees a MCE>60% in the range 1520 nm - 1580 nm with a peak value of 68.5% at 1550nm. We attribute the superior performances of the UHNA fibres compared to the 980HP to the small mode field diameter (3-5  $\mu\text{m}$ ), that is very well matched with the intensity distribution of the CBG emission (Fig.6.8). Finally, it is worth noting that UHNA fibres can be

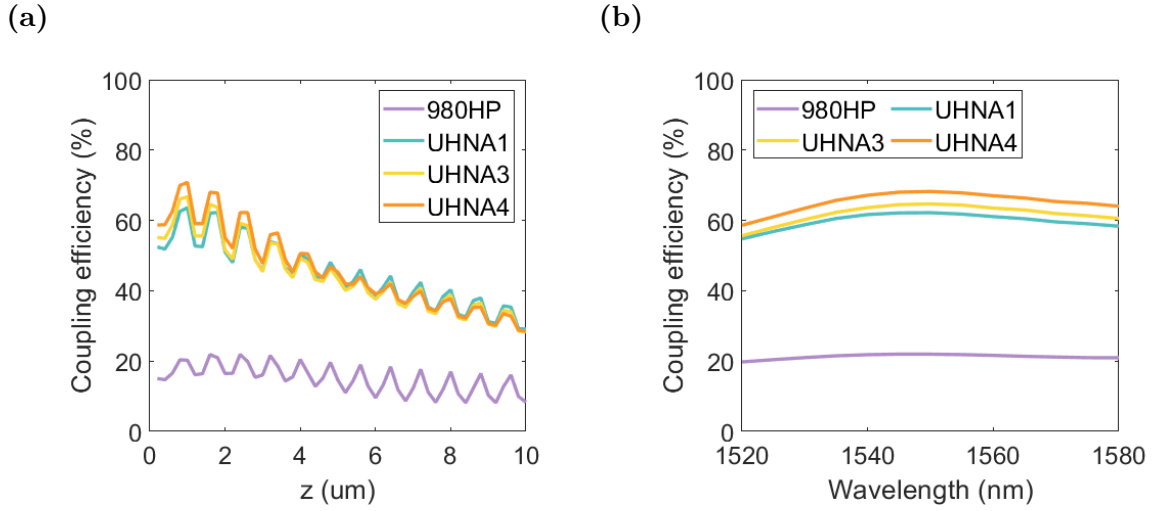


Figure 6.7: (a) Coupling efficiency into 4 different SM fibres calculated at resonance as a function of the vertical distance  $z$  between each fibre and the CBG. (b) Coupling efficiency as a function of wavelength for 4 SM fibres positioned at a distance  $z = 1.6 \mu\text{m}$  from the device.

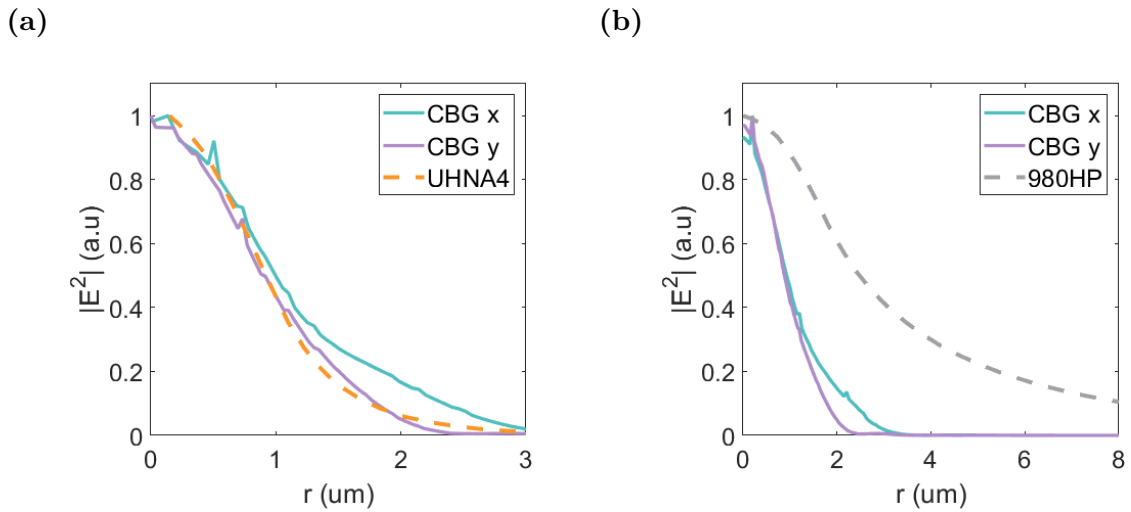


Figure 6.8: Comparison between the SM fibre mode profile at  $\lambda=1550 \text{ nm}$  and the corresponding profile of the radiation emitted by the CBG and at a distance  $z=1.6 \mu\text{m}$  for (a) UHNA4 fibre and (b) 980HP fibre. The different intensity distribution along  $x$  and  $y$  is caused by the orientation of the dipole source.

fusion spliced directly into standard SMF28 with very low losses ( $\leq 0.15$  dB) [161], which guarantees easy compatibility with standard fibre networks [162].

### Further device optimization

After determining the optimal strategy for direct fibre coupling of the photons emitted by the InP CBG, we analyze potential improvements in the device design aiming to reach even higher efficiencies. Since we demonstrated that small variations of the trench width have a negligible effect on the resonance wavelength (Figure 6.5d) and do not reduce the Purcell factor, we focus on this parameter and report the wavelength dependent MCE in UHNA4 fibre for different values of  $w$ . Figure 6.9a shows that etching trenches with a width of 370 nm provides even better coupling, with MCE above 71% at 1550 nm for  $z = 1.6 \mu\text{m}$ .

Moreover, we investigate an apodization of the InP grating, which is a well-known technique to engineer the mode profile in highly efficient couplers on SOI platforms [163, 164]. We propose an apodized design where the periodicity  $a = 785$  nm is kept constant and the width of the trenches is varied linearly along the length of the structure according to the formula:

$$w_i = a[1 - (F_0 + (i - 1)R_0)] \quad (6.3)$$

where  $F_0 = (a - w)/a$  is the initial filling factor of the unit cell and  $R_0$  is the apodization rate. The calculated efficiencies are presented in Figure 6.9b: the maximum MCE=71.7% occurs for  $F_0 = 0.52$  (i.e.  $w = 377$  nm) and  $R_0 = 0.005$ , but it is only 0.3% higher than the one provided by the uniform grating. Therefore, a linear variation of  $w$  does not provide any advantage in a real device. It might be possible to achieve higher efficiencies by apodizing simultaneously both the lattice constant and the width of the trenches [165]. However, this adds further complexity that should be avoided at in the initial stage of this project.

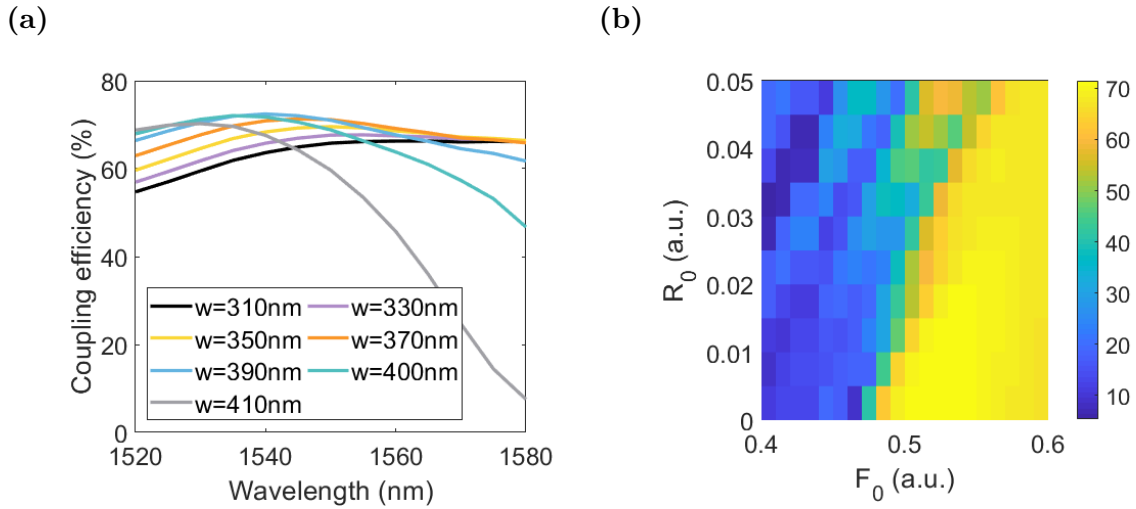


Figure 6.9: (a) Coupling efficiency into UHNA4 SM fibre as a function of wavelength for different widths  $w$  of the trenches in units of nm. The efficiency is calculated for  $z = 1.6 \mu\text{m}$ . (b) Coupling efficiency into UHNA4 SM fibre for an apodized CBG, as a function of the initial filling factor  $F_0$  and the apodization rate  $R_0$ . The efficiency is calculated for  $z = 1.6 \mu\text{m}$  and  $\lambda = 1550 \text{ nm}$ .

### 6.3.3 Proposal for an electrically driven circular Bragg grating

The structure of the CBG studied so far does not permit any direct electrical control of the QD emission. In fact, accommodating a pin diode structure in such a thin InP slab may be challenging because of Zn (p-dopant) diffusion [166, 167]. Furthermore, the fully etched circular trenches isolate the central disk from any type of metal contact placed outside the device. In the following section we present a further set of simulations where we study a modified design compatible with electric field control. We propose a wafer structure with increased  $t_{\text{InP}} = 400 \text{ nm}$ , which in principle is compatible with the growth of a n-doped layer at the bottom and a p-doped layer on top (Figure 6.10a) without making the InP slab too thick and therefore eluding losses related to higher order modes. As shown in Figure 6.10b, we also avoid etching fully circular trenches and leave four semiconductor bridges of width  $w_b$ , which connect the central disk to the n-type and p-type contacts placed outside the device.

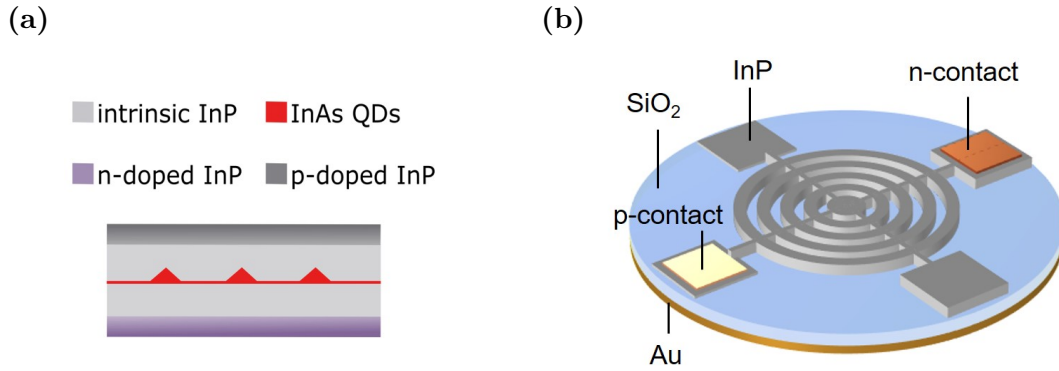


Figure 6.10: (a) Schematic of the modified InP slab as grown, including n-doped and p-doped layers. (b) Schematic of the proposed electrically controllable CBG. The metal contacts are deposited on two of the four squares outside the CBG, which are not in scale in this drawing.

Since the increased thickness of InP causes a significant variation in the simulation domain, the set of design parameters presented in the previous sections is used as starting point to run a new numerical optimization on the modified wafer structure, aiming to find the best compromise between Purcell factor, collection efficiency and bandwidth. Moreover, the introduction of the semiconductor bridges breaks the circular symmetry of the CBG. As a result, we expect the optical performance to be influenced by the orientation of the dipole source with respect to the bridges, which is quantified by the relative angle  $\alpha$ . For the purpose of this study, we decided to focus on the two limit cases reported in Figure 6.11, i.e.  $\alpha = 0^\circ$  and  $\alpha = 45^\circ$ , which represent two individual photon-emission events with defined polarization. The final set of design parameters produced by the numerical optimization keeping  $t_{\text{InP}} = 400$  nm fixed is:  $t_{\text{SiO}_2} = 280$  nm,  $R = 610$  nm,  $a = 740$  nm,  $w = 350$  nm,  $N = 4$ ,  $w_b = 200$  nm. The optical performance of the optimized device for the two different limit cases are summarized in Figure 6.12, which shows that collection efficiencies close to 70% in NA=0.65 are expected in the whole telecom C-band. In both cases, the cavity resonance is nicely confined in the central disk, exhibiting FWHM = 10 nm and Purcell factor up to 20. Noteworthy, the orientation of the dipole with respect to the bridges has a negligible effect on the DCE and causes only a small red shift

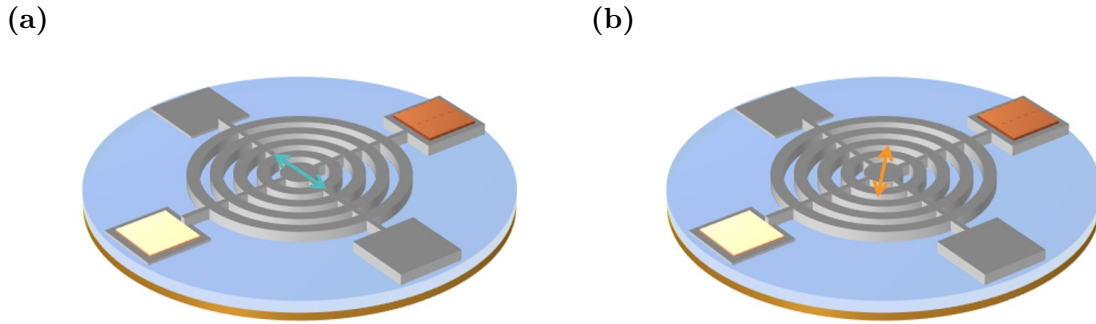


Figure 6.11: Schematic of the two limit cases studied in our simulations. The arrows represent the orientation of the dipole source with (a)  $\alpha = 0^\circ$  and (b)  $\alpha = 45^\circ$ .

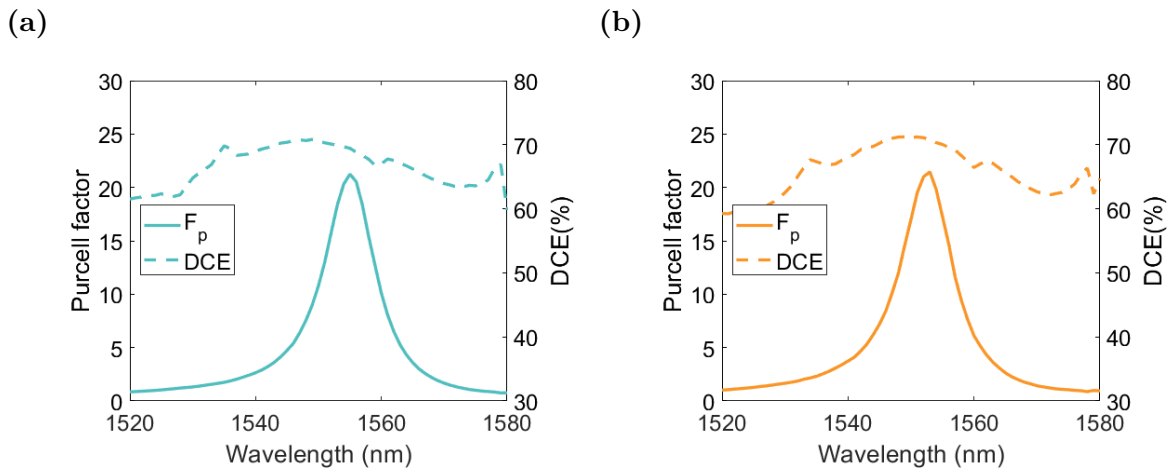


Figure 6.12: Performance of the optimized devices with Purcell factor (solid line) and DCE in  $\text{NA}=0.65$  (dashed line) as a function of wavelength for (a)  $\alpha = 0^\circ$  and (b)  $\alpha = 45^\circ$ .

( $\sim 3$  nm) of the cavity mode. Considering the large bandwidth of the device, this does not appear to be an obstacle to the simultaneous enhancement of the X and XX transitions. Given the typical radiative lifetimes  $\sim 1.5$  ns of the excitonic states in DE InAs/InP QDs [143], these results pave the way for the realization of an efficient and GHz-clocked quantum light source.

To conclude our study, in Figure 6.13a we show that the performance of the CBG are significantly affected by the width of the InP bridges, with a constant descent of both  $F_p$  and DCE for increased  $w_b$ . We attribute this behaviour to a weaker confinement of the cavity mode caused by the intermittent grating. On the other

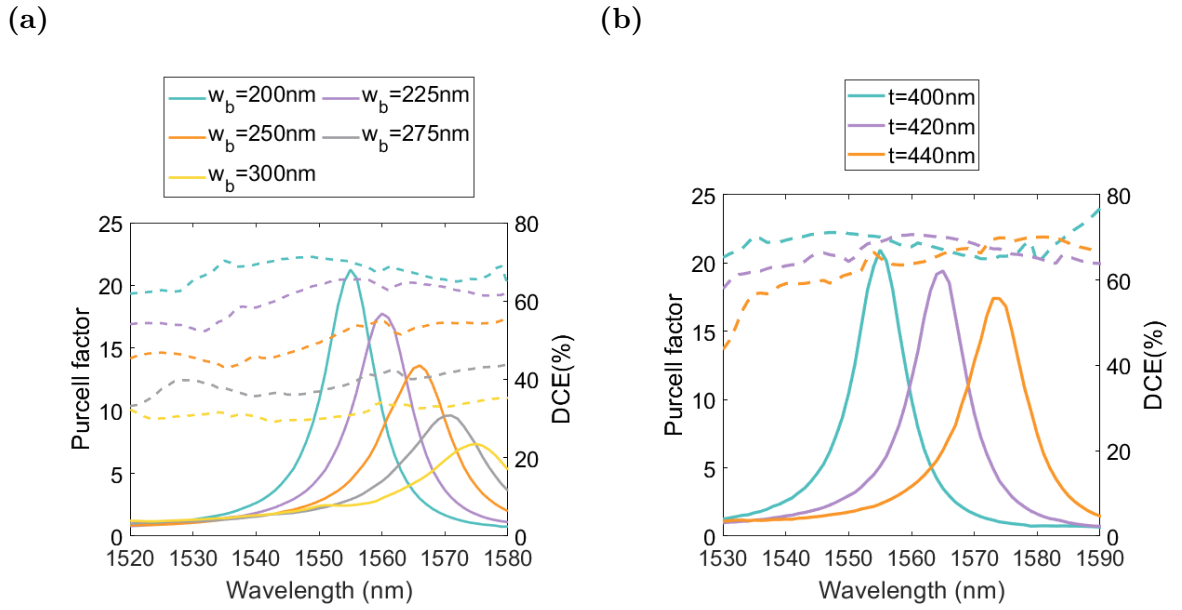


Figure 6.13: (a) Influence of the bridges on the performance of the device: Purcell factor (solid lines) and DCE in  $\text{NA}=0.65$  (dashed lines) as a function of wavelength for five different values of  $w_b$ . (b) Influence of the InP thickness on the performance of the device: Purcell factor (solid lines) and DCE in  $\text{NA}=0.65$  (dashed lines) as a function of wavelength for five different values of  $t_{\text{InP}}$ .

hand, the device shows good tolerance for  $t_{\text{InP}}$ : in fact, increasing the slab thickness by 40 nm leads only to a 20 nm redshift of the cavity mode with small influence on the Purcell factor and maintaining a DCE of 70% around resonance (Figure 6.13b). This robust behaviour, together with the ability to readjust the resonance wavelength with small variations of  $R$  and  $a$ , is essential for the fabrication of an electrically driven CBG which may require an increased slab thickness to avoid degradation of the device performances due to Zn diffusion.

## 6.4 Conclusions

In this chapter we presented a detailed study based on FEM simulations of circular Bragg gratings etched in InP slabs and operating in the telecom C-band. These

devices guarantee efficient extraction of photons emitted by InAs/InP QDs and enable the simultaneous enhancement of the X and XX spectral lines.

First, we optimized the choice of the design parameters to achieve the best combination of Purcell factor, collection efficiency and bandwidth: we reported a DCE in NA=0.65 close to 90% in the whole range 1520 - 1580 nm, together with a cavity mode exhibiting FWHM=16nm and Purcell factor up to 15. We also analyzed the influence of each individual parameter on the optical performances of the device. Then, we determined the optimal strategy for the direct coupling of the emitted photons into four different SM fibres. We showed a maximum MCE of 68.5% in UHNA4 and discussed potential improvements in the device design to achieve an even higher coupling efficiency of 71.7%. Finally, we proposed a modified device design which is directly compatible with electrical carrier injection, reporting Purcell factors up to 20 and a DCE in NA=0.65 close to 70% in the whole telecom C-band. The absence of particularly demanding features that may be challenging to fabricate is a further advantage of our design compared to previous proposals. Our results may benefit the development of highly efficient electrically driven semiconductor quantum light sources and their integration with existing fiber networks for long-distance quantum communication systems.

# 7 | Summary and future work

This dissertation describes the experimental work towards the development of efficient quantum light sources with potential applications in quantum information and cryptography. In particular, we have studied InAs quantum dots, which seem particularly attractive for the generation of single photons and entangled photon pairs. Since those emitters suffer from relatively low efficiency, meaning that achieving sufficient signal intensities for applications has sometimes proven challenging, we have investigated different platforms such as one-dimensional DBR microcavities and circular Bragg gratings that have the potential to enhance their light output.

The main conclusions of each chapter and the prospects for future work are summarized below:

- **Chapter 4 - Cavity-enhanced InAs QDs grown by droplet epitaxy on vicinal GaAs(111)A**

In this chapter we reported the integration of telecom-wavelength InAs droplet epitaxy QDs within a DBR microcavity grown on a vicinal GaAs(111)A. Employing a  $2^\circ$  miscut allowed us to increase the growth rates by approximately one order of magnitude and reduced the propensity of twin defects in the AlGaAs layers. We demonstrated that the presence of the optical microcavity can produce an enhancement of the brightness by a factor  $> 5$  in the telecom O-band together with a remarkable reduction in the density of lines and background, facilitating the spectroscopic investigation of single dots. Moreover, the natural  $C_{3v}$  symmetry on the (111)-oriented substrate is supposed to promote the formation of highly-symmetrical QDs. Nevertheless, measuring the fine-structure splitting over multiple spectral lines produced values similar to the ones reported in literature for DE QDs grown on GaAs(100) substrates. In fact, a deeper analysis revealed that the presence of a  $2^\circ$  miscut breaks

the  $C_{3v}$  symmetry of the system and introduces a privileged direction. Those experimental observations were confirmed by numerical simulations under the framework of the empirical pseudopotential and configuration interaction methods.

In the future, linewidths and FSS could be reduced by changing the composition of the barrier layer from InAlAs to InGaAs and employing a smaller miscut angle respectively. Moreover, it may be beneficial to abandon the thick DBR cavity and focus on the growth of DE QDs in thin semiconductor slabs. This way, the extraction efficiency could be drastically improved by fabricating hybrid circular Bragg gratings. Finally, it would be interesting to exploit the flexibility of the DE technique to push the QD emission towards longer wavelength and reach the telecom C-band.

- **Chapter 5 - Efficient O-band quantum light sources based on circular Bragg gratings**

In this chapter we described the design and characterization of single photon sources in the telecom O-band based on InAs QDs in hybrid circular Bragg gratings. We proved that, even with a non-deterministic fabrication method, the devices are robust against common fabrication issues and could deliver bright and Purcell-enhanced single photon emission.

In order to improve the reproducibility and achieve even higher Purcell factors, it would be desirable to develop a marker-based fabrication technique to optimize the spatial overlap between the QD and the cavity mode. Moreover, the reproducible fabrication of structures compatible with strain-tuning or Stark-tuning would be beneficial for quantum optics experiments with interconnectable sources, such as high-rate interference of indistinguishable photons from remote QDs. Finally, it would be interesting to develop a room-temperature alignment technique for the fabrication of fiber-pigtailed devices, which guarantee permanent and robust coupling for the integration in compact deployable systems to be used outside the laboratory environment.

---

- **Chapter 6 - Design study for C-band quantum light sources based on circular Bragg gratings**

Here, we extended the investigation of hybrid circular Bragg gratings to the telecom C-band, presenting a design optimization for devices fabricated on InP slabs. Furthermore, we determined the optimal strategy for the direct coupling of the emitted photons into four different SM fibres. Finally, we studied an alternative structure that enables electric field control while showing optical properties similar to the original hybrid CBGs. The absence of particularly demanding features that may be challenging to fabricate is a further advantage of our design compared to previous proposals.

The fabrication of the devices presented in this chapter requires the development of a recipe for the InP material system, including the choice of a new material for the sacrificial layer and different chemicals for selective wet etching. Moreover, since high temperatures are usually needed to dry etch InP effectively, ZEP 520A may need to be replaced by a different resist or a hard mask. As for the electrically contacted device, it would be interesting to simulate more advanced geometries where the position of the connections between consecutive rings is shifted to minimize the losses induced by the bridges and achieve even better performance.



# A Single photon emitters in WSe<sub>2</sub> coupled to GaP nano-antennas

This appendix presents the optical characterization of single photon emitters (SPEs) in WSe<sub>2</sub> monolayers coupled to GaP nano-antennas, which provide a positioning site for the SPEs as well as an optical device to enhance the light output and improve the collection efficiency. The data presented here were collected during my visit to Prof. Alexander Tartakovskii's group at the University of Sheffield, with the collaboration and supervision of Luca Sortino and Panaiot Zotev.

## A.1 Introduction

Semiconductor quantum dots integrated in optical cavities are the most mature technology for deterministic single-photon sources and established the current benchmarks for brightness, purity and indistinguishability. However, their large-scale fabrication requires remarkable resources [168], which still poses some challenges to the full scalability and broad diffusion of this approach. In recent years two-dimensional (2D) materials have emerged as a promising alternative, since a simple scotch-tape exfoliation can yield high-quality samples with unique photonic and optoelectronic properties [169]. In particular, transition metal dichalcogenides (TMD) monolayers attracted a special interest due to their strong spin-orbit coupling, large exciton binding energy, and direct bandgap in the visible region [170].

Between TMDs, WSe<sub>2</sub> has been extensively studied since, at low temperature, it can deliver single photons under optical [171, 172, 173] or electrical [174, 175] excitation. The origin of such emission has been attributed to a quantum dot-like

confinement of excitons down to tens of nanometers and recent research demonstrated the possibility of tailoring its properties exploiting external electric and magnetic fields [176] as well as mechanical strain [177, 178]. Moreover, WSe<sub>2</sub> can be efficiently coupled to a broad range of microcavities and devices such as photonic crystals and circular Bragg gratings in order to enhance the quantum light output [179, 180, 181]. Those structures exploit the Purcell effect to increase the spontaneous emission rate of the source, by confining the electromagnetic energy in a diffraction-limited mode volume  $V_{\text{eff}} > (\lambda/n)^3$  with selectivity measured by the quality factor  $Q$ . Since such a  $V_{\text{eff}}$  is relatively large, remarkable Purcell factors can be achieved only for high values of  $Q$ , which affects the bandwidth of the devices.

Alternatively, plasmonics offers the possibility to confine light to subwavelength scales with the use of metallic particles and nano-cavities, leading to a Purcell enhancement comparable to the one guaranteed by photonic structures with much lower  $Q$ . Remarkable enhancements of the PL emission have been demonstrated by coupling WSe<sub>2</sub> to plasmonic structures [182], however the losses caused by absorption in the metal constitute an issue for the development of hybrid TMD-plasmonic devices. For this reason, high-index dielectrics have recently emerged as a substitute of plasmonic materials to design resonators and optical nano-antennas with low losses, combining the advantages of plasmonic systems to interact with quantum emitters and of dielectric cavities to manipulate radiative optical modes without introducing nonradiative decay channels [183].

In this appendix we show that transferring a WSe<sub>2</sub> monolayer onto GaP nano-antennas induces the formation of localized SPEs at cryogenic temperature, with bright photoluminescence intensity enhanced by the coupling to the optical modes of the device. We report PL count rates up to 30 kHz, more than one order of magnitudes brighter than those measured on plasmonic nano-structures [184], and identify two different types of SPEs: the first one exhibits a single emission line characterized by fine structure splitting (FSS) and long radiative lifetimes, while the second one reveals a plurality of satellite peaks at longer wavelength, with the same polarization axis and zero FSS. Finally, we report an evaluation of the first order

correlation function  $g^{(1)}(\tau)$  and the power dependent dephasing time by measuring the fringe contrast in a Mach-Zehnder interferometer.

## A.2 Methods

This section contains a brief description of the additional experimental methods employed for the investigation of single photon emitters in WSe<sub>2</sub>.

### A.2.1 Device design

The nano-antennas investigated in this work were designed by Sandro Mignuzzi from Imperial College London. Figure A.1 shows a schematic view of a device (dimer), which consist of a couple of identical pillars defined on a GaP substrate ( $n = 3.2$ ) with etch depth  $h = 200$  nm. The other relevant parameters are the radius  $r$  of each pillar, and the gap  $g$  between them. For small values of the gap  $g \sim 50$  nm, the dimers support an optical mode with enhanced near-field intensity localized around the edges of the pillars, as reported in Figure A.1a. This mode extends into the visible and near-infrared spectral ranges and is characterized by a low  $Q \sim 10$ . Choosing values of  $r$  between 100 and 500 nm leads to a spectral response centered around 750 nm, which is the typical emission wavelength of WSe<sub>2</sub> monolayers [185]. When an emitter is coupled to such a mode, it can experience an enhanced spontaneous emission rate due to the Purcell effect. Typical Purcell factors for these structures may vary between 5 and 15, depending on the radius of the pillars (Figure A.1b). Meanwhile part of the emitted photons are directed vertically, increasing the amount of radiation that can be collected by a microscope objective (Figure A.1c). Even if the majority of the emission is still trapped in GaP due to the high refractive index contrast at the interface with air, this enhanced directivity constitutes a remarkable improvement compared to bare GaP [186], where less than 1% of the emitted photons can escape from the substrate.

The devices studied in this work were fabricated by Javier Cambiasso from Imperial College London using electron-beam lithography followed by several wet and dry

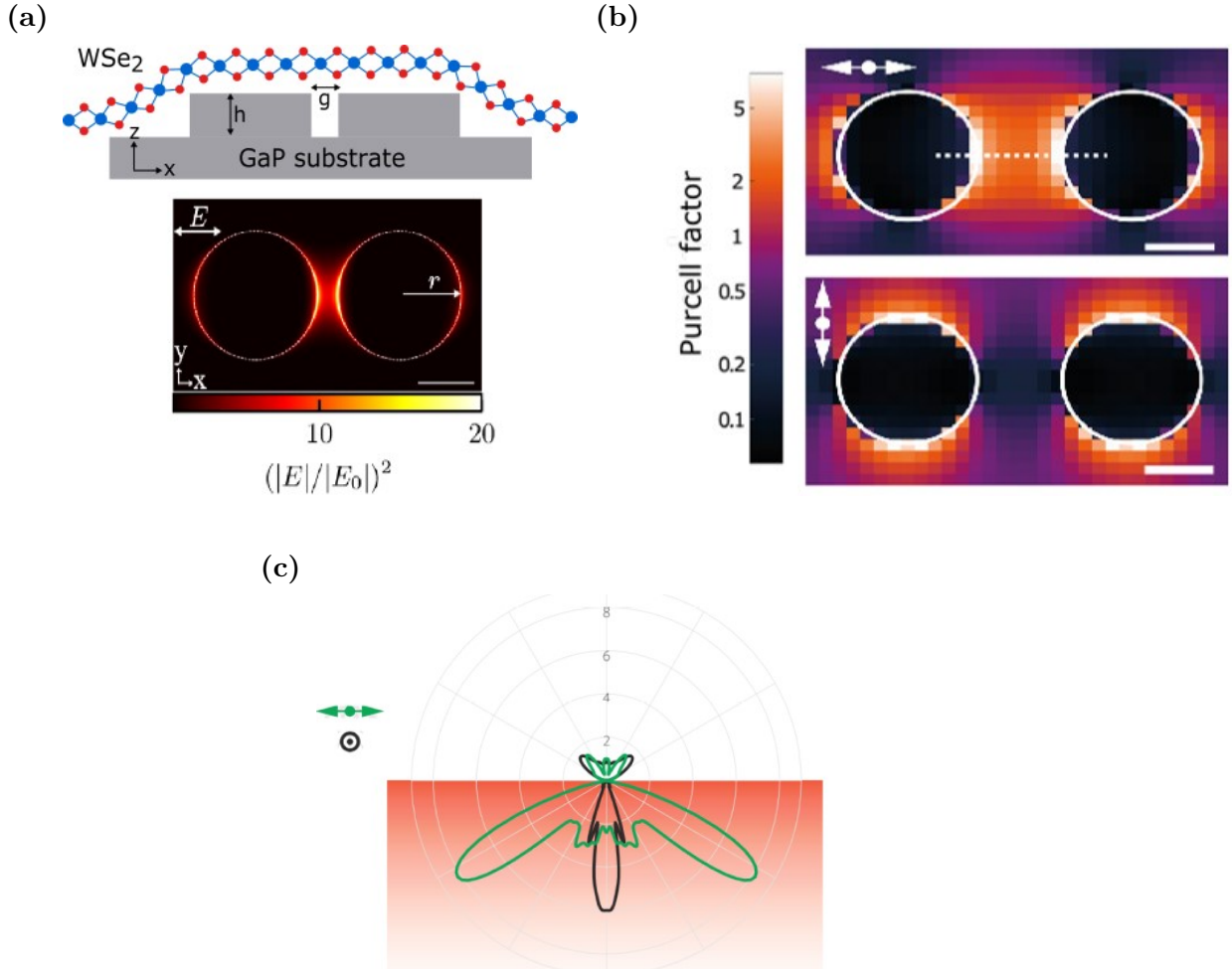


Figure A.1: (a) Schematic of a WSe<sub>2</sub> monolayer placed on a GaP nano-antenna and simulated near-field distribution calculated for a GaP dimer nano-antenna (height 200 nm, radius 50 nm, gap 65 nm) illuminated with a normally incident plane wave. The electric field amplitude  $E$  is normalised by the amplitude  $E_0$  of the incident wave. (b) Simulated Purcell factor for a dipole source placed at different positions over the dimer, with orientation parallel and perpendicular to axis of the device. (c) Associated radiation pattern for an in-plane and out-of-plane dipole source placed in the middle of the gap  $g$  at  $z = 200$  nm. The three plots in this Figure are taken from Ref. [185].

etching steps [187]. An atomically thin layer of WSe<sub>2</sub> was then placed onto an array of GaP dimers with variable radius (50 - 300 nm) by Luca Sortino and Panaiot Zotev, as described in Section A.2.2. After the transfer the monolayer stretches and follows the shape of the underlying device, which guarantees an optimal spatial overlap with the supported optical mode.

### A.2.2 Exfoliation and transfer of WSe<sub>2</sub> monolayers

The sample used in these experiments was produced by mechanical exfoliation of commercially available WSe<sub>2</sub> bulk crystals and then transferred onto a pre-patterned GaP (100) substrate by Luca Sortino and Panaiot Zotev at the University of Sheffield. The fundamental steps of the exfoliation procedure, also known as "scotch-tape method" [188], are shown in Figure A.2. First, a bulk crystal of WSe<sub>2</sub> is placed onto an adhesive tape and covered with a protective PET film. After applying a gentle pressure to improve the adhesion, the crystal is carefully removed leaving just a few layers of WSe<sub>2</sub> on the tape. This exfoliation is then repeated a few more times with fresh tape in order to break the interlayer bonding in the leftover material and obtain even thinner residuals. Then, the tape is pressed on a target substrate (in our case a 1x1 cm PDMS film on a glass slide) and pulled off to transfer the residual flakes, which can be examined under the microscope to identify the monolayers.

The identification of the monolayers was carried out by illuminating the sample with the white light source of a commercial optical microscope. In order to distinguish the PL signal coming from the WSe<sub>2</sub> monolayers, which is peaked around 750 nm, two optical filters were added to the setup: a 550 nm shortpass filter in the excitation path after the white light source and 600 nm longpass filter in the collection path, before the CCD camera of the microscope. Because of their high quantum efficiency at room temperature, under the conditions described above the WSe<sub>2</sub> monolayers could be immediately identified from their bright yellow PL emission. The yellow colour is an artefact caused by the filter placed in the collection path.

Finally, the identified monolayers can be deterministically placed on top of the target substrate. In our case that was a GaP chip with pre-etched optical nano-

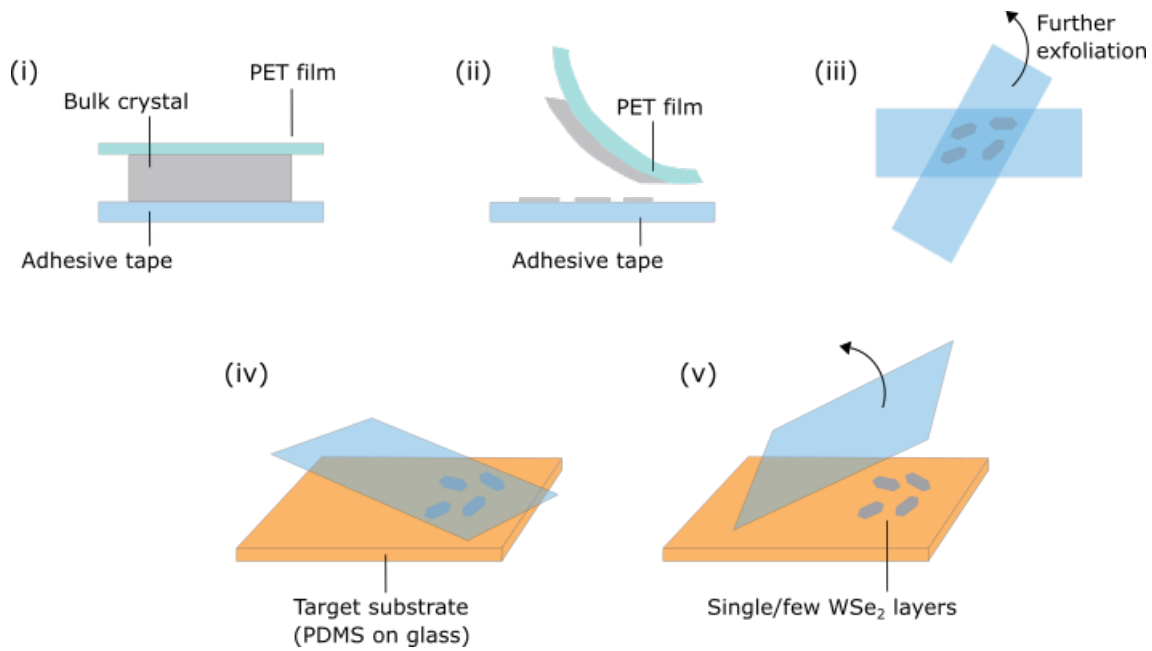


Figure A.2: Schematic of the scotch-tape method: (i) The WSe<sub>2</sub> bulk crystal is placed on the adhesive tape. A gentle pressure with the help of a protective PET film ensures good adhesion. (ii) When the crystal is removed, the adhesion forces break some of the weak interlayer bonds in WSe<sub>2</sub>, leaving a few crystal layers on the tape. (iii) The exfoliation is repeated a few more times with fresh tape to end up with even thinner residuals. (iv) The tape with the remaining material is pressed on a target substrate. (v) The tape is pulled off, leaving some WSe<sub>2</sub> flakes on the PDMS film, ready to be examined under the optical microscope.

antennas. The procedure chosen for the transfer relies on the visco-elastic properties of PDMS [189], which behaves as an elastic solid over short timescales but can slowly flow over long timescales [190]. The exfoliated monolayer is aligned to the target region with the help of a micro-manipulator and pressed against the substrate. Then the PDMS is peeled off very slowly in order to release the WSe<sub>2</sub> flakes. By slowly peeling off the stamp from the surface, the visco-elastic material detaches, releasing the flakes that remain attached to the target substrate.

### A.2.3 PL measurements

The micro-PL measurements presented in this appendix have been carried out using a setup assembled at the University of Sheffield by Luca Sortino. The general structure of the setup is similar to the one represented in Figure 3.10, but in this case the sample was mounted onto stepper motor stages in a bath cryostat and excited with either a CW laser diode at 685 nm or a pulsed laser diode at 638 nm (pulse width  $\sim 90$  ps) through an infinity corrected objective with NA=0.7. The collected light was first coupled into a spectrometer containing two gratings (300 and 1800 grooves/mm respectively) and then sent to a CCD sensor for detection. For time-resolved measurements, the photons belonging to the transition of interest were recorded with an avalanche photodiode (APD) operating near the reverse breakdown voltage.

### A.2.4 First order correlation function measurements

In order to evaluate the first order correlation function  $g^{(1)}(\tau)$  of single-photon emitters in WSe<sub>2</sub> monolayers, we employed the setup represented in Figure A.3. Here, the PL signal filtered by the monochromator is coupled into a fibre Mach-Zehnder interferometer with a phase shifter in one arm and a motorized translation stage in the other arm [191]. The fiber phase shifter is controlled by a voltage generator and produces a phase difference  $\Delta\phi$  to measure the fringe contrast, whereas a motorised translation stage controls the variable optical delay ( $\Delta t$ ) between the two arms. For each value of  $\Delta t$ , the phase difference is scanned by applying a variable voltage to the phase shifter while the output intensity is detected by an APD and recorded electronically by a photon counter. After measuring the interference fringes, the fringe contrast visibility  $v$  is calculated as:

$$v = \frac{I_{\max} - I_{\min}}{I_{\max} + I_{\min}} \quad (\text{A.1})$$

where  $I_{\max}$  and  $I_{\min}$  are the average values of the local maxima and minima.

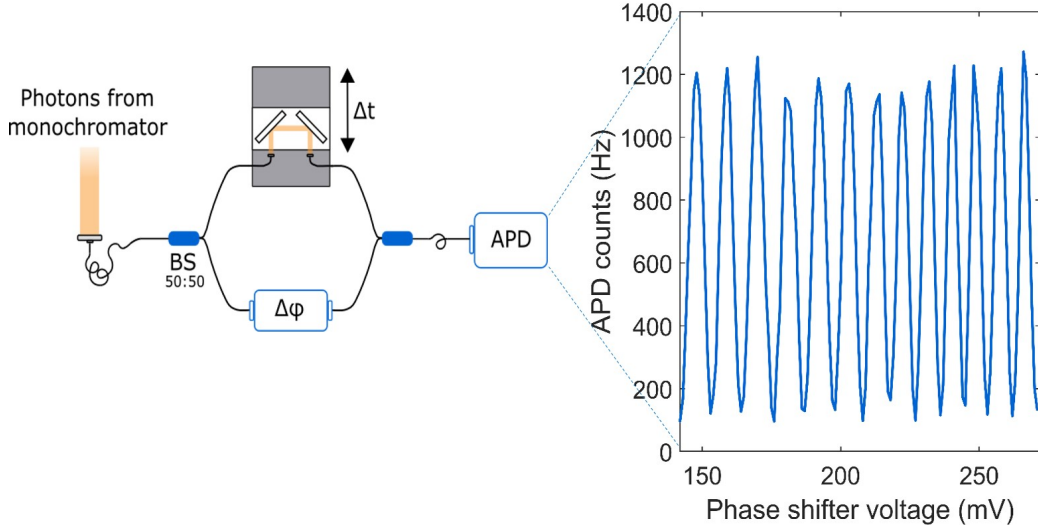


Figure A.3: Schematic of the fiber Mach-Zehnder interferometer employed to measure the first order correlation function  $g^{(1)}(\tau)$  and example of fringes recorded by the photon counter by changing the voltage applied to the fiber phase shifter at  $\Delta t = 0$ .

This procedure is repeated for increasing values of  $\Delta t$ , until the fringes can no longer be observed. As demonstrated in [191], the relationship between the measured fringe contrast visibility and  $g^{(1)}(\tau)$  is given by:

$$g^{(1)}(\tau) = (1 - \epsilon) \frac{|g^{(1)}(\tau)|}{g^{(1)}(0)} \quad (\text{A.2})$$

where  $(1 - \epsilon)$  is the maximum resolvable fringe contrast of the interferometer, which in our case was limited to 0.98.

## A.3 Experimental results

### A.3.1 Micro-PL measurements

In Figure A.4a we report the low-temperature PL emission of a WSe<sub>2</sub> placed on top of a GaP dimer with radius  $r = 300$  nm. The PL signal is recorded at a temperature of 4 K under above-band pulsed laser excitation at 80 MHz. The spectrum is characterized by the presence of a bright isolated peak (labelled "main") at  $\lambda = 745$  nm, exhibiting count rates up to 30 kHz and a linewidth of  $410 \mu\text{eV}$  (Figure A.4b).

We also observe a series of secondary peaks at longer wavelength (labelled "satellite"), which sit on top of a broader background. This spectral structure, which is coherent with previous observations of quantum emitters in WSe<sub>2</sub> monolayers [171], appears extremely stable over weeks at cryogenic temperature. The PL emission shows a small spectral wandering over a long time scale (Figure A.4c), which we attribute to charge or electric field fluctuations in the neighbourhood of the emitter. To investigate the nature of the photon emission, we spectrally selected the main peak and measured the photon statistics using Hanbury-Brown-Twiss interferometry, as explained in Section 3.12. The corresponding diagram of photon coincidences (Figure A.4d) shows a pronounced sign of anti-bunching, with reduced coincidences at zero delay time indicating single photon emission. The high value of  $g^{(2)}(0) = 0.46$  recorded in our experiment can be explained by the presence of residual background from 2D excitons causing undesired multi-photon events. It is worth noting that lower values of  $g^{(2)}(0)$  down to 0.26 have been reported for the same class of emitters [192]. According to previous observations, we attribute the single photon emission to the formation of excitonic complexes associated with the local strain experienced by the WSe<sub>2</sub> monolayer [193], which folds around the edges of the underlying nano-pillars.

Moreover, we analysed the power dependence of the PL response under optical excitation at 638 nm and 80 MHz repetition rate. In fact, a saturation of the PL intensity is expected for single quantum emitters, since the maximum number of emitted single photons is limited by the lifetime of the excited state. This leads to a nonlinear dependence of the integrated PL intensity ( $I$ ) with respect to the optical excitation power ( $P$ ) described by the equation:

$$I = I_{\text{sat}} \frac{P}{P + P_0} \quad (\text{A.3})$$

where  $I_{\text{sat}}$  is the integrated PL intensity at saturation and  $P_0$  is the normalized power value, i.e. the excitation power such that  $I(P_0) = \frac{1}{2}I_{\text{sat}}$ .

As reported in Figure A.5, both the main and the satellite peak at  $\lambda=752$  nm follow the expected saturation behaviour with similar values of  $P_0$  around 50 nW. Repeating this analysis over the other satellite peaks confirms that  $P_0$  can change slightly but saturation is always observed.

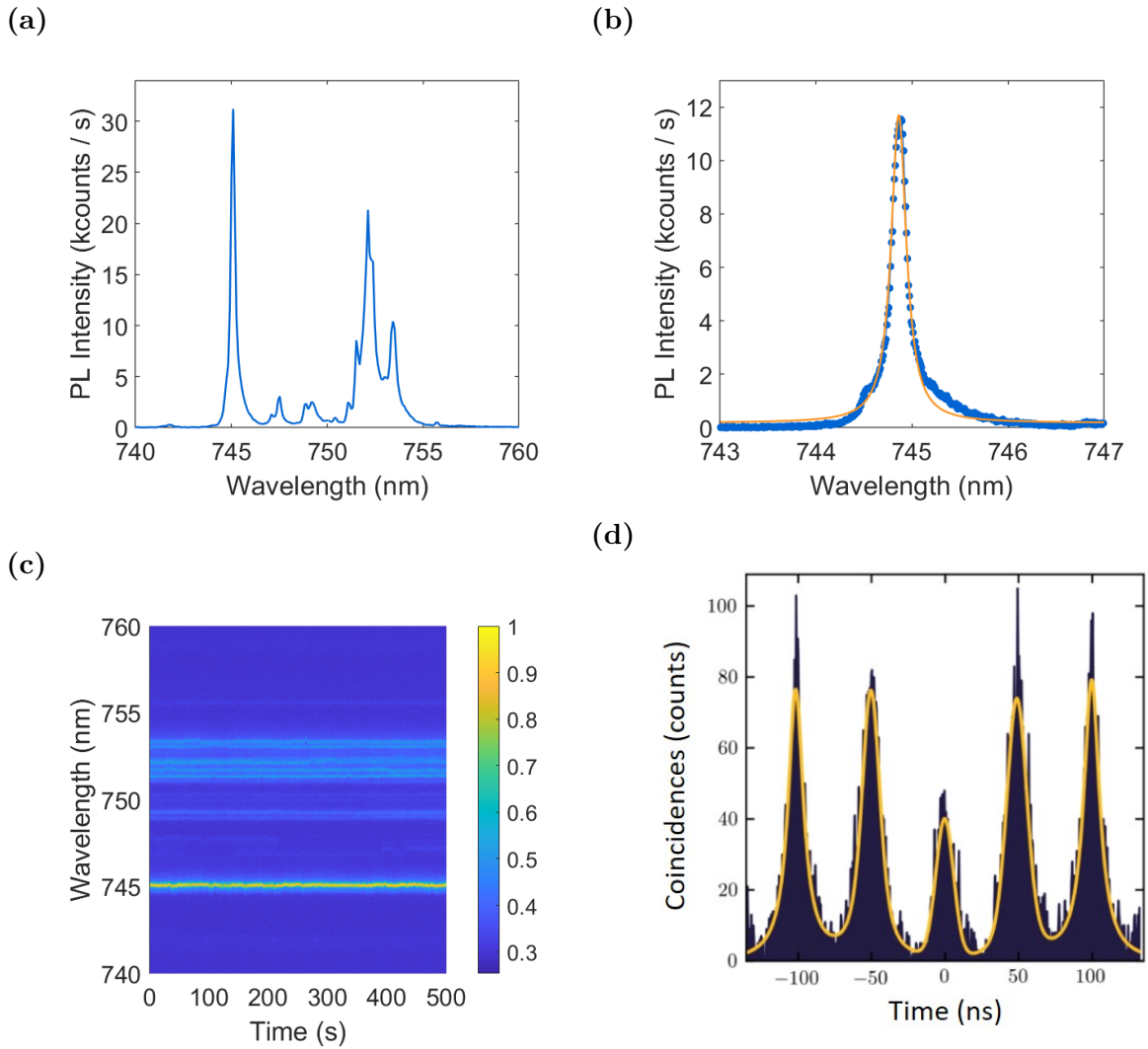


Figure A.4: (a) Low-temperature photoluminescence emission of a strained WSe<sub>2</sub> monolayer on top of a GaP nano-antenna ( $r = 300$  nm) under pulsed laser excitation at 80MHz ( $\lambda=638$  nm), exhibiting a main emission peak at  $\lambda=745$  nm and a series of satellite peaks at longer wavelength. (b) Main emission peak fitted with a Lorentzian function (solid line), showing a linewidth of  $410 \mu\text{eV}$ . (c) Corresponding spectral wandering showing a stable spectral emission over 500 s for both the main and the satellite peaks. (d) Second order photon correlation measured on the main emission peak at  $\lambda=745$  nm under pulsed excitation at 80 MHz, with reduced coincidences at zero delay time indicating single photon emission.

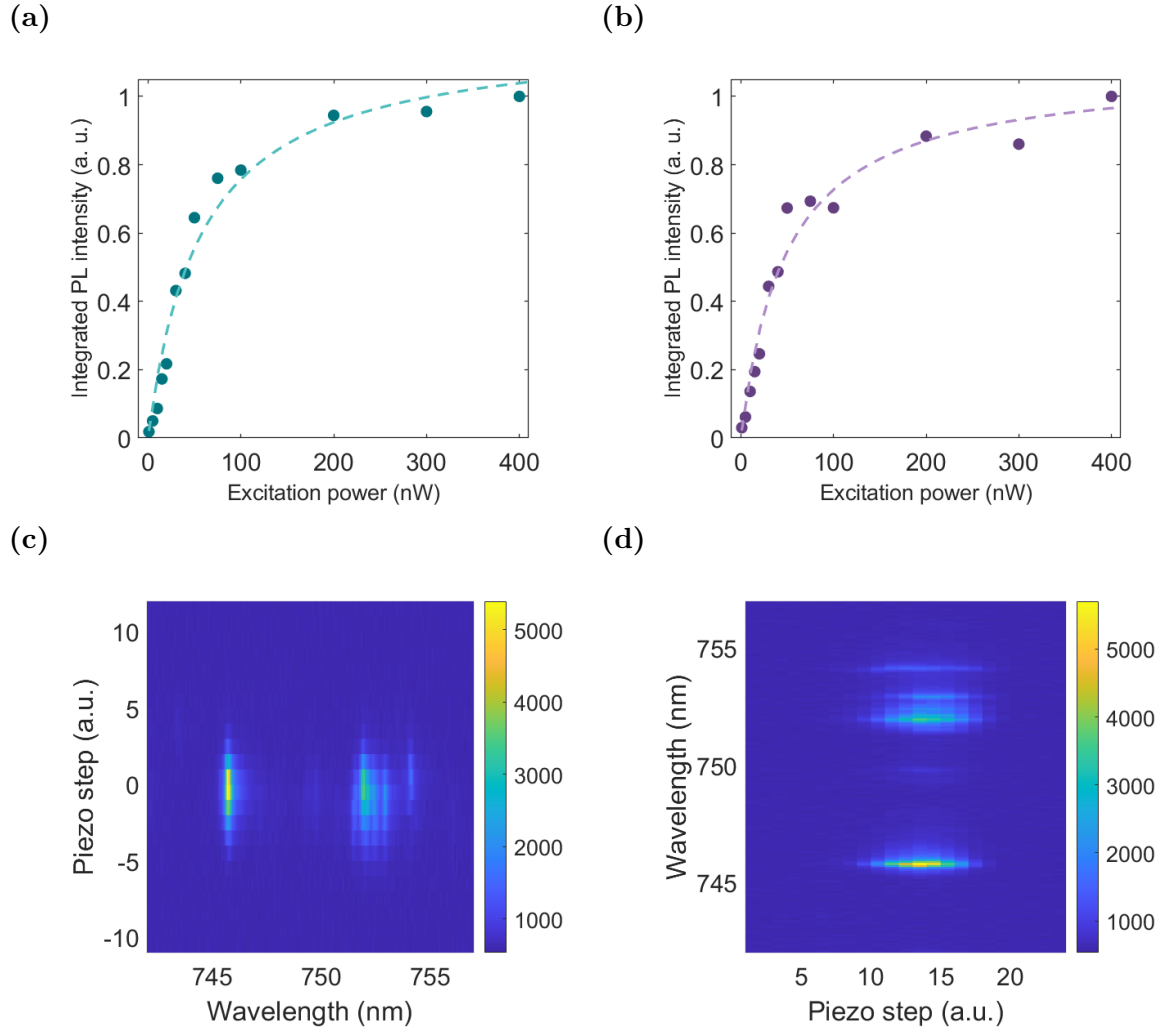


Figure A.5: (a) Integrated intensity versus excitation power for the main emission peak at  $\lambda=745$  nm. The dashed lines represent the fit with Equation A.3, with  $P_0 = 56$  nW. (b) Integrated intensity versus excitation power for the satellite peak at  $\lambda=752$  nm. The dashed lines represent the fit with Equation A.3, with  $P_0 = 47$  nW. (c) Vertical PL scan (i.e. perpendicular to the axis connecting the nano-pillars) measured across the dimer position to demonstrate the localization of the SPE. (d) Horizontal PL scan (i.e. along the axis connecting the nano-pillars) measured across the dimer position.

Next, in order to demonstrate that the GaP nano-antennas provide a deterministic positioning site for the SPEs, we performed two perpendicular linear scans by moving the excitation and collection spots across the position of the dimer and recording the corresponding PL spectra. As reported in Figure A.5, the PL signal is maximized for positions close to the centre of the device, while it vanishes when we move away from the pillars. Unfortunately, the spatial resolution of this method does not allow us to investigate in which area of the device the emission originates, but the correlation between the PL intensity and the position of the dimer is a clear indication of the deterministic localization of the SPE. We also observe that the PL emission of the main and the satellite peaks is maximized for slightly different positions along the horizontal direction (Figure A.5d), suggesting that multiple emitters contribute to the complex spectral structure in Figure A.4a. In fact, excitons can be trapped in multiple potential wells, which form in the WSe<sub>2</sub> monolayer when it folds around the edges of the nano-pillars, experiencing a different local strain. However, testing this hypothesis would require a spatial resolution much higher than the one provided by the experimental setup used.

### A.3.2 Polarization-resolved spectroscopy

To gain further insight into the nature of the emission centre described in Figure A.4, we performed polarization resolved PL measurements, where the sample is excited with a linearly polarized pulsed laser while a rotating half-wave plate and a linear polarizer are included in the collection arm. As reported in Figure A.6, the main emission peak at  $\lambda=744.7$  nm is accompanied by a secondary peak at shorter wavelength (Figure A.6a), energetically separated by  $\sim 700$   $\mu\text{eV}$ . The intensity ratio between the two peaks is  $\sim 6$  under above-band excitation and the degree of linear polarization is 74% and 87% respectively. The existence of states with high degree of linear polarization can be explained by the presence of aligned strain, which breaks the honeycomb crystal structure of the monolayer along a particular direction. The resulting reduced symmetry gives rise to the high linear polarization of strain-trapped excitons [194]. Overall, the observed polarization characteristics are coherent with

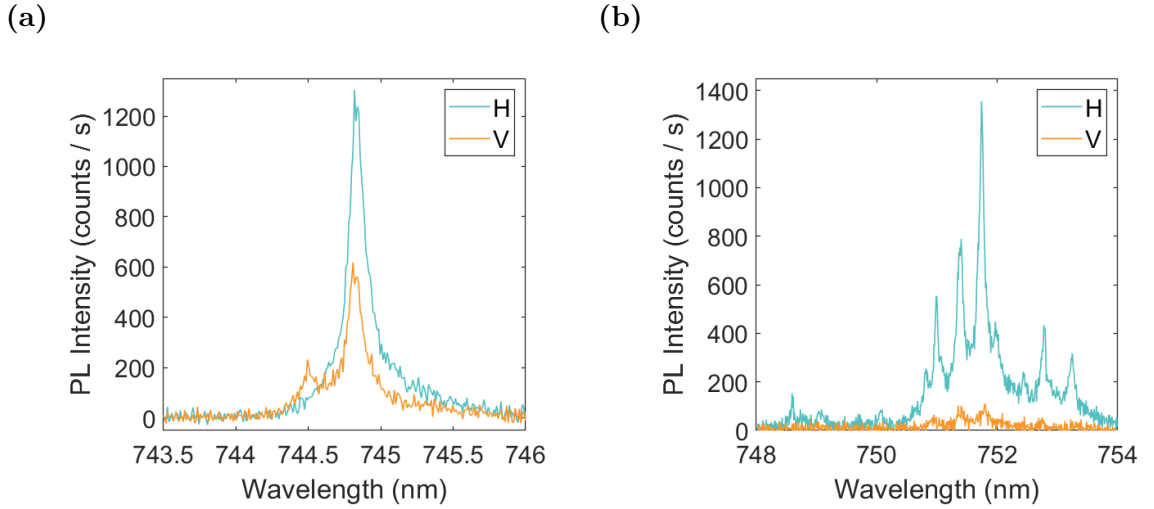


Figure A.6: (a) Polarization resolved PL spectra of the main emission peak, revealing a doublet with a fine structure splitting of  $\sim 700 \mu\text{eV}$  and intensity ratio  $\sim 6$ . (b) Polarization resolved PL spectra of the satellite peaks, which show no evidence of fine structure splitting.

previous results [195], although the relevant literature shows an extensive variety in the polarization properties of PL peaks from strain-trapped excitons in  $\text{WSe}_2$ . Such a variety supports the idea that the different strain conditions experienced by the monolayer must influence the shape of the trapping potential as reported in [196], where directional elongations of the potential well were achieved by changing the gap of the nanostructure underneath the  $\text{WSe}_2$ . On the other hand, all the satellite peaks are linearly polarized along the same axis, without showing any sign of fine structure splitting. Together with the linear scan in Figure A.5d, this supports the hypothesis that the main and the satellite peaks are not associated to the same potential well. Instead, the satellite peaks could originate from a second well, which forms in a slightly different area of the device and can host a larger number of quantum states because of the different mechanical strain experienced.

### A.3.3 Emission dynamics

To conclude the characterization of the emitter described above, we focussed on the temporal evolution of the excited states and studied the photoluminescence

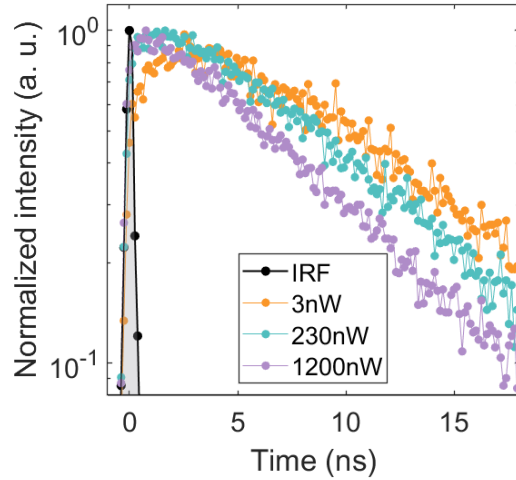


Figure A.7: Photoluminescence decay traces of the main emission peak measured under above-band excitation for three different values of the pump power: below, around and above  $P_0$ .

dynamics of the main emission peak using time-resolved spectroscopy, as described in Section 3.4.2. In general, the emission dynamics of SPEs in WSe<sub>2</sub> is not yet fully understood because it can be extremely variable: in fact, the literature includes reports of both very long (225 ns) and very short (2 ps) lifetimes [197]. In Figure A.7 we report the luminescence decay trace measured on the main peak as a function of the excitation power and we observe the presence of a clearly resolvable rise time. In order to capture the combined growth and decay behaviour, we define the decay time constant  $\tau_d$  and the onset time  $\tau_0$  as the time where the exponential decay starts. We notice a strong power dependence in the rise of the luminescence trace with a reduction of  $\tau_0$  from 2.5 ns at 1 nW to 0.9 ns at 1  $\mu$ W, suggesting a more efficient capture of the excitonic complex into the strain-induced potential well for increasing laser excitation. The effect of the pump power is visible also on the decay trace, with  $\tau_d$  varying from 9.7 ns at 1 nW to 7.3 ns at 1  $\mu$ W. This is coherent with previous observations [198] and can be explained by the increasing probability of non-radiative recombination mechanisms, such as diffusion-assisted exciton-exciton annihilation.

### A.3.4 Coherence of a strain-induced single-photon emitter

To conclude our study of SPEs in WSe<sub>2</sub>, we evaluate the first order correlation function  $g^{(1)}(\tau)$  for a different emitter localized on a GaP nano-antennas of radius  $r = 200$  nm. As described in Section A.2.4, we employ a Mach-Zehnder interferometer with a phase shifter in one arm and a motorized delay line in the other arm.

Figure A.8 shows the PL emission of the SPE considered, with a main isolated emission line at  $\lambda=752$  nm exhibiting FWHM = 450  $\mu$ eV and  $P_0 = 72$  nW. In Figure A.8d we report the measured fringe contrast visibility  $v(\tau)$  for three different values of the excitation power: below, around and above  $P_0$  respectively. The decay of the fringe contrast is fitted with the function:

$$g^{(1)}(\tau) = e^{(-\tau/T_2)} \quad (\text{A.4})$$

from which we extract the coherence time  $T_2$ .

We observe that the longest coherence time  $T_2 = 2.78 \pm 0.14$  ps is obtained with the lowest excitation power of 25 nW. It is worth noting that the 450  $\mu$ eV linewidth of the transition investigated, which is a typical value for SPEs in WSe<sub>2</sub>, limits the coherence time to:

$$T_2 = \frac{2\hbar}{FWHM} = 2.9ps \quad (\text{A.5})$$

This indicates that the rapid dephasing determined by electron-phonon interactions [199] is still the main limiting factor for the coherence time of this class of emitters.

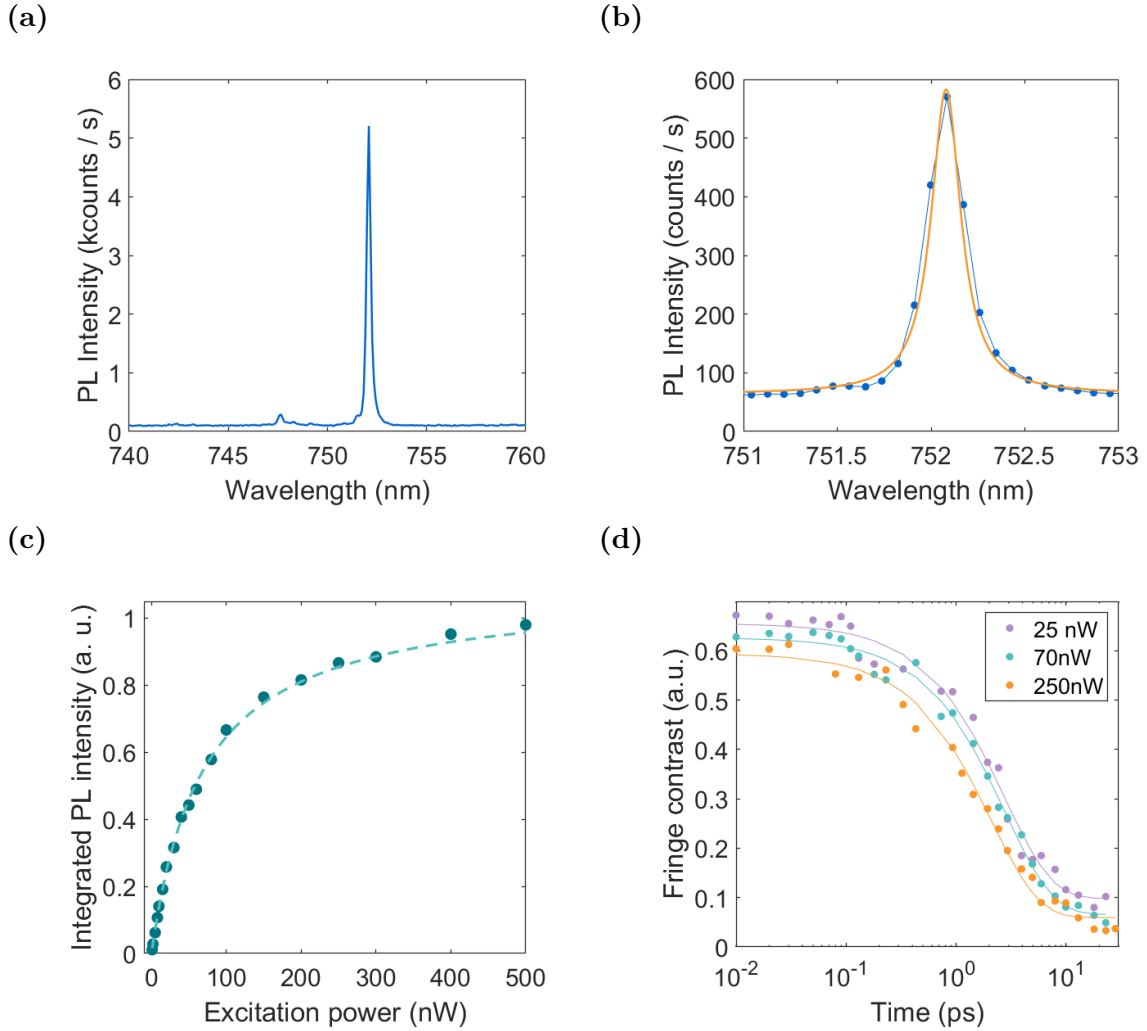


Figure A.8: (a) Low-temperature PL signal from a WSe<sub>2</sub> SPE localized on a GaP nano-antennas of radius  $r = 200$  nm. (b) Lorentzian fit of the emission peak, showing a linewidth of  $450 \mu\text{eV}$ . (c) Integrated PL intensity as a function of the excitation laser power. (d) Fringe contrast visibility  $v(\tau)$  measured under above-band excitation at 638 nm for three different values of the excitation power.

## A.4 Conclusions

In this chapter we presented a detailed characterization of SPEs in WSe<sub>2</sub> coupled to GaP nano-antennas. First, we demonstrated that the dimers provide a deterministic positioning site for strain-induced SPEs as well as an optical device to enhance the light output and improve the collection efficiency. We reported bright photoluminescence emission and observed the presence of two different classes of emitters with well defined optical properties in the PL spectra. The first class appears at shorter wavelength as an isolated peak and is characterized by the presence of a FSS doublet, while the second one consists of a set of peaks at longer wavelength without any sign of FSS. The origin of those emitters can be explained by the excitonic confinement in strain-induced potential wells. We also reported a direct measurement of the first order correlation function for a SPE coupled to a GaP dimer, extracting a coherence time of  $T_2 = 2.78$  ps, which appears to be mainly limited by pure dephasing.

Although more detailed measurements would be necessary, the preliminary data suggest that GaP nano-antennas are a powerful platform to enhance the light output of single-photon emitters in 2D semiconductors. In terms of future work, developing a flip-chip fabrication process for the integration of a backside broad-band reflective mirror may considerably improve the brightness by redirecting towards the collection optics the majority of the photons currently absorbed in the GaP substrate.



# Bibliography

- [1] W. Stallings, *Cryptography and network security: principles and practice*. Boston: Pearson, 7<sup>th</sup> ed., 2014.
- [2] C. H. Bennett and G. Brassard, “Quantum cryptography: public key distribution and coin tossing,” *Theoretical Computer Science*, vol. 560, pp. 7–11, 2014.
- [3] S. Pirandola, U. L. Andersen, L. Banchi, M. Berta, D. Bunandar, R. Colbeck, D. Englund, T. Gehring, C. Lupo, C. Ottaviani, J. L. Pereira, M. Razavi, J. Shamsul Shaari, M. Tomamichel, V. C. Usenko, G. Vallone, P. Villoresi, and P. Wallden, “Advances in quantum cryptography,” *Advances in Optics and Photonics*, vol. 12, no. 4, p. 1012, 2020.
- [4] N. Gisin, G. Ribordy, W. Tittel, and H. Zbinden, “Quantum cryptography,” *Reviews of Modern Physics*, vol. 74, no. 1, pp. 145–195, 2002.
- [5] H. S. Singh, D. Gupta, and A. K. Singh, “Quantum key distribution protocols: a review,” *IOSR Journal of Computer Engineering*, vol. 16, pp. 1–9, 2014.
- [6] A. K. Ekert, “Quantum cryptography based on Bell’s theorem,” *Physical Review Letters*, vol. 67, no. 6, pp. 661–663, 1991.
- [7] N. Lütkenhaus, “Security against individual attacks for realistic quantum key distribution,” *Physical Review A*, vol. 61, no. 5, p. 78, 2000.
- [8] N. Lütkenhaus and M. Jahma, “Quantum key distribution with realistic states: photon-number statistics in the photon-number splitting attack,” *Optics Letters*, vol. 4, p. 44, 2002.

- [9] D. A. Vajner, L. Rickert, T. Gao, K. Kaymazlar, and T. Heindel, “Quantum communication using semiconductor quantum dots,” *Advanced Quantum Technologies*, vol. 5, no. 7, p. 2100116, 2022.
- [10] X. B. Wang, “Beating the photon-number-splitting attack in practical quantum cryptography,” *Physical Review Letters*, vol. 94, no. 23, p. 230503, 2005.
- [11] B. C. Jacobs, T. B. Pittman, and J. D. Franson, “Quantum relays and noise suppression using linear optics,” *Physical Review A*, vol. 66, no. 5, p. 46, 2002.
- [12] K. Azuma, K. Tamaki, and H.-K. Lo, “All-photonic quantum repeaters,” *Nature communications*, vol. 6, p. 6787, 2015.
- [13] C. Monroe, “Quantum information processing with atoms and photons,” *Nature*, vol. 416, no. 6877, pp. 238–246, 2002.
- [14] B. Lounis and W. E. Moerner, “Single photons on demand from a single molecule at room temperature,” *Nature*, vol. 407, no. 6803, pp. 491–493, 2000.
- [15] T. M. Babinec, B. J. M. Hausmann, M. Khan, Y. Zhang, J. R. Maze, P. R. Hemmer, and M. Loncar, “A diamond nanowire single-photon source,” *Nature Nanotechnology*, vol. 5, no. 3, pp. 195–199, 2010.
- [16] I. Aharonovich, D. Englund, and M. Toth, “Solid-state single-photon emitters,” *Nature Photonics*, vol. 10, no. 10, pp. 631–641, 2016.
- [17] M. A. Reed, “Spatial quantization in GaAs-AlGaAs multiple quantum dots,” *Journal of Vacuum Science & Technology B: Microelectronics and Nanometer Structures*, vol. 4, no. 1, p. 358, 1986.
- [18] R. C. Ashoori, “Electrons in artificial atoms,” *Nature*, vol. 379, no. 6564, pp. 413–419, 1996.
- [19] P. Michler, *Single Semiconductor Quantum Dots*. Berlin, Heidelberg: Springer Berlin Heidelberg, 2009.

- 
- [20] A. Tartakovskii, *Quantum Dots*. Cambridge University Press, 2012.
- [21] D. Bimberg, M. Grundmann, and N. N. Ledentsov, *Quantum dot heterostructures*. Chichester: J. Wiley, 1999.
- [22] M. Holm, M. E. Pistol, and C. Pryor, “Calculations of the electronic structure of strained InAs quantum dots in InP,” *Journal of Crystal Growth*, vol. 92, no. 2, pp. 932–936, 2002.
- [23] C. Tablero, “Energy levels in self-assembled quantum arbitrarily shaped dots,” *The Journal of chemical physics*, vol. 122, no. 6, p. 064701, 2005.
- [24] R. Heitz, M. Grundmann, N. N. Ledentsov, L. Eeckey, M. Veit, D. Bimberg, V. M. Ustinov, A. Y. Egorov, A. E. Zhukov, P. S. Kop’ev, and Z. I. Alferov, “Multiphonon–relaxation processes in self–organized InAs/GaAs quantum dots,” *Applied Physics Letters*, vol. 68, no. 3, pp. 361–363, 1996.
- [25] A. J. Shields, “Semiconductor quantum light sources,” *Nature Photonics*, vol. 1, p. 215, 2007.
- [26] D. Gammon, E. S. Snow, B. V. Shanabrook, D. S. Katzer, and D. Park, “Fine structure splitting in the optical spectra of single GaAs quantum dots,” *Physical Review Letters*, vol. 76, no. 16, pp. 3005–3008, 1996.
- [27] M. Bayer, G. Ortner, O. Stern, A. Kuther, A. A. Gorbunov, A. Forchel, P. Hawrylak, S. Fafard, K. Hinzer, T. L. Reinecke, S. N. Walck, J. P. Reithmaier, F. Klopff, and F. Schäfer, “Fine structure of neutral and charged excitons in self-assembled In(Ga)As/(Al)GaAs quantum dots,” *Physical Review B*, vol. 65, no. 19, p. 3216, 2002.
- [28] R. Uppu, F. T. Pedersen, Y. Wang, C. T. Olesen, C. Papon, X. Zhou, L. Midolo, S. Scholz, A. D. Wieck, A. Ludwig, and P. Lodahl, “Scalable integrated single-photon source,” *Science advances*, vol. 6, no. 50, 2020.
- [29] R. Uppu, H. T. Eriksen, H. Thyrestrup, A. D. Uğurlu, Y. Wang, S. Scholz, A. D. Wieck, A. Ludwig, M. C. Löbl, R. J. Warburton, P. Lodahl, and L. Midolo,

- “On-chip deterministic operation of quantum dots in dual-mode waveguides for a plug-and-play single-photon source,” *Nature communications*, vol. 11, no. 1, p. 3782, 2020.
- [30] G. Kiršanskė, H. Thyrrerstrup, R. S. Daveau, C. L. Dreeßen, T. Pregnolato, L. Midolo, P. Tighineanu, A. Javadi, S. Stobbe, R. Schott, A. Ludwig, A. D. Wieck, S. I. Park, J. D. Song, A. V. Kuhlmann, I. Söllner, M. C. Löbl, R. J. Warburton, and P. Lodahl, “Indistinguishable and efficient single photons from a quantum dot in a planar nanobeam waveguide,” *Physical Review B*, vol. 96, no. 16, p. 174, 2017.
- [31] J. Skiba-Szymanska, R. M. Stevenson, C. Varnava, M. Felle, J. Huwer, T. Müller, A. J. Bennett, J. P. Lee, I. Farrer, A. B. Krysa, P. Spencer, L. E. Goff, D. A. Ritchie, J. Heffernan, and A. J. Shields, “Universal growth scheme for quantum dots with low fine-structure splitting at various emission wavelengths,” *Physical Review Applied*, vol. 8, no. 1, 2017.
- [32] C. Santori, D. Fattal, J. Vučković, G. S. Solomon, and Y. Yamamoto, “Indistinguishable photons from a single-photon device,” *Nature*, vol. 419, no. 6907, pp. 594–597, 2002.
- [33] E. Moreau, I. Robert, J. M. Gérard, I. Abram, L. Manin, and V. Thierry-Mieg, “Single-mode solid-state single photon source based on isolated quantum dots in pillar microcavities,” *Applied Physics Letters*, vol. 79, no. 18, pp. 2865–2867, 2001.
- [34] N. Tomm, A. Javadi, N. O. Antoniadis, D. Najer, M. C. Löbl, A. R. Korsch, R. Schott, S. R. Valentin, A. D. Wieck, A. Ludwig, and R. J. Warburton, “A bright and fast source of coherent single photons,” *Nature Nanotechnology*, 2021.
- [35] M. A. M. Versteegh, M. E. Reimer, K. D. Jöns, D. Dalacu, P. J. Poole, A. Gulinatti, A. Giudice, and V. Zwiller, “Observation of strongly entangled

- photon pairs from a nanowire quantum dot,” *Nature communications*, vol. 5, p. 5298, 2014.
- [36] K. D. Jöns, L. Schweickert, M. A. M. Versteegh, D. Dalacu, P. J. Poole, A. Gulinatti, A. Giudice, V. Zwiller, and M. E. Reimer, “Bright nanoscale source of deterministic entangled photon pairs violating Bell’s inequality,” *Scientific Reports*, vol. 7, no. 1, p. 1700, 2017.
- [37] M. Gschrey, A. Thoma, P. Schnauber, M. Seifried, R. Schmidt, B. Wohlfeil, L. Krüger, J.-H. Schulze, T. Heindel, S. Burger, F. Schmidt, A. Strittmatter, S. Rodt, and S. Reitzenstein, “Highly indistinguishable photons from deterministic quantum-dot microlenses utilizing three-dimensional in situ electron-beam lithography,” *Nature communications*, vol. 6, no. 1, p. 7662, 2015.
- [38] Y. Chen, M. Zopf, R. Keil, F. Ding, and O. G. Schmidt, “Highly-efficient extraction of entangled photons from quantum dots using a broadband optical antenna,” *Nature communications*, vol. 9, no. 1, p. 2994, 2018.
- [39] A. Kaganskiy, S. Fischbach, A. Strittmatter, T. Heindel, S. Rodt, and S. Reitzenstein, “Enhancing the photon-extraction efficiency of site-controlled quantum dots by deterministically fabricated microlenses,” *Optics Communications*, vol. 413, pp. 162–166, 2018.
- [40] K. J. Vahala, “Optical microcavities,” *Nature*, vol. 424, pp. 839 EP –, 2003.
- [41] P. Lalanne, C. Sauvan, and J. P. Hugonin, “Photon confinement in photonic crystal nanocavities,” *Laser & Photonics Review*, vol. 2, no. 6, pp. 514–526, 2008.
- [42] J. D. Jackson, *Classical electrodynamics*. New York: Wiley, 3rd ed. ed., 1999.
- [43] M. Capek, L. Jelinek, and G. A. E. Vandenbosch, “Stored electromagnetic energy and quality factor of radiating structures,” *Proceedings. Mathematical, physical, and engineering sciences*, vol. 472, no. 2188, p. 20150870, 2016.

- [44] M. Fox, *Quantum optics: An introduction*, vol. 15 of *Oxford master series in physics*. Oxford and New York: Oxford University Press, 2006.
- [45] K. Srinivasan, M. Borselli, O. Painter, A. Stintz, and S. Krishna, “Cavity Q, mode volume, and lasing threshold in small diameter AlGaAs microdisks with embedded quantum dots,” *Optics express*, vol. 14, no. 3, pp. 1094–1105, 2006.
- [46] Y. Yamamoto, F. Tassone, H. Cao, *Semiconductor Cavity Quantum Electrodynamics*, vol. 169. Berlin, Heidelberg: Springer Berlin Heidelberg, 2000.
- [47] E. M. Purcell, “Spontaneous emission probabilities at radio frequencies,” *Physical Review*, vol. 69, 1946.
- [48] J. P. Reithmaier, G. Sek, A. Löffler, C. Hofmann, S. Kuhn, S. Reitzenstein, L. V. Keldysh, V. D. Kulakovskii, T. L. Reinecke, and A. Forchel, “Strong coupling in a single quantum dot-semiconductor microcavity system,” *Nature*, vol. 432, no. 7014, pp. 197–200, 2004.
- [49] E. Peter, P. Senellart, D. Martrou, A. Lemaître, J. Hours, J. M. Gérard, and J. Bloch, “Exciton-photon strong-coupling regime for a single quantum dot embedded in a microcavity,” *Physical Review Letters*, vol. 95, no. 6, p. 067401, 2005.
- [50] D. Najer, I. Söllner, P. Sekatski, V. Dolique, M. C. Löbl, D. Riedel, R. Schott, S. Starosielec, S. R. Valentin, A. D. Wieck, N. Sangouard, A. Ludwig, and R. J. Warburton, “A gated quantum dot strongly coupled to an optical microcavity,” *Nature*, vol. 575, no. 7784, pp. 622–627, 2019.
- [51] A. J. Bennett, P. Atkinson, P. See, M. B. Ward, R. M. Stevenson, Z. L. Yuan, D. C. Unitt, D. J. P. Ellis, K. Cooper, D. A. Ritchie, and A. J. Shields, “Single-photon-emitting diodes: a review,” *Physica status solidi (b)*, vol. 243, no. 14, pp. 3730–3740, 2006.
- [52] J. Nilsson, *Electrically generated entangled light for optical quantum information applications*. Phd thesis, Universite‘ Blaise Pascal - Clermont-Ferrand II, 2013.

- 
- [53] Y. Ma, P. E. Kremer, and B. D. Gerardot, “Efficient photon extraction from a quantum dot in a broad-band planar cavity antenna,” *Journal of Applied Physics*, vol. 115, no. 2, p. 023106, 2014.
- [54] P. Bharadwaj, B. Deutsch, and L. Novotny, “Optical antennas,” *Advances in Optics and Photonics*, vol. 1, no. 3, p. 438, 2009.
- [55] M. Ohring, *Materials science of thin films*. ACADEMIC Press, 2013.
- [56] B. Bhushan, ed., *Springer Handbook of Nanotechnology*. Springer Handbooks, Berlin, Heidelberg: Springer Berlin Heidelberg, 2017.
- [57] R. Nötzel, “Self-organized growth of quantum-dot structures,” *Semiconductor Science and Technology*, vol. 11, no. 10, pp. 1365–1379, 1996.
- [58] A. Y. Cho and J. R. Arthur, “Molecular beam epitaxy,” *Progress in Solid State Chemistry*, vol. 10, pp. 157–191, 1975.
- [59] I. N. Stranski and L. Krastanow, “Zur theorie der orientierten ausscheidung von ionenkristallen aufeinander,” *Monatshefte für Chemie*, vol. 71, no. 1, pp. 351–364, 1937.
- [60] R. J. Warburton, “Single spins in self-assembled quantum dots,” *Nature Materials*, vol. 12, no. 6, pp. 483–493, 2013.
- [61] M. Felle, J. Huwer, R. M. Stevenson, J. Skiba-Szymanska, M. B. Ward, I. Farrer, R. V. Penty, D. A. Ritchie, and A. J. Shields, “Interference with a quantum dot single-photon source and a laser at telecom wavelength,” *Applied Physics Letters*, vol. 107, no. 13, p. 131106, 2015.
- [62] P. Senellart, G. Solomon, and A. White, “High-performance semiconductor quantum-dot single-photon sources,” *Nature Nanotechnology*, vol. 12, no. 11, pp. 1026–1039, 2017.
- [63] L. Hanschke, K. A. Fischer, S. Appel, D. Lukin, J. Wierzbowski, S. Sun, R. Trivedi, J. Vučković, J. J. Finley, and K. Müller, “Quantum dot single-photon

- sources with ultra-low multi-photon probability,” *npj Quantum Information*, vol. 4, no. 1, 2018.
- [64] M. Gurioli, Z. Wang, A. Rastelli, T. Kuroda, and S. Sanguinetti, “Droplet epitaxy of semiconductor nanostructures for quantum photonic devices,” *Nature Materials*, vol. 18, no. 8, pp. 799–810, 2019.
- [65] N. Koguchi, S. Takahashi, and T. Chikyow, “New mbe growth method for InSb quantum well boxes,” *Journal of Crystal Growth*, vol. 111, no. 1-4, pp. 688–692, 1991.
- [66] N. Koguchi and K. Ishige, “Growth of GaAs epitaxial microcrystals on an S-terminated GaAs substrate by successive irradiation of Ga and As molecular beams,” *Japanese Journal of Applied Physics*, vol. 32, no. Part 1, No. 5A, pp. 2052–2058, 1993.
- [67] A. Nemcsics, “Quantum dots prepared by droplet epitaxial method,” in *Quantum Dots - Theory and Applications* (V. N. Stavrou, ed.), InTech, 2015.
- [68] J. Wu and Z. M. Wang, “Droplet epitaxy for advanced optoelectronic materials and devices,” *Journal of Physics D: Applied Physics*, vol. 47, p. 173001, 2014.
- [69] C. Somaschini, S. Bietti, N. Koguchi, and S. Sanguinetti, “Fabrication of multiple concentric nanoring structures,” *Nano letters*, vol. 9, no. 10, pp. 3419–3424, 2009.
- [70] COMSOL AB, Stockholm, Sweden, “Comsol multiphysics cyclopedia: physics, PDEs and numerical modeling, finite element method,” 2017.
- [71] K. H. Huebner, *The finite element method for engineers*. New York: Wiley, 4. ed. ed., 2001.
- [72] M. G. Larson and F. Bengzon, *The finite element method: theory, implementation, and applications*. Berlin and Heidelberg: Springer, 2013.

- 
- [73] COMSOL AB, Stockholm, Sweden, “Wave Optics module user’s guide: Comsol multiphysics v. 5.4,” 2019.
- [74] D. Leonard, “Molecular-beam epitaxy growth of quantum dots from strained coherent uniform islands of InGaAs on GaAs,” *Journal of Vacuum Science & Technology B: Microelectronics and Nanometer Structures*, vol. 12, no. 2, p. 1063, 1994.
- [75] M. Levinshtein, S. Rumyantsev, and M. Shur, *Handbook Series on Semiconductor Parameters*, vol. 2. WORLD SCIENTIFIC, 1996.
- [76] J. Liu, R. Su, Y. Wei, B. Yao, S. F. C. d. Silva, Y. Yu, J. Iles-Smith, K. Srinivasan, A. Rastelli, J. Li, and X. Wang, “A solid-state source of strongly entangled photon pairs with high brightness and indistinguishability,” *Nature Nanotechnology*, 2019.
- [77] H. Wang, H. Hu, T.-H. Chung, J. Qin, X. Yang, J.-P. Li, R.-Z. Liu, H.-S. Zhong, Y.-M. He, X. Ding, Y.-H. Deng, Q. Dai, Y.-H. Huo, S. Höfling, C.-Y. Lu, and J.-W. Pan, “On-demand semiconductor source of entangled photons which simultaneously has high fidelity, efficiency, and indistinguishability,” *Physical review letters*, vol. 122, no. 11, p. 113602, 2019.
- [78] W. Reinert, *Handbook of Silicon Based MEMS Materials and Technologies*. Elsevier, 2015.
- [79] E.-A. Moon, J.-L. Lee, and H. M. Yoo, “Selective wet etching of GaAs on  $\text{Al}_x\text{Ga}_{1-x}\text{As}$  for AlGaAs/InGaAs/AlGaAs pseudomorphic high electron mobility transistor,” *Journal of Applied Physics*, vol. 84, no. 7, pp. 3933–3938, 1998.
- [80] W. Hu, K. Sarveswaran, M. Lieberman, and G. H. Bernstein, “Sub-10 nm electron beam lithography using cold development of poly(methylmethacrylate),” *Journal of Vacuum Science & Technology B: Microelectronics and Nanometer Structures*, vol. 22, no. 4, p. 1711, 2004.

- [81] I.-B. Baek, J.-H. Yang, W.-J. Cho, C.-G. Ahn, K. Im, and S. Lee, “Electron beam lithography patterning of sub-10 nm line using hydrogen silsesquioxane for nanoscale device applications,” *Journal of Vacuum Science & Technology B: Microelectronics and Nanometer Structures*, vol. 23, no. 6, p. 3120, 2005.
- [82] Y. Chen, “Nanofabrication by electron beam lithography and its applications: a review,” *Microelectronic Engineering*, vol. 135, pp. 57–72, 2015.
- [83] ZEON CORPORATION, Tokyo , JAPAN, “ZEP 520A, high resolution positive electron beam resist, technical report,” 2003.
- [84] K. Kurihara, K. Iwadate, H. Namatsu, M. Nagase, H. Takenaka, and K. Murase, “An electron beam nanolithography system and its application to Si nanofabrication,” *Japanese Journal of Applied Physics*, vol. 34, no. Part 1, No. 12B, pp. 6940–6946, 1995.
- [85] T. Nishida, M. Notomi, R. Iga, and T. Tamamura, “Quantum wire fabrication by e-beam lithography using high-resolution and high-sensitivity e-beam resist ZEP520,” *Japanese Journal of Applied Physics*, vol. 31, no. Part 1, No. 12B, pp. 4508–4514, 1992.
- [86] S.-F. Hu, C.-L. Sung, K.-D. Huang, and Y.-M. Wan, “Proximity effect of electron beam lithography for single-electron transistor fabrication,” *Applied Physics Letters*, vol. 85, no. 17, pp. 3893–3895, 2004.
- [87] G. Owen, “Proximity effect correction in electron-beam lithography,” *Optical Engineering*, vol. 32, no. 10, pp. 2446–2451, 1993.
- [88] Micro resist technology, Berlin, Germany, “Microposit remover 1165, technical data sheet,” 2015.
- [89] P. Lelong and G. Bastard, “Binding energies of excitons and charged excitons in GaAsGa(In)As quantum dots.,” *Solid State Communications*, vol. 98, no. 9, pp. 819–823, 1996.

- 
- [90] Becker & Hickl GmbH, “The BH TCSPC handbook 8<sup>th</sup> ed.,” 2019.
- [91] Becker & Hickl GmbH, “Time-correlated single photon counting modules, SPC module manual,” 2002.
- [92] H. J. Kimble, M. Dagenais, and L. Mandel, “Photon antibunching in resonance fluorescence,” *Physical Review Letters*, vol. 39, no. 11, pp. 691–695, 1977.
- [93] A. Auffèves, D. Gerace, S. Portolan, A. Drezet, and M. França Santos, “Few emitters in a cavity: from cooperative emission to individualization,” *New Journal of Physics*, vol. 13, no. 9, p. 093020, 2011.
- [94] H. J. Kimble, “The quantum internet,” *Nature*, vol. 453, no. 7198, pp. 1023–1030, 2008.
- [95] S. Wehner, D. Elkouss, and R. Hanson, “Quantum internet: a vision for the road ahead,” *Science (New York, N. Y.)*, vol. 362, no. 6412, 2018.
- [96] A. Orioux, M. A. M. Versteegh, K. D. Jöns, and S. Ducci, “Semiconductor devices for entangled photon pair generation: a review,” *Reports on Progress in Physics*, vol. 80, no. 7, p. 076001, 2017.
- [97] D. Huber, M. Reindl, J. Aberl, A. Rastelli, and R. Trotta, “Semiconductor quantum dots as an ideal source of polarization-entangled photon pairs on-demand: a review,” *Japanese Journal of Applied Physics*, vol. 20, no. 7, p. 073002, 2018.
- [98] S. E. Thomas, M. Billard, N. Coste, S. C. Wein, Priya, H. Ollivier, O. Krebs, L. Tazaïrt, A. Harouri, A. Lemaitre, I. Sagnes, C. Anton, L. Lanco, N. Somaschi, J. C. Loredó, and P. Senellart, “Bright polarized single-photon source based on a linear dipole,” *Physical Review Letters*, vol. 126, no. 23, p. 233601, 2021.
- [99] M. Sartison, S. L. Portalupi, T. Gissibl, M. Jetter, H. Giessen, and P. Michler, “Combining in-situ lithography with 3D printed solid immersion lenses for single quantum dot spectroscopy,” *Scientific Reports*, vol. 7, p. 39916, 2017.

- [100] V. D. Kulakovskii, G. Bacher, R. Weigand, T. KÜmmell, A. Forchel, E. Borovitskaya, K. Leonardi, and D. Hommel, “Fine structure of biexciton emission in symmetric and asymmetric CdSe/ZnSe single quantum dots,” *Physical Review Letters*, vol. 82, no. 8, pp. 1780–1783, 1999.
- [101] T. Mano, M. Abbarchi, T. Kuroda, B. McSkimming, A. Ohtake, K. Mitsuishi, and K. Sakoda, “Self-assembly of symmetric GaAs quantum dots on (111)A substrates: suppression of fine-structure splitting,” *Applied Physics Express*, vol. 3, no. 6, p. 065203, 2010.
- [102] T. Kuroda, T. Mano, N. Ha, H. Nakajima, H. Kumano, B. Urbaszek, M. Jo, M. Abbarchi, Y. Sakuma, K. Sakoda, I. Suemune, X. Marie, and T. Amand, “Symmetric quantum dots as efficient sources of highly entangled photons: violation of Bell’s inequality without spectral and temporal filtering,” *Physical Review B*, vol. 88, no. 4, 2013.
- [103] N. Ha, T. Mano, T. Kuroda, K. Mitsuishi, A. Ohtake, A. Castellano, S. Sanguinetti, T. Noda, Y. Sakuma, and K. Sakoda, “Droplet epitaxy growth of telecom InAs quantum dots on metamorphic InAlAs/GaAs(111)A,” *Japanese Journal of Applied Physics*, vol. 54, no. 4S, p. 04DH07, 2015.
- [104] S. L. Portalupi, M. Jetter, and P. Michler, “InAs quantum dots grown on metamorphic buffers as non-classical light sources at telecom C-band: a review,” *Semiconductor Science and Technology*, vol. 34, no. 5, p. 053001, 2019.
- [105] A. Tuktamyshev, A. Fedorov, S. Bietti, S. Vichi, K. D. Zeuner, K. D. Jöns, D. Chrastina, S. Tsukamoto, V. Zwiller, M. Gurioli, and S. Sanguinetti, “Telecom-wavelength InAs QDs with low fine structure splitting grown by droplet epitaxy on GaAs(111)A vicinal substrates,” *Applied Physics Letters*, vol. 118, no. 13, p. 133102, 2021.
- [106] M. B. Ward, M. C. Dean, R. M. Stevenson, A. J. Bennett, D. Ellis, K. Cooper, I. Farrer, C. A. Nicoll, D. A. Ritchie, and A. J. Shields, “Coherent dynamics

- of a telecom-wavelength entangled photon source,” *Nature communications*, vol. 5, no. 1, p. 3316, 2014.
- [107] J. Huwer, R. M. Stevenson, J. Skiba-Szymanska, M. B. Ward, A. J. Shields, M. Felle, I. Farrer, D. A. Ritchie, and R. V. Penty, “Quantum-dot-based telecommunication-wavelength quantum relay,” *Physical Review Applied*, vol. 8, no. 2, 2017.
- [108] T. Müller, J. Skiba-Szymanska, A. B. Krysa, J. Huwer, M. Felle, M. Anderson, R. M. Stevenson, J. Heffernan, D. A. Ritchie, and A. J. Shields, “A quantum light-emitting diode for the standard telecom window around 1550 nm,” *Nature communications*, vol. 9, no. 1, p. 862, 2018.
- [109] L. Esposito, S. Bietti, A. Fedorov, R. Nötzel, and S. Sanguinetti, “Ehrlich-schwöbel effect on the growth dynamics of GaAs(111)A surfaces,” *Physical Review Materials*, vol. 1, no. 2, 2017.
- [110] F. Herzog, M. Bichler, G. Koblmüller, S. Prabhu-Gaunkar, W. Zhou, and M. Grayson, “Optimization of AlAs/AlGaAs quantum well heterostructures on on-axis and misoriented GaAs (111)B,” *Applied Physics Letters*, vol. 100, no. 19, p. 192106, 2012.
- [111] A. Tuktamyshev, A. Fedorov, S. Bietti, S. Tsukamoto, and S. Sanguinetti, “Temperature activated dimensionality crossover in the nucleation of quantum dots by droplet epitaxy on GaAs(111)A vicinal substrates,” *Scientific Reports*, vol. 9, no. 1, p. 14520, 2019.
- [112] R. J. Young, R. M. Stevenson, A. J. Shields, P. Atkinson, K. Cooper, D. A. Ritchie, K. M. Groom, A. I. Tartakovskii, and M. S. Skolnick, “Inversion of exciton level splitting in quantum dots,” *Physical Review B*, vol. 72, no. 11, 2005.

- [113] P. N. Keating, “Effect of invariance requirements on the elastic strain energy of crystals with application to the diamond structure,” *Physical Review*, vol. 145, no. 2, pp. 637–645, 1966.
- [114] A. J. Williamson, L. W. Wang, and A. Zunger, “Theoretical interpretation of the experimental electronic structure of lens-shaped self-assembled InAs/GaAs quantum dots,” *Physical review. B, Condensed matter*, vol. 62, no. 19, pp. 12963–12977, 2000.
- [115] G. Bester, “Electronic excitations in nanostructures: an empirical pseudopotential based approach,” *Journal of physics: Condensed matter*, vol. 21, no. 2, p. 023202, 2009.
- [116] L.-W. Wang and A. Zunger, “Linear combination of bulk bands method for large-scale electronic structure calculations on strained nanostructures,” *Physical review. B, Condensed matter*, vol. 59, no. 24, pp. 15806–15818, 1999.
- [117] A. Franceschetti, H. Fu, L. W. Wang, and A. Zunger, “Many-body pseudopotential theory of excitons in InP and CdSe quantum dots,” *Physical Review B*, vol. 60, no. 3, pp. 1819–1829, 1999.
- [118] R. Resta, “Thomas-Fermi dielectric screening in semiconductors,” *Physical Review B*, vol. 16, no. 6, pp. 2717–2722, 1977.
- [119] W. Sheng, “Origins of optical anisotropy in artificial atoms,” *Applied Physics Letters*, vol. 89, no. 17, p. 173129, 2006.
- [120] R. Sittig, C. Nawrath, S. Kolatschek, S. Bauer, R. Schaber, J. Huang, P. Vijayan, P. Pruy, S. L. Portalupi, M. Jetter, and P. Michler, “Thin-film InGaAs metamorphic buffer for telecom C-band InAs quantum dots and optical resonators on GaAs platform,” *Nanophotonics*, vol. 11, no. 6, p. 1109–1116, 2022.

- 
- [121] R. M. Stevenson, R. J. Young, P. Atkinson, K. Cooper, D. A. Ritchie, and A. J. Shields, “A semiconductor source of triggered entangled photon pairs,” *Nature*, vol. 439, no. 7073, pp. 179–182, 2006.
- [122] P. Zhao and H. Zhao, “Analysis of light extraction efficiency enhancement for thin-film flip-chip InGaN quantum wells light-emitting diodes with GaN micro-domes,” *Optics express*, vol. 20 Suppl 5, pp. A765–76, 2012.
- [123] G. Björk, S. Machida, Y. Yamamoto, and K. Igeta, “Modification of spontaneous emission rate in planar dielectric microcavity structures,” *Physical Review A*, vol. 44, no. 1, pp. 669–681, 1991.
- [124] T. Heindel, C. Schneider, M. Lermer, S. H. Kwon, T. Braun, S. Reitzenstein, S. Höfling, M. Kamp, and A. Forchel, “Electrically driven quantum dot-micropillar single photon source with 34% overall efficiency,” *Applied Physics Letters*, vol. 96, no. 1, p. 011107, 2010.
- [125] M. Davanço, M. T. Rakher, D. Schuh, A. Badolato, and K. Srinivasan, “A circular dielectric grating for vertical extraction of single quantum dot emission,” *Applied Physics Letters*, vol. 99, no. 4, p. 041102, 2011.
- [126] L. Sapienza, M. Davanço, A. Badolato, and K. Srinivasan, “Nanoscale optical positioning of single quantum dots for bright and pure single-photon emission,” *Nature communications*, vol. 6, pp. 7833 EP –, 2015.
- [127] L. Rickert, T. Kupko, S. Rodt, S. Reitzenstein, and T. Heindel, “Optimized designs for telecom-wavelength quantum light sources based on hybrid circular Bragg gratings,” *Optics express*, vol. 27, no. 25, p. 36824, 2019.
- [128] S. Kolatschek, C. Nawrath, S. Bauer, J. Huang, J. Fischer, R. Sittig, M. Jetter, S. L. Portalupi, and P. Michler, “Bright purcell enhanced single-photon source in the telecom O-band based on a quantum dot in a circular Bragg grating,” *Nano letters*, vol. 21, no. 18, pp. 7740–7745, 2021.

- [129] B. Yao, R. Su, Y. Wei, Z. Liu, T. Zhao, and J. Liu, “Design for hybrid circular Bragg gratings for a highly efficient quantum-dot single-photon source,” *Journal of the Korean Physical Society*, vol. 73, no. 10, pp. 1502–1505, 2018.
- [130] D. Englund, A. Faraon, I. Fushman, N. Stoltz, P. Petroff, and J. Vučković, “Controlling cavity reflectivity with a single quantum dot,” *Nature*, vol. 450, no. 7171, pp. 857–861, 2007.
- [131] M. S. Ghamsari, *Quantum-dot Based Light-emitting Diodes*. InTech, 2017.
- [132] S. Kolatschek, S. Hepp, M. Sartison, M. Jetter, P. Michler, and S. L. Portalupi, “Deterministic fabrication of circular Bragg gratings coupled to single quantum emitters via the combination of in-situ optical lithography and electron-beam lithography,” *Journal of Applied Physics*, vol. 125, no. 4, p. 045701, 2019.
- [133] J.-H. Kim, T. Cai, C. J. K. Richardson, R. P. Leavitt, and E. Waks, “Two-photon interference from a bright single-photon source at telecom wavelengths,” *Optica*, vol. 3, no. 6, p. 577, 2016.
- [134] S. Haffouz, K. D. Zeuner, D. Dalacu, P. J. Poole, J. Lapointe, D. Poitras, K. Mnaymneh, X. Wu, M. Couillard, M. Korkusinski, E. Schöll, K. D. Jöns, V. Zwiller, and R. L. Williams, “Bright single InAsP quantum dots at telecom wavelengths in position-controlled InP nanowires: The role of the photonic waveguide,” *Nano letters*, vol. 18, no. 5, pp. 3047–3052, 2018.
- [135] N. Srocka, P. Mrowiński, J. Große, M. von Helversen, T. Heindel, S. Rodt, and S. Reitzenstein, “Deterministically fabricated quantum dot single-photon source emitting indistinguishable photons in the telecom O-band,” *Applied Physics Letters*, vol. 116, no. 23, p. 231104, 2020.
- [136] C. L. Morrison, M. Rambach, Z. X. Koong, F. Graffitti, F. Thorburn, A. K. Kar, Y. Ma, S.-I. Park, J. D. Song, N. G. Stoltz, D. Bouwmeester, A. Fedrizzi, and B. D. Gerardot, “A bright source of telecom single photons based on quantum

- frequency conversion,” *Applied Physics Letters*, vol. 118, no. 17, p. 174003, 2021.
- [137] K. D. Zeuner, K. D. Jöns, L. Schweickert, C. Reuterskiöld Hedlund, C. Nuñez Lobato, T. Lettner, K. Wang, S. Gyger, E. Schöll, S. Steinhauer, M. Hammar, and V. Zwiller, “On-demand generation of entangled photon pairs in the telecom C-band with inas quantum dots,” *ACS Photonics*, vol. 8, no. 8, pp. 2337–2344, 2021.
- [138] B. Da Lio, C. Faurby, X. Zhou, M. L. Chan, R. Uppu, H. Thyrrerstrup, S. Scholz, A. D. Wieck, A. Ludwig, P. Lodahl, and L. Midolo, “A pure and indistinguishable single-photon source at telecommunication wavelength.”
- [139] O. Gazzano, T. Huber, V. Loo, S. Polyakov, E. B. Flagg, and G. S. Solomon, “Effects of resonant-laser excitation on the emission properties in a single quantum dot,” *Optica*, vol. 5, no. 4, p. 354, 2018.
- [140] E. Schöll, L. Hanschke, L. Schweickert, K. D. Zeuner, M. Reindl, S. F. Covre da Silva, T. Lettner, R. Trotta, J. J. Finley, K. Müller, A. Rastelli, V. Zwiller, and K. D. Jöns, “Resonance fluorescence of GaAs quantum dots with near-unity photon indistinguishability,” *Nano letters*, vol. 19, no. 4, pp. 2404–2410, 2019.
- [141] S. Thomas and P. Senellart, “The race for the ideal single-photon source is on,” *Nature Nanotechnology*, 2021.
- [142] N. Srocka, P. Mrowiński, J. Große, M. Schmidt, S. Rodt, and S. Reitzenstein, “Deterministically fabricated strain-tunable quantum dot single-photon sources emitting in the telecom O-band,” *Applied Physics Letters*, vol. 117, no. 22, p. 224001, 2020.
- [143] M. Anderson, T. Müller, J. Skiba-Szymanska, A. B. Krysa, J. Huwer, R. M. Stevenson, J. Heffernan, D. A. Ritchie, and A. J. Shields, “Coherence in single photon emission from droplet epitaxy and Stranski–Krastanov quantum dots

- in the telecom c-band,” *Applied Physics Letters*, vol. 118, no. 1, p. 014003, 2021.
- [144] S. Fafard, Z. Wasilewski, J. McCaffrey, S. Raymond, and S. Charbonneau, “InAs self-assembled quantum dots on InP by molecular beam epitaxy,” *Applied Physics Letters*, vol. 68, no. 7, pp. 991–993, 1996.
- [145] R. Leonelli, C. A. Tran, J. L. Brebner, G. J. T., T. T., R. A. Masut, and S. Charbonneau, “Optical and structural properties of metalorganic-vapor-phase-epitaxy-grown InAs quantum wells and quantum dots in InP,” *Physical review. B, Condensed matter*, vol. 48, no. 15, pp. 11135–11143, 1993.
- [146] C. Nawrath, F. Olbrich, M. Paul, S. L. Portalupi, M. Jetter, and P. Michler, “Coherence and indistinguishability of highly pure single photons from non-resonantly and resonantly excited telecom C-band quantum dots,” *Applied Physics Letters*, vol. 115, no. 2, p. 023103, 2019.
- [147] M. Anderson, T. Müller, J. Huwer, J. Skiba-Szymanska, A. B. Krysa, R. M. Stevenson, J. Heffernan, D. A. Ritchie, and A. J. Shields, “Quantum teleportation using highly coherent emission from telecom C-band quantum dots,” *npj Quantum Information*, vol. 6, no. 1, p. 14, 2020.
- [148] J. Schall, M. Deconinck, N. Bart, M. Florian, M. Helversen, C. Dangel, R. Schmidt, L. Bremer, F. Bopp, I. Hüllen, C. Gies, D. Reuter, A. D. Wieck, S. Rodt, J. J. Finley, F. Jahnke, A. Ludwig, and S. Reitzenstein, “Bright electrically controllable quantum-dot-molecule devices fabricated by in situ electron-beam lithography,” *Advanced Quantum Technologies*, vol. 4, no. 6, p. 2100002, 2021.
- [149] S. A. Blokhin, M. A. Bobrov, N. A. Maleev, J. N. Donges, L. Bremer, A. A. Blokhin, A. P. Vasil’ev, A. G. Kuzmenkov, E. S. Kolodeznyi, V. A. Shchukin, N. N. Ledentsov, S. Reitzenstein, and V. M. Ustinov, “Design optimization for bright electrically-driven quantum dot single-photon sources emitting in telecom O-band,” *Optics express*, vol. 29, no. 5, pp. 6582–6598, 2021.

- 
- [150] S. Adachi, “Optical dispersion relations for GaP, GaAs, GaSb, InP, InAs, InSb,  $\text{Al}_x\text{Ga}_{1-x}\text{As}$  and  $\text{In}_{1-x}\text{Ga}_x\text{As}_y\text{P}_{1-y}$ ,” *Journal of Applied Physics*, vol. 66, no. 12, pp. 6030–6040, 1989.
- [151] I. H. Malitson, “Interspecimen comparison of the refractive index of fused Silica,” *Journal of the Optical Society of America*, vol. 55, no. 10, p. 1205, 1965.
- [152] D. I. Yakubovsky, A. V. Arsenin, Y. V. Stebunov, D. Y. Fedyanin, and V. S. Volkov, “Optical constants and structural properties of thin gold films,” *Optics express*, vol. 25, no. 21, pp. 25574–25587, 2017.
- [153] S. Rodt, S. Reitzenstein, and T. Heindel, “Deterministically fabricated solid-state quantum-light sources,” *Journal of Physics: Condensed Matter*, vol. 32, no. 15, p. 153003, 2020.
- [154] A. Kaganskiy, M. Gschrey, A. Schlehahn, R. Schmidt, J.-H. Schulze, T. Heindel, A. Strittmatter, S. Rodt, and S. Reitzenstein, “Advanced in-situ electron-beam lithography for deterministic nanophotonic device processing,” *The Review of scientific instruments*, vol. 86, no. 7, p. 073903, 2015.
- [155] J. Liu, M. I. Davanço, L. Sapienza, K. Konthasinghe, de Miranda Cardoso, José Vinícius, J. D. Song, A. Badolato, and K. Srinivasan, “Cryogenic photoluminescence imaging system for nanoscale positioning of single quantum emitters,” *The Review of scientific instruments*, vol. 88, no. 2, p. 023116, 2017.
- [156] A. Musiał, K. Żołnacz, N. Srocka, O. Kravets, J. Große, J. Olszewski, K. Poturaj, G. Wójcik, P. Mergo, K. Dybka, M. Dyrkacz, M. Dłubek, K. Lauritsen, A. Bültner, P.-I. Schneider, L. Zschiedrich, S. Burger, S. Rodt, W. Urbańczyk, G. Sęk, and S. Reitzenstein, “Plug&play fiber-coupled 73 khz single-photon source operating in the telecom O-band,” *Advanced Quantum Technologies*, vol. 3, no. 6, p. 2000018, 2020.

- [157] L. Rickert, F. Schröder, T. Kupko, C. Schneider, S. Höfling, and T. Heindel, “Fiber-pigtailing quantum-dot cavity-enhanced light emitting diodes,” *Applied Physics Letters*, vol. 119, no. 13, p. 131104, 2021.
- [158] A. Schlehahn, S. Fischbach, R. Schmidt, A. Kaganskiy, A. Strittmatter, S. Rodt, T. Heindel, and S. Reitzenstein, “A stand-alone fiber-coupled single-photon source,” *Scientific Reports*, vol. 8, no. 1, p. 1340, 2018.
- [159] H. Snijders, J. A. Frey, J. Norman, V. P. Post, A. C. Gossard, J. E. Bowers, M. P. van Exter, W. Löffler, and D. Bouwmeester, “Fiber-coupled cavity-QED source of identical single photons,” *Physical Review Applied*, vol. 9, no. 3, 2018.
- [160] P.-I. Schneider, N. Srocka, S. Rodt, L. Zschiedrich, S. Reitzenstein, and S. Burger, “Numerical optimization of the extraction efficiency of a quantum-dot based single-photon emitter into a single-mode fiber,” *Optics express*, vol. 26, no. 7, pp. 8479–8492, 2018.
- [161] P. Yin, J. R. Serafini, Z. Su, R.-J. Shiue, E. Timurdogan, M. L. Fanto, and S. Preble, “Low connector-to-connector loss through silicon photonic chips using ultra-low loss splicing of SMF-28 to high numerical aperture fibers,” *Optics express*, vol. 27, no. 17, pp. 24188–24193, 2019.
- [162] R. Marchetti, C. Lacava, L. Carroll, K. Gradkowski, and P. Minzioni, “Coupling strategies for silicon photonics integrated chips,” *Photonics Research*, vol. 7, no. 2, p. 201, 2019.
- [163] Y. Tang, Z. Wang, L. Wosinski, U. Westergren, and S. He, “Highly efficient nonuniform grating coupler for Silicon-on-Insulator nanophotonic circuits,” *Optics Letters*, vol. 35, no. 8, pp. 1290–1292, 2010.
- [164] A. Bozzola, L. Carroll, D. Gerace, I. Cristiani, and L. C. Andreani, “Optimising apodized grating couplers in a pure SOI platform to -0.5 dB coupling efficiency,” *Optics express*, vol. 23, no. 12, pp. 16289–16304, 2015.

- 
- [165] R. Marchetti, C. Lacava, A. Khokhar, X. Chen, I. Cristiani, D. J. Richardson, G. T. Reed, P. Petropoulos, and P. Minzioni, “High-efficiency grating-couplers: demonstration of a new design strategy,” *Scientific Reports*, vol. 7, no. 1, 2017.
- [166] E. F. Schubert, C. J. Pinzone, and M. Geva, “Phenomenology of Zn diffusion and incorporation in InP grown by organometallic vapor-phase epitaxy (OMVPE),” *Applied Physics Letters*, vol. 67, no. 5, pp. 700–702, 1995.
- [167] Z. Li, I. Yang, L. Li, Q. Gao, J. S. Chong, Z. Li, M. N. Lockrey, H. H. Tan, C. Jagadish, and L. Fu, “Reducing Zn diffusion in single axial junction InP nanowire solar cells for improved performance,” *Progress in Natural Science: Materials International*, vol. 28, no. 2, pp. 178–182, 2018.
- [168] Y.-M. He, J. Liu, S. Maier, M. Emmerling, S. Gerhardt, M. Davanço, K. Srinivasan, C. Schneider, and S. Höfling, “Deterministic implementation of a bright, on-demand single photon source with near-unity indistinguishability via quantum dot imaging,” *Optica*, vol. 4, no. 7, pp. 802–808, 2017.
- [169] M. Toth and I. Aharonovich, “Single photon sources in atomically thin materials,” *Annual review of physical chemistry*, vol. 70, pp. 123–142, 2019.
- [170] J. Dang, S. Sun, X. Xie, Y. Yu, K. Peng, C. Qian, S. Wu, F. Song, J. Yang, S. Xiao, L. Yang, Y. Wang, M. A. Rafiq, C. Wang, and X. Xu, “Identifying defect-related quantum emitters in monolayer WSe<sub>2</sub>,” *npj 2D Materials and Applications*, vol. 4, no. 1, p. 136805, 2020.
- [171] A. Srivastava, M. Sidler, A. V. Allain, D. S. Lembke, A. Kis, and A. Imamoglu, “Optically active quantum dots in monolayer WSe<sub>2</sub>,” *Nature Nanotechnology*, vol. 10, pp. 491 EP –, 2015.
- [172] Y.-M. He, G. Clark, J. R. Schaibley, Y. He, M.-C. Chen, Y.-J. Wei, X. Ding, Q. Zhang, W. Yao, X. Xu, C.-Y. Lu, and J.-W. Pan, “Single quantum emitters in monolayer semiconductors,” *Nature Nanotechnology*, vol. 10, pp. 497 EP –, 2015.

- [173] M. Koperski, K. Nogajewski, A. Arora, V. Cherkez, P. Mallet, J.-Y. Veuillen, J. Marcus, P. Kossacki, and M. Potemski, “Single photon emitters in exfoliated WSe<sub>2</sub> structures,” *Nature Nanotechnology*, vol. 10, pp. 503 EP –, 2015.
- [174] C. Palacios-Berraquero, M. Barbone, D. M. Kara, X. Chen, I. Goykhman, D. Yoon, A. K. Ott, J. Beitner, K. Watanabe, T. Taniguchi, A. C. Ferrari, and M. Atatüre, “Atomically thin quantum light-emitting diodes,” *Nature communications*, vol. 7, p. 12978, 2016.
- [175] B. Schuler, K. A. Cochrane, C. Kastl, E. S. Barnard, E. Wong, N. J. Borys, A. M. Schwartzberg, D. F. Ogletree, F. J. G. de Abajo, and A. Weber-Bargioni, “Electrically driven photon emission from individual atomic defects in monolayer WSe<sub>2</sub>,” *Science advances*, vol. 6, no. 38, 2020.
- [176] C. Chakraborty, L. Kinnischtzke, K. M. Goodfellow, R. Beams, and A. N. Vamivakas, “Voltage-controlled quantum light from an atomically thin semiconductor,” *Nature Nanotechnology*, vol. 10, pp. 507 EP –, 2015.
- [177] C. Palacios-Berraquero, D. M. Kara, A. R.-P. Montblanch, M. Barbone, P. Latawiec, D. Yoon, A. K. Ott, M. Loncar, A. C. Ferrari, and M. Atatüre, “Large-scale quantum-emitter arrays in atomically thin semiconductors,” *Nature communications*, vol. 8, p. 15093, 2017.
- [178] O. Iff, D. Tedeschi, J. Martín-Sánchez, M. Moczala-Dusanowska, S. Tongay, K. Yumigeta, J. Taboada-Gutiérrez, M. Savaresi, A. Rastelli, P. Alonso-González, S. Höfling, R. Trotta, and C. Schneider, “Strain-tunable single photon sources in WSe<sub>2</sub> monolayers,” *Nano letters*, vol. 19, no. 10, pp. 6931–6936, 2019.
- [179] L. Zhang, R. Gogna, W. Burg, E. Tutuc, and H. Deng, “Photonic-crystal exciton-polaritons in monolayer semiconductors,” *Nature communications*, vol. 9, no. 1, p. 713, 2018.

- 
- [180] L. C. Flatten, L. Weng, A. Branny, S. Johnson, P. R. Dolan, A. A. P. Trichet, B. D. Gerardot, and J. M. Smith, “Microcavity enhanced single photon emission from two-dimensional WSe<sub>2</sub>,” *Applied Physics Letters*, vol. 112, no. 19, p. 191105, 2018.
- [181] N. M. H. Duong, Z.-Q. Xu, M. Kianinia, R. Su, Z. Liu, S. Kim, C. Bradac, T. T. Tran, Y. Wan, L.-J. Li, A. Solntsev, J. Liu, and I. Aharonovich, “Enhanced emission from WSe<sub>2</sub> monolayers coupled to circular Bragg gratings,” *ACS Photonics*, vol. 5, no. 10, pp. 3950–3955, 2018.
- [182] Z. Wang, Z. Dong, Y. Gu, Y.-H. Chang, L. Zhang, L.-J. Li, W. Zhao, G. Eda, W. Zhang, G. Grinblat, S. A. Maier, J. K. W. Yang, C.-W. Qiu, and A. T. S. Wee, “Giant photoluminescence enhancement in tungsten-diselenide-gold plasmonic hybrid structures,” *Nature communications*, vol. 7, p. 11283, 2016.
- [183] S. Bidault, M. Mivelle, and N. Bonod, “Dielectric nanoantennas to manipulate solid-state light emission,” *Journal of Applied Physics*, vol. 126, no. 9, p. 094104, 2019.
- [184] Y. Luo, G. D. Shepard, J. V. Ardelean, D. A. Rhodes, B. Kim, K. Barmak, J. C. Hone, and S. Strauf, “Deterministic coupling of site-controlled quantum emitters in monolayer WSe<sub>2</sub> to plasmonic nanocavities,” *Nature Nanotechnology*, vol. 13, no. 12, pp. 1137–1142, 2018.
- [185] L. Sortino, P. G. Zotev, S. Mignuzzi, J. Cambiasso, D. Schmidt, A. Genco, M. Aßmann, M. Bayer, S. A. Maier, R. Sapienza, and A. I. Tartakovskii, “Enhanced light-matter interaction in an atomically thin semiconductor coupled with dielectric nano-antennas,” *Nature communications*, vol. 10, no. 1, p. 5119, 2019.
- [186] L. Sortino, *Enhanced light-matter interaction in atomically thin semiconductors coupled with dielectric nano-antennas*. PhD thesis, The University of Sheffield, Sheffield, UK, 2021.

- [187] J. Cambiasso, G. Grinblat, Y. Li, A. Rakovich, E. Cortés, and S. A. Maier, “Bridging the gap between dielectric nanophotonics and the visible regime with effectively lossless gallium phosphide antennas,” *Nano letters*, vol. 17, no. 2, pp. 1219–1225, 2017.
- [188] K. S. Novoselov, A. K. Geim, S. V. Morozov, D. Jiang, Y. Zhang, S. V. Dubonos, I. V. Grigorieva, and A. A. Firsov, “Electric field effect in atomically thin carbon films,” *Science (New York, N.Y.)*, vol. 306, no. 5696, pp. 666–669, 2004.
- [189] A. Castellanos-Gomez, M. Buscema, R. Molenaar, V. Singh, L. Janssen, H. S. J. van der Zant, and G. A. Steele, “Deterministic transfer of two-dimensional materials by all-dry viscoelastic stamping,” *2D Materials*, vol. 1, no. 1, p. 011002, 2014.
- [190] M. A. Meitl, Z.-T. Zhu, V. Kumar, K. J. Lee, X. Feng, Y. Y. Huang, I. Adesida, R. G. Nuzzo, and J. A. Rogers, “Transfer printing by kinetic control of adhesion to an elastomeric stamp,” *Nature Materials*, vol. 5, no. 1, pp. 33–38, 2006.
- [191] A. J. Brash, J. Iles-Smith, C. L. Phillips, D. P. S. McCutcheon, J. O’Hara, E. Clarke, B. Royall, L. R. Wilson, J. Mørk, M. S. Skolnick, A. M. Fox, and A. Nazir, “Light scattering from solid-state quantum emitters: Beyond the atomic picture,” *Physical Review Letters*, vol. 123, no. 16, p. 167403, 2019.
- [192] L. Sortino, “Bright single photon emitters with enhanced quantum efficiency in a two-dimensional semiconductor coupled with dielectric nano-antennas,” *Nature communications*, vol. 12, no. 6063, 2021.
- [193] P. Tonndorf, R. Schmidt, R. Schneider, J. Kern, M. Buscema, G. A. Steele, A. Castellanos-Gomez, H. S. J. van der Zant, S. Michaelis de Vasconcellos, and R. Bratschitsch, “Single-photon emission from localized excitons in an atomically thin semiconductor,” *Optica*, vol. 2, no. 4, p. 347, 2015.

- [194] B. Li, Z. Ren, N. Zhong, and W. Xie, “Highly linear polarized photoluminescence from a rippled WSe<sub>2</sub> monolayer,” *Optics express*, vol. 27, no. 9, pp. 12436–12442, 2019.
- [195] S. Kumar, M. Brotóns-Gisbert, R. Al-Khuzheyri, A. Branny, G. Ballesteros-Garcia, J. F. Sánchez-Royo, and B. D. Gerardot, “Resonant laser spectroscopy of localized excitons in monolayer WSe<sub>2</sub>,” *Optica*, vol. 3, no. 8, p. 882, 2016.
- [196] J.-P. So, K.-Y. Jeong, J. M. Lee, K.-H. Kim, S.-J. Lee, W. Huh, H.-R. Kim, J.-H. Choi, J. M. Kim, Y. S. Kim, C.-H. Lee, S. Nam, and H.-G. Park, “Polarization control of deterministic single-photon emitters in monolayer WSe<sub>2</sub>,” *Nano letters*, vol. 21, no. 3, pp. 1546–1554, 2021.
- [197] C. Chakraborty, N. Vamivakas, and D. Englund, “Advances in quantum light emission from 2D materials,” *Nanophotonics*, vol. 8, no. 11, pp. 2017–2032, 2019.
- [198] S. Mouri, Y. Miyauchi, M. Toh, W. Zhao, G. Eda, and K. Matsuda, “Nonlinear photoluminescence in atomically thin layered WSe<sub>2</sub> arising from diffusion-assisted exciton-exciton annihilation,” *Physical Review B*, vol. 90, no. 15, 2014.
- [199] P. Dey, J. Paul, Z. Wang, C. E. Stevens, C. Liu, A. H. Romero, J. Shan, D. J. Hilton, and D. Karauskaj, “Optical coherence in atomic-monolayer transition-metal dichalcogenides limited by electron-phonon interactions,” *Physical Review Letters*, vol. 116, no. 12, p. 127402, 2016.